MASTER THESIS

Dark Stars: Review and Open Questions

Author:
Chirag MEHROTRA(Matrikelnr: 5340174)

Supervisor:
Prof. Dott. Andrea SANTANGELO,
Dr. Denys MALYSHEV,
Dr. Lorenzo DUCCI

A thesis submitted in fulfillment of the requirements for the degree of Master Astro and Particle Physics

in the

High Energy Astrophysics
Institut für Astronomie und Astrophysik Tübingen (IAAT)

Declaration of Authorship

I, Chirag MEHROTRA(Matrikelnr: 5340174), declare that this thesis titled, "Dark Stars: Review and Open Questions" and the work presented in it are my own. I confirm that:

- This work was done wholly or mainly while in candidature for a research degree at this University.
- Where any part of this thesis has previously been submitted for a degree or any other qualification at this University or any other institution, this has been clearly stated.
- Where I have consulted the published work of others, this is always clearly attributed.
- Where I have quoted from the work of others, the source is always given. With the exception of such quotations, this thesis is entirely my own work.
- I have acknowledged all main sources of help.
- Where the thesis is based on work done by myself jointly with others, I have made clear exactly what was done by others and what I have contributed myself.

Signed: Chirag

Date: 28/08/2022 Tübingen

"Dark Matter Dark matter is an idea. The Universe behaves in a way that cannot be explained by the amount of material we can see. A galaxy would have to be about ten times bigger than the galaxy we can see to explain its behaviour. Scientists don't know what else might be present – they can't see anything – so they call the missing part dark matter. It could be particles, or very small dim stars, or black holes – some scientists think dark matter could be hot, and some think it could be cold. Discussions – and research – continue. "

Stephen Hawking, Unlocking the Universe

EBERHARD KARLS UNIVERSITÄT TÜBINGEN

Abstract

Institut für Astronomie und Astrophysik Tübingen (IAAT)

Master Astro and Particle Physics

Dark Stars: Review and Open Questions

by Chirag MEHROTRA(Matrikelnr: 5340174)

The first objects are theorised to be formed at the center of high density dark matter halos. These objects are POPIII stars which are massive and heavy. Spolyar, Freeze and Paolo in their work titled "Dark matter and the first stars: a new phase of stellar evolution"[1] proposed that very first stars use energy released by dark matter dark matter annihilation instead of thermonuclear fusion to keep the star in equilibrium against its own gravitational contraction. These stars, called "Dark Stars", even though use dark matter-dark matter annihilation as their main energy source, are made up of almost entirely of hydrogen and helium. We sought to look into and examine the theoretical work on dark stars in this study. We will study on the ways a dark star can be born. The three criteria i.e. high dark matter density, dark matter annihilation products gets trapped at the stellar surface and dark matter-dark matter annihilation is the major heating/cooling mechanism in the star, should be fulfilled in order to be a star called a dark star. We have discussed in detail how dark matter can be collected via adiabatic contraction and scattering capture and how a dark star evolves.Here we follow different works on the evolution of dark stars.

These stars can be giant, puffy ($\sim 10AU$) and cool surface temperature objects ($\sim 10,000K$)[2]. They can be detected using the, now launched, James Webb Space Telescope. Two works on the detectability of dark stars by the JWST are discussed, one for the supermassive dark stars with masses $> 10^5 M_\odot$ and other for dark stars with masses $10^3 M_\odot$ which can be detected by JWST by phenomenon of gravitational microlensing. The signatures of dark stars in Cosmic Microwave Background and its effects on reionization can also be good indication for their presence. Open questions like ,we have discussed, how dark stars can be a possible solution to "*Paradox of Youth problem*" and if galactic center can be a suitable location for survival of dark stars. We have also discussed if the stellar clusters can show some signatures of effects of dark matter annihilation which can be also a good place for hunting of dark stars. When dark stars use up all their dark matter, they can collapse directly to black holes which can act as seeds for supermassive black holes. The dark stars can also form the missing black holes masses which are observed via LIGO and Virgo but are not predicted theoretically. Lastly, we have also run three exemplar simulation codes on "DarkStars" developed by P. Scott, J. Edjsö and M. Fairbairn [3], which is a simulation code studying the evolution of dark stellar properties, on our system to virtually see the capture of dark matter and evolution of dark star's properties in three different dark matter density profiles. These codes are very basic and were run for a $1M_\odot$ star.

Acknowledgements

I would like to express my sincere gratitude to my supervisors, Prof. Dott.Andrea Santangelo, Dr. Denys Malyshev and Dr. Lorenzo Ducci for their expert supervision, guidance and their help in solving the problems I faced while working on this thesis. I am thankful to my supervisors for motivating and encouraging me to find new ways to find solutions to the problems. Without their insights, this work would have not been possible.

I am really thankful to my family for their moral and emotional support in such difficult times when the world is going through a pandemic. Without you, none of this would be possible.

Contents

Chapter 1

Introduction

The current theory for the birth of the Universe is that of Universe being born from an infinitely dense space-time singularity which exploded around 13.7 billion years ago, known as the Big Bang. The Big Bang theory is a remarkably simple theory built on two pillars: the Einstein's theory of general relativity and the assumption that the universe is isotropic and homogeneous on large scales[4].This theory has had a number of important successes: it can explain the observed expansion of the universe; the thermal microwave background radiation; the observed abundances of deuterium, helium, and lithium; and the rapid evolution seen in distant galaxies[4] [5] [6]. After the Big Bang, the Universe underwent different epochs[7]:

- The first epoch in the history of the Universe was known as the *Planck epoch*, which lasted until $t \sim 10^{-43}$ s ($kT \sim 10^{19}$ GeV) after the Big Bang. It is thought that quantum adjustments to our current theory of gravity are important to define this epoch when all of the fundamental forces may have been united.(Refer to [8] for evolution of the Universe through this era.)

- Gravity dissociated from the other fundamental forces defined by the grand unified theory during the *GUT epoch*, which lasted approximately $t \sim 10^{-43}s - 10^{-35}s$. There were all known particles as well as particles from additional theories such as super-symmetry (SUSY). The end of this period was caused by the breaking of symmetry between the strong and electroweak forces.

- The *Quark era* happened at $t \sim 10^{-11}$s. The symmetry between the electromagnetic and weak forces was broken. It is also hypothesized that the Higgs mechanism occurred at this time.

- During the *Hadron epoch*, which started $t \sim 10^{-6}$s after the big bang, quarks and gluons no longer survive as independent particles, but instead formed quark bound states and condensed to hadrons and mesons. With a further fall in temperature, the hadrons annihilate, resulting in a minor asymmetry. A tiny percentage of hadrons survived as a result of this asymmetry (stable neutrons and protons).

- As the Universe continued to expand, the temperature of the Universe dropped further, causing the charged tauons and muons to vanish within the first microseconds. However, the pair production process was still ongoing, resulting in an excess of electrons, kicking off the *lepton epoch* since there were 10^9 times more electrons than protons or neutrons.

- The different kinds of fermions and bosons would have been in *thermal equilibrium* if $kT \gg mc^2$. As the Universe expands and temperature falls, the collision probability becomes too tiny, and particles *freeze out*.

- The neutrino separated from the rest of the particles at $kT \sim 2MeV$, or $t \sim 1s$, since the reaction $\nu + \bar{\nu} \longrightarrow e^+ + e^-$ could no longer take place. They had a temperature of $T_\nu \propto 1/R$ [1], generating a cosmic neutrino background similar to the Cosmic Microwave Background.

- After 2 seconds of the Big Bang, the neutron-to-proton ratio decreases because the temperature drops less than the rest mass energy. When the temperature fell below the rest mass energy of electrons and positrons, they began to decay via the reaction $e^+ + e^- \longrightarrow \gamma + \gamma$, creating more photons and initiating the *photon epoch*. After 2 minutes, the first elements are formed. Because deuterium could no longer decay, *nucleosynthesis* occurrs.

- The shift from a radiation-dominated to a matter-dominated epoch occurred around 10000 years after the big bang. The decoupling of photons from the matter that produces the *CMB* began roughly 350000 years. Large structure formation became feasible after this epoch.

The energy-matter content of Universe comprises of dark energy, dark matter and baryonic matter. According to recent Planck mission results[9], the inferred (model-based) late-Universe parameters parameters, assuming the base-Λ CDM model are: Hubble Constant $H_0 = 67.4 \pm 0.5 kms^{-1}Mpc^{-1}$; matter density parameter $\Omega_m = 0.315 \pm 0.007$. The dark matter and baryonic density is $\Omega_c h^2 = 0.120 \pm 0.001$ and $\Omega_b h^2 = 0.0224 \pm 0.0001$ respectively.

The standard cosmological structure formation model covers the shape and material composition of the universe (galaxies of different kinds and sizes, groups and clusters of galaxies, complete space networks of filaments and cavities that are virtually uniform at high temperatures). These patterns appear to be the result of quantum zero point fluctuations created during the early inflationary phase of the universe. Over the next few years, these small-density perturbations were reinforced primarily by the relentless action of gravity by dark matter, but illuminated by complex astrophysical phenomena involving ordinary matter[10].

In this work we will look into the effects of dark matter on stellar formation and evolution. First proposed by [1], these stars use dark matter-dark matter annihilation as their primary energy source, instead of nuclear fusion, to keep themselves in hydrostatic and thermal equilibrium even though these stars are made (almost entirely) of hydrogen and helium. They called these stars **Dark Stars**.The WIMP or Weakly Interacting Massive Particle is the preferred model of dark matter. These are the stars that were born when Universe was roughly 200 million years old at redshift $z = 10 - 15$ ending the dark ages of the Universe and can grow as long as there is dark matter to power it, therefore it can reach the mass of $10^7 M_\odot$ with luminosity $10^{11} L_\odot$[2].

In subsequent sections we will look into evidences and role of dark matter in structure formation; search strategies for dark matter and their properties; and why WIMPs are popular model of dark matter. In chapter 2 we will briefly look into the physics of Dark Matter-Dark Matter annihilation, in chapter 3 we will discuss Dark Stars in detail i.e. the 3 criteria to form dark stars, if other models of dark matter can form dark stars and their main energy sources are discussed. In chapter 4 we will look into scattering capture of dark matter by the stars; in chapter 5 we will look into the simulations and evolution of dark stars. Chapter 6 will be dedicated towards the observation of dark stars directly (using James Webb Space Telescope and Hubble

[1] where R is the scale factor

Space Telescope) or indirectly (signatures in Cosmic Microwave Background and reionization, Extragalactic Background Light). In chapter 7, we have discussed open questions like Paradox of Youth, effects of dark matter on different stages of stellar evolution, if dark stars can be found in stellar clusters and if Dark Stars can be the solution to black holes masses found by LIGO and Virgo collaborations, which were not predicted by current stellar evolution theorem and if the Dark Stars can be seeds to Supermassive black holes. We will also see the capabilities and how code "DarkStars" work, developed by [3], and run very simple codes for dark star evolution in three different dark matter density profiles. The $1M_{\odot}$ star in these codes collect dark matter via capture scattering. Finally, in chapter 8 we will summarize the thesis.

1.1 Evidences and role of Dark Matter in Structure Formation

In 1933, Zwicky published unambiguous evidence for Dark Matter in the Coma galaxy cluster[11]; in 1939, Babcock's rotation curve for the Andromeda Nebula [12] indicated that much of its mass is at large radius. In 1959, Kahn and Woltjer argued that the total mass of the Milky Way and Andromeda galaxies must be much larger than their stellar mass in order to explain why they are currently approaching each other[13].The hypothesis that galaxies and galaxy clusters are surrounded by huge dark matter halos is getting a good test since 1970's. The influential, based on observations, papers of Ostriker, Peebles and Yahil[14] and Einasto,Kaasik,Saar, and Chernin[15] and with Ostriker and Peebles' theoretical argument that massive halos are required to stabilize spiral galaxy disks[16]. Within four years, a hierarchically merging population of dark matter halos formed the basis for the galaxy formation scenario proposed by White and Reese[17], providing the gravitational potential well within which gas cools and condenses to form galaxies[10].

1.2 Search for Dark Matter

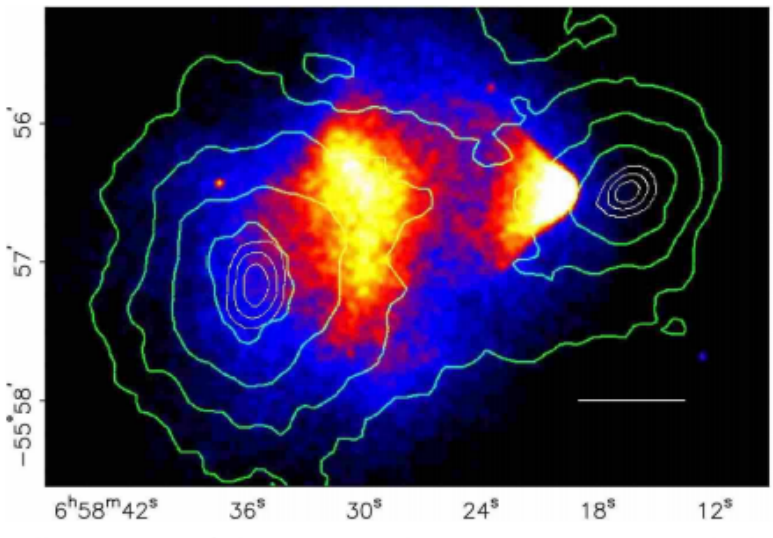

FIGURE 1.1: Bullet Cluster mass density contours (green) and the distribution of baryonic matter. Credit: [18]

Dark matter have the following properties[19]:

- Dark Matter cannot be baryons because if baryons make up dark matter then the CMB and cosmic web of structures would look radically different and the abundance of light elements created during big bang nucleosynthesis depends strongly on the baryonic density(refer[20] and references therein). Also from the recent Planck observations[9], the baryonic matter density is around $\Omega_b h^2 = 0.02237 \pm 0.00015$.
- Dark Matter cannot be light sub-keV-mass particles unless they were created via a phase transition in the early universe like QCD axions[21], this is because light particles are relativistic in earlier times and thus fly out of small scale density perturbations.
- Dark matter is electromagnetically neutral. There are strong constraints on the electromagnetic of dark matter[22].
- From the observations of the Bullet cluster, we see that the dark matter clouds pass without any or some interaction which means that they interact with baryonic matter weakly. Self-interaction of dark matter is important to be considered as they will have effects on structure formation. In our case the dark matter self annihilation being the energy source for the dark stars.

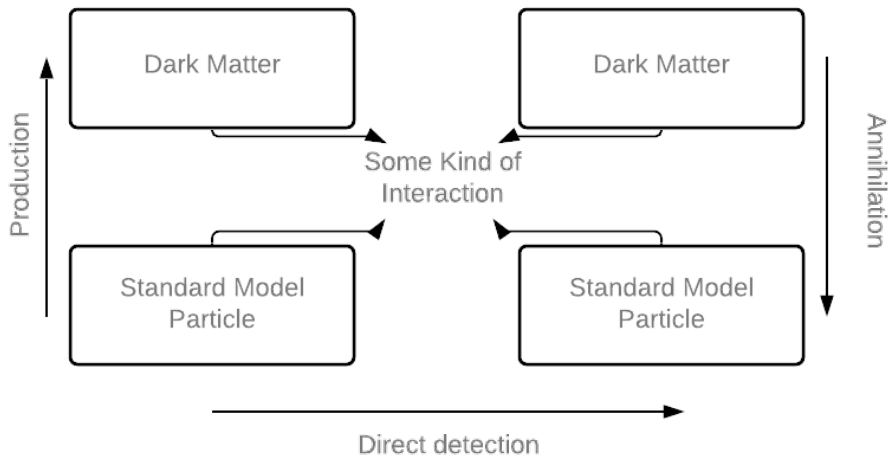

FIGURE 1.2: A toy Feynman Diagram for the search strategies which depends on the direction in which one looks at the diagram

The detection of dark matter depends on the type and strength of interactions with baryonic matter. As seen in figure 1.2, there are three main strategies for detection of dark matter. Going through diagram from bottom-to-top, we produce dark matter particles using Standard-Model particles. This technique is used in colliders like the Large Hadron Collider. Reading the diagram sideways(left-to-right), we are looking for the effects on Standard-model particles induced by their interactions with dark matter. When we look at the diagram from top-to-bottom, we are looking for Standard-model particles produced by annihilation of the dark matter or decays(refer [19] and references therein, for details in observations of dark matter.)

1.3 Weakly Interacting Massive Particles or WIMPs

WIMPs are considered to be among the best motivated dark matter candidates. This candidate was first introduced by Steigman & Turner[23]. The key features of this candidate are: interactions around or near typical weak-force interaction, particle masses near the weak scale ($m \sim 100GeV$). This candidate class has the additional features that it may naturally make up all the dark matter in the Universe.Many WIMP candidates are antiparticles of their own and when they first come into thermal equilibrium in the early universe, they annihilate each other, leaving a predictable amount of them today. A huge percentage of WIMPs freeze out when the annihilation rate falls below the Hubble expansion rate.The relic density of these particles is approximately [2][24][25]

$$\Omega_\chi h^2 \simeq \frac{3 \times 10^{-27} \frac{cm^3}{sec}}{< \sigma v >}, \tag{1.1}$$

where Ω_χ is the fraction of the energy density in the Universe today in the form of WIMPs; h is the Hubble constant in the units of 100km/s/Mpc.WIMPs naturally make up about the proper dark matter density today on the assumption that the annihilation cross section $\langle \sigma v \rangle$ is governed by the weak interaction strength. This occurrence is referred to as "the WIMP miracle." This is why WIMPs are seen as a viable Dark Matter contender[2].

Not only do WIMPs exist naturally in particle theories described to solve problems unrelated to Dark Matter, but Super-symmetric (SUSY) Extension of the standard model of particle physics predicts the presence of additional companions for each particle in the standard model, with the lightest of these being dark matter candidates given R-parity. The lightest neutralino in the Minimal Super-symmetric Standard Model, in particular, is a promising WIMP candidate. WIMP dark matter candidates may be present in models with universal extra dimensions, for example Kaluza-Klein particles[2].

Chapter 2

Dark Matter Annihilation

In this chapter, we will look into the annihilation of WIMPs into Fermions, Gauge Bosons, Higgs Bosons and photons briefly.

2.1 Annihilation Into Fermions

Neutralinos can annihilate to fermion pairs by the tree level diagrams. These processes consist of s-channel exchange of pseudoscalar Higgs and Z^0-bosons and t-channel exchange of s-fermions [24][25]. Calculations shown here are taken from [24] and [25] and credit is given to the authors of them.

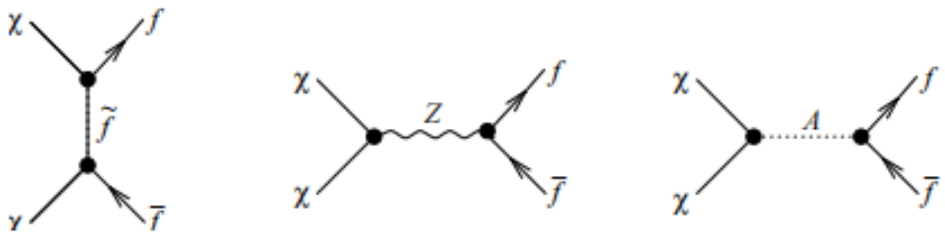

FIGURE 2.1: Tree level diagrams for neutralino annihilation into fermion pairs.Credit:[24][25]

The amplitude for pseudoscalar Higgs exchange is given by

$$A_A = 4\sqrt{2}gT_{A11}h_{Aff}\frac{1}{4-(\frac{m_A}{m_\chi})^2+i\Gamma_A\frac{m_A}{(m_\chi)^2}} \tag{2.1}$$

Here, m_A is the pseudoscalar Higgs mass and Γ_A is the pseudoscalar Higgs width. T_{A11} is the A^0-neutralino-neutralino coupling and is given by

$$T_{A11} = -\sin(\beta Q''_{1,1}) + \cos(\beta S''_{1,1}) \tag{2.2}$$

where,

$$Q''_{1,1} = N_{3,1}(N_{2,1} - \tan(\Theta_W N_{1,1}) \tag{2.3}$$

and

$$S''_{1,1} = N_{4,1}(N_{2,1} - \tan(\Theta_W N_{1,1}) \tag{2.4}$$

N is the matrix which diagonalizes the neutralino mass matrix (for neutralino mass eigenstates, refer to appendix A of [24]). Θ_W is the Weinberg angel and $\tan(\beta)$ is the ratio of the Higgs vacuum expectation value. h_{Aff} is the A^0-fermion-fermion

Yukawa coupling. For up-type fermions, this is given by

$$h_{Aff} = -\frac{g m_f \cot\beta}{2m_W^{\pm}} \tag{2.5}$$

For down-type fermions, it is given as

$$h_{Aff} = -\frac{g m_f \tan\beta}{2m_W^{\pm}} \tag{2.6}$$

The amplitude for the neutralino annihilation via sfermion exchange to a pair of fermions, fi, $\bar{f}_i$ is given as

$$A_{\bar{f}} = \sqrt{2}\sum_{j=1}^{6}\frac{1}{P_j}([(X'_{ij1})^2 + (W'_{ij1})^2]\frac{m_{f_i}}{m_\chi} + 2X'_{ij1}W'_{ij1} \tag{2.7}$$

where

$$P_j = 1 + (\frac{m_{\bar{f}_j}}{m_\chi})^2 - (\frac{m_{f_i}}{m_\chi}) \tag{2.8}$$

and the sum is over the six sfermion states which couple to the final state fermion. The fermion-sfermion-neutralino couplings,

$$X'_{ij1} = X_1(\Pi_L\Theta_f)_{i,j} + Z_{i,k,1}(\Pi_R\Theta_f)_{k,j} \tag{2.9}$$

and

$$W'_{ij1} = Y_1(\Pi_R\Theta_f)_{i,j} + Z_{i,k,1}(\Pi_L\Theta_f)_{k,j} \tag{2.10}$$

where

$$X_1 = -g\sqrt{2}[T_3(f_i)N^*_{2,1} - \tan\theta_W(T_3(f_i) - e(f_i))N^*_{1,1}] \tag{2.11}$$

and

$$Y_1 = g\sqrt{2}\tan\theta_W e(f_i)N^*_{1,1} \tag{2.12}$$

For final state up-type quark,

$$Z_{i,j,1} = -\frac{g}{\sqrt{2}m_{W^\pm}\sin\beta}\Theta_{i,j}N^*_{4,1} \tag{2.13}$$

For final state down-type quark,

$$Z_{i,j,1} = -\frac{g}{\sqrt{2}m_{W^\pm}\cos\beta}\Theta_{i,j}N^*_{3,1} \tag{2.14}$$

And for final state leptons,

$$Z_{i,j,1} = -\frac{g}{\sqrt{2}m_{W^\pm}\cos\beta}\Theta_{i,j}N^*_{3,1} \tag{2.15}$$

Here, T3(fi) and e(fi) are the weak hypercharge and electric charge of the final state fermion. N, again is the matrix which diagonalizes the neutrino mass matrix. Θ_f's are the appropriate 6×6 sfermion mass matrices and $\Pi_{L,R}$ are left and right projection operators:

$$\Pi_L = \begin{pmatrix} 1 & 0 & 0 & 0 & 0 & 0 \\ 0 & 1 & 0 & 0 & 0 & 0 \\ 0 & 0 & 1 & 0 & 0 & 0 \end{pmatrix} \tag{2.16}$$

$$\Pi_R = \begin{pmatrix} 0 & 0 & 0 & 1 & 0 & 0 \\ 0 & 1 & 0 & 0 & 1 & 0 \\ 0 & 0 & 1 & 0 & 0 & 1 \end{pmatrix} \tag{2.17}$$

Lastly, the amplitude for neutralino annihilation to fermions via Z exchange is given by

$$A_Z = 2\sqrt{2}\frac{g^2}{\cos^2\theta_W} O''^L_{1,1} T_3(f_i) \frac{m_{f_i} m_\chi}{m_Z^2} \tag{2.18}$$

where $T_3(f_i)$ is the weak hypercharge of the fermion. The coupling $O''^L_{1,1}$ is given by $\frac{1}{2}(-N_{3,1}N^*_{3,1} + N_{4,1}N^*_{4,1})$.

Summing these all contributions to the amplitude, we can calculate the cross section for this process as

$$\sigma v(\chi\chi \longrightarrow \bar{f}_i f_i)_{v\longrightarrow 0} = \frac{c_f \beta_f}{128\pi m_\chi^2} |A_A(\chi\chi \longrightarrow \bar{f}_i f_i) + A_{\tilde{f}}(\chi\chi \longrightarrow \bar{f}_i f_i) + A_Z(\chi\chi \longrightarrow \bar{f}_i f_i)|^2 \tag{2.19}$$

where $\beta_f = \sqrt{1 - \frac{m_f^2}{m_\chi^2}}$. c_f is a colour factor which is equal to three for quark final states and one otherwise.

All tree level low velocity neutralino annihilation diagrams to fermion pairs have amplitudes proportional to the final fermion mass. This is due to the fact that for sfermion and Z^0 exchange, the Z^0-fermion-fermion and neutralino-fermion-fermion connections maintain chirality.

The amplitude introduces an explicit factor of the fermion mass in the Yukawa coupling for pseudoscalar Higgs exchange. It's also worth mentioning that the Yukawa coupling is proportional to $\tan\beta$ for down-type quarks and $\cot\beta$ for up-type quarks in the pseudoscalar Higgs exchange amplitude. As a result of these results, heavy final states ($b\bar{b}$, $tau^- tau^+$, and, if kinematics permitted, $t\bar{t}$) will dominate neutralino annihilation into fermions. Furthermore, if $\tan\beta$ is big, bottom-type fermions, even if less heavy, may prevail over up-type fermions. Even for neutralinos, annihilation to $b\bar{b}$ may dominate over $t\bar{t}$.

2.2 Annihilation into Gauge Bosons

Neutralinos can annihilate into gauge bosons via several processes[24]. Calculations shown here are taken from [24] and [25] and credit is given to the authors of them.

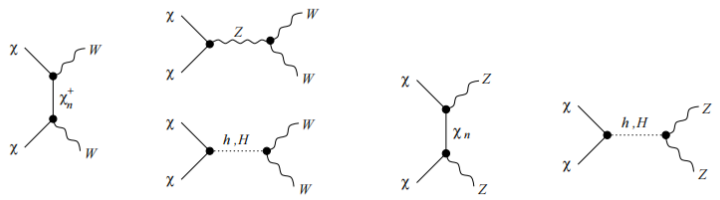

FIGURE 2.2: Tree level diagrams for neutralino annihilation into gauge bosons pairs.Credit: [24][25]

In the low velocity limit, the amplitude for neutrino annihilation to $W^{\pm}$-pair is given by

$$A(\chi\chi \longrightarrow W^+W^-)_{v\to 0} = 2\sqrt{2}\beta_W g^2 \sum_{n=1}^{2}[(O^L_{1,n})^2 + (O^R_{1,n})^2]\frac{1}{P_n} \tag{2.20}$$

where $\beta_W = \sqrt{1-\frac{m_W^2}{m_\chi^2}}$ and $P_n = 1 + (\frac{m_{\chi_n^\pm}}{m_\chi})^2 - (\frac{m_W}{m_\chi})^2$. The sum is over chargino states. $O^L_{1,n} = \frac{-1}{\sqrt{2}}N_{4,1}V^*_{2,1} + N_{2,1}V^*_{1,n}$ and $O^R_{1,n} = \frac{1}{\sqrt{2}}N^*_{3,1}U_{2,n} + N^*_{2,1}U_{1,n}$ are the neutralino couplings to charginos, where N is the matrix which diagonalizes the neutralino mass matrix. The V's and U's are components of the chargino mass matrix, in the basis.

$$U = \begin{pmatrix} \cos\phi_- & -\sin\phi_- \\ \sin\phi_- & \cos\phi_+ \end{pmatrix} \tag{2.21}$$

and

$$V = \begin{pmatrix} \cos\phi_+ & -\sin\phi_+ \\ \sin\phi_+ & \cos\phi_- \end{pmatrix} \tag{2.22}$$

where

$$\tan 2\phi_- = 2\sqrt{2}m_W\frac{(\mu\sin\beta + M_2\cos\beta)}{(M_2^2 - \mu^2 + 2m_W^2\cos\beta)} \tag{2.23}$$

and

$$\tan 2\phi_+ = 2\sqrt{2}m_W\frac{(\mu\cos\beta + M_2\sin\beta)}{(M_2^2 - \mu^2 - 2m_W^2\cos\beta)} \tag{2.24}$$

The amplitude for the annihilation to Z^0-pairs is similar:

$$A(\chi\chi \longrightarrow Z^0Z^0)_{v\to 0} = 4\sqrt{2}\beta_Z\frac{g^2}{\cos^2\theta_W}\sum_{n=1}^{4}(O''^L_{1,n})^2\frac{1}{P_n} \tag{2.25}$$

Here, $\beta_Z = \sqrt{1-\frac{m_Z^2}{m_{\chi 2}}}$ and $P_n = 1 + (\frac{m_{\chi n}}{m_\chi})^2 - (\frac{m_z}{m_\chi})^2$. The sum is over neutralino states. Also, $O''^L_{1,n} = \frac{1}{2}(-N_{3,1}N^*_{3,n} + N_{4,1}N^*_{4,n})$

The low velocity annihilation cross section for this mode is given by

$$\sigma v(\chi\chi \longrightarrow GG)_{v\to 0} = \frac{1}{S_G}\frac{\beta_G}{128\pi m_\chi^2}|A(\chi\chi \longrightarrow GG)|^2 \tag{2.26}$$

where G indicates which gauge boson is being considered. S_G is a statistical factor equal to one for W^+W^- and two for Z^0Z^0. It should be noted that pure-gaugino neutralinos have no S-wave annihilation amplitude to gauge bosons. Pure-higgsinos or mixed higgsino-gauginos, however, can annihilate efficiently via these channels, even at low velocities.

2.3 Annihilation Into Higgs Bosons

There are many tree level diagrams which contribute to neutralino annihilation into Higgs boson pairs or a Higgs boson and a gauge boson. In the low velocity limit, the amplitude for neutralino annihilation to a Z^0 and a light neutral Higgs h^0, is given by[24]

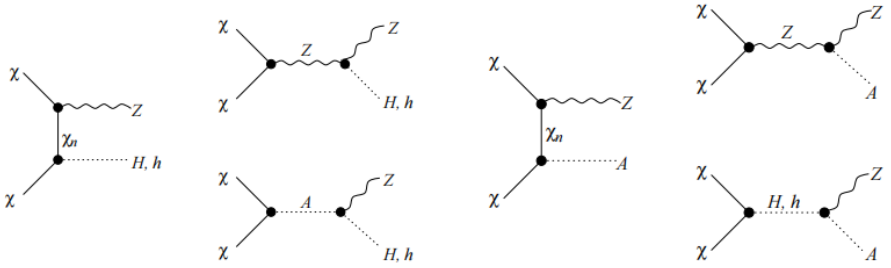

FIGURE 2.3: Tree level diagrams for neutralino annihilation into Z and Higgs boson. Credit:[24] [25]

$$A(\chi\chi \to Z^0 h^0)_{v\to 0} = -2\sqrt{2}\beta_{Zh}\frac{m_\chi}{m_Z}\frac{g^2}{\cos\theta_W}\left[-2\sum_{n=1}^{4} O''^{L}_{1,n} T_{h1,n}\frac{m_{\chi n}-m_\chi}{m_\chi P_n} + O''^{L}_{1,1}\frac{m_\chi \sin(\beta-\alpha)}{m_Z\cos\theta_W}\right] \times -2\sqrt{2}\beta_{Zh}\frac{g^2}{\cos\theta_W}\left[-\frac{2\cos(\alpha-\beta)T_{A1,1}}{4-\frac{m_A^2}{m_\chi^2}+i\Gamma_A\frac{m_A}{m_\chi^2}}\right] \tag{2.27}$$

where Γ_A is the pseudoscalar Higgs width and $T_{h1,n}$ is the $h^0-\chi_0-\chi_n$ Yukawa coupling. Also, $O''^{L}_{1,n} = N_{3,1}(N_{2,n}-\tan\theta_W N_{1,n})/2 + N_{3,n}(N_{2,1}-\tan\theta_W N_{1,1})/2$ and $P_n = 1+(m_{\chi n}/m_\chi)^2 - 1/2(m_Z/m_\chi)^2 - 1/2(m_h/m_\chi)^2$. $\tan\beta$ is the ratio of the Higgs vacuum expectation values and the mixing angle, α, is related to β by

$$\sin 2\alpha = -\sin 2\beta\left(\frac{m_H^2+m_h^2}{m_H^2-m_h^2}\right) \tag{2.28}$$

and

$$\cos 2 = -\cos 2\beta\left(\frac{m_A^2-m_Z^2}{m_H^2-m_h^2}\right) \tag{2.29}$$

The terms of Eq.2.27 correspond to neutralino, Z^0 and A^0 exchange, from first to last.

The expression for neutralino annihilations to a Z^0 and a heavy Higgs boson,H^0, is the same, but with $\sin(\beta\alpha)$ and $\cos(\alpha\beta)$ exchanged, and the couplings and masses of h^0 replaced by the couplings and masses of H^0. These Yukawa couplings are given by

$$T_{h1,n} = \sin\alpha Q''_{1,n} + \cos\alpha S''_{1,n} \tag{2.30}$$

and

$$T_{H1,n} = -\cos\alpha Q''_{1,n} + \sin\alpha S''_{1,n} \tag{2.31}$$

Here, $S''_{1,n} = N_{4,1}(N_{2,n}-\tan\theta_W)/2 + N_{4,n}(N_{2,1}-\tan\theta_W N_{1,1})/2$. $Q''_{1,n}$ is defined above.

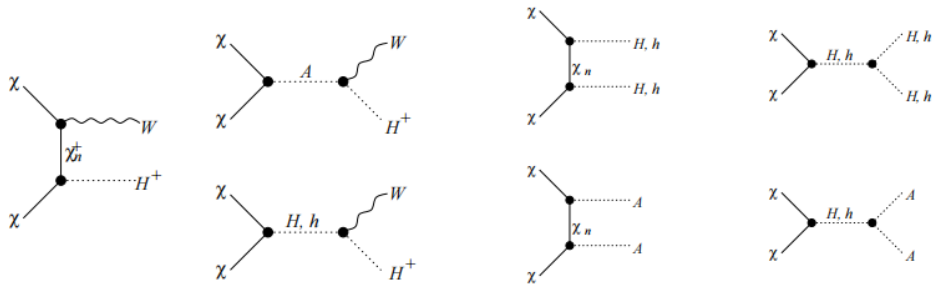

FIGURE 2.4: Tree level diagrams for neutralino annihilation into a $W^{\pm}$ and Higgs boson or a pair of Higgs bosons. Credit:[24] [25]

The amplitude for annihilation to a $W^{\pm}$ and a charged Higgs boson is given by

$$A(\chi\chi \to W^{\pm}H^{\mp})_{v\to 0} = 4\sqrt{2}\beta_{WH}g^2\left[\frac{1}{2}\sum_{n=1}^{2}\frac{m_\chi}{m_W}\frac{O^R_{1,n}Q'^R_{1,n} - O^L_{1,n}Q'^L_{1,n}}{P_n} + \frac{1}{2}\sum_{n=1}^{2}\frac{m_{\chi_n^+}}{m_W}\frac{O^R_{1,n}Q'^L_{1,n} - O^L_{1,n}Q'^R_{1,n}}{P_n}\right] \times 4\sqrt{2}\beta_{WH}g^2\left[-\frac{m_\chi T_{A11}}{m_W(4 - m_A^2/m_\chi^2)}\right] \tag{2.32}$$

where $P_n = 1 + (m_{\chi_n^\pm}/m_\chi)^2 - 1/2(m_{H^\pm}/m_\chi)^2 - 1/2(m_W/m_\chi)^2$. $O^R_{1,n}$ and $O^L_{1,n}$ are couplings given earlier.

$$Q'^L_{n,m} = \cos\beta\left[N^*_{4n}V^*_{1m} + \sqrt{\frac{1}{2}}\left(N^*_{2n} + \tan\theta_W N^*_{1n}\right)V^*_{2m}\right] \tag{2.33}$$

and

$$Q'^R_{nm} = \sin\beta\left[N_{3n}U_{1m} - \sqrt{\frac{1}{2}}\left(N_{2n} + \tan\theta_W N_{1n}\right)U_{2m}\right] \tag{2.34}$$

are the chargino-neutralino-charged Higgs couplings where each of the quantities have been defined above.

Chargino exchange is represented by the first and second terms in Eq.(2.32). The pseudoscalar Higgs exchange is the third term. The scalar Higgs exchange has no low velocity contribution.

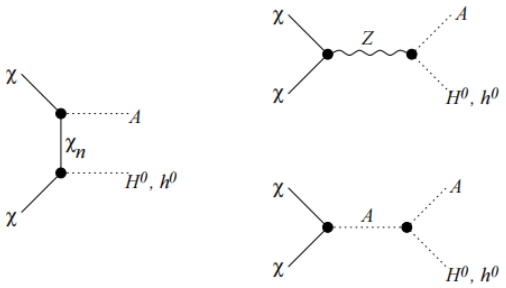

FIGURE 2.5: Tree level diagrams for neutralino annihilation into a neutral Higgs boson and a pseudoscalar Higgs bosons. Credit: [24][25]

The low velocity amplitude for neutralino annihilation into one neutral Higgs boson and one pseudoscalar Higgs boson is given by

$$A\left(\chi\chi \to h^0 A^0\right)_{v\to 0} = \sqrt{2}g^2\left[-4\sum_{n=1}^{4} T_{h0n}T_{a)n}\left(\frac{m_{\chi n}}{m_\chi P_n} - \frac{m_A^2 - m_h^2}{m_\chi^2}\right)\right] \times\sqrt{2}g^2\left[-2\frac{m_Z}{m_\chi}\frac{\sin(\alpha+\beta)\cos 2\beta}{2\cos\theta_W}\frac{T_{A00}}{4 - m_A^2/m_\chi^2}\right] \times\sqrt{2}g^2\left[-\frac{\cos(\alpha-\beta)O_{L00}^{''}}{2\cos^2\theta_W}\frac{m_A^2 - m_h^2}{m_z^2}\right] \tag{2.35}$$

Here, $P_n = 1 + \left(m_{\chi_n}/m_\chi\right)^2 - 1/2\left(m_A/m_\chi\right)^2 - 1/2\left(m_h/m_\chi\right)^2$. The other quantities have been already defined before. The amplitude for a similar process with a heavy Higgs boson rather than a light Higgs boson in the end state is the same, but with $\sin(\alpha+\beta)$ and $\cos(\alpha-\beta)$ swapped out and the light Higgs couplings and masses replaced with those for the heavy Higgs boson. There is no amplitude for neutralino annihilations to H^+H^-, h^0h^0, H^0H^0, A^0A^0 or Z^0A^0 at the low velocity limit. The low velocity cross section for neutralino annihilation via any of these modes is

$$\sigma v\left(\chi\chi \to XY\right)_{v\to 0} = \frac{\beta_{XY}}{128\pi m_\chi^2}\left|A\left(\chi\chi \to XY\right)_{v\to 0}\right|^2, \tag{2.36}$$

where X and Y are labels referring to the final state particles.

2.4 Annihilation into Photons

While no tree level processes exist for neutralino annihilation into photons, loop processes to $\gamma\gamma$ and γZ^0 are extremely intriguing since they may produce a spectral line characteristic detectable in indirect detection techniques. Fig. 2.6 depicts all of the one-loop diagrams for neutralino annihilation to a pair of photons. In Fig 2.7 and 2.8, are Feynman diagrams of annihilation of neutralino to a photon and a Z^0 are shown. Kindly refer to [26] and [27] for $\gamma\gamma$ and γZ^0 final states respectively. Also refer to [28].

The annihilation process' amplitude can be factored in the form

$$A = \frac{e^2}{2\sqrt{2}\pi^2}\epsilon\left(\epsilon_1, \epsilon_2, \kappa_1, \kappa_2\right)\bar{A} \tag{2.37}$$

where ϵ_1,ϵ_2 and κ_1,κ_2 are the polarization tensors and momenta of the two outgoing photons, respectively.

The cross-section is given as

$$\sigma v_{2\gamma} = \frac{\alpha^2 m_\chi^2}{16\pi^3}\left|\bar{A}\right|^2 \tag{2.38}$$

where the total amplitude as the sum of the contributions obtained from the four different classes of diagrams: $\bar{A} = \bar{A}_{f\bar{f}} + \bar{A}_H + \bar{A}_W + \bar{A}_G$ The single contributions are listed in Ref.[26]

The amplitude for the annihilation of neutralino to photon and Z^0 is factorised as

$$A = \frac{e}{2\sqrt{2}\pi^2}\epsilon\left(\epsilon_1, \epsilon_2, \kappa_1, \kappa_2\right)\bar{A} \tag{2.39}$$

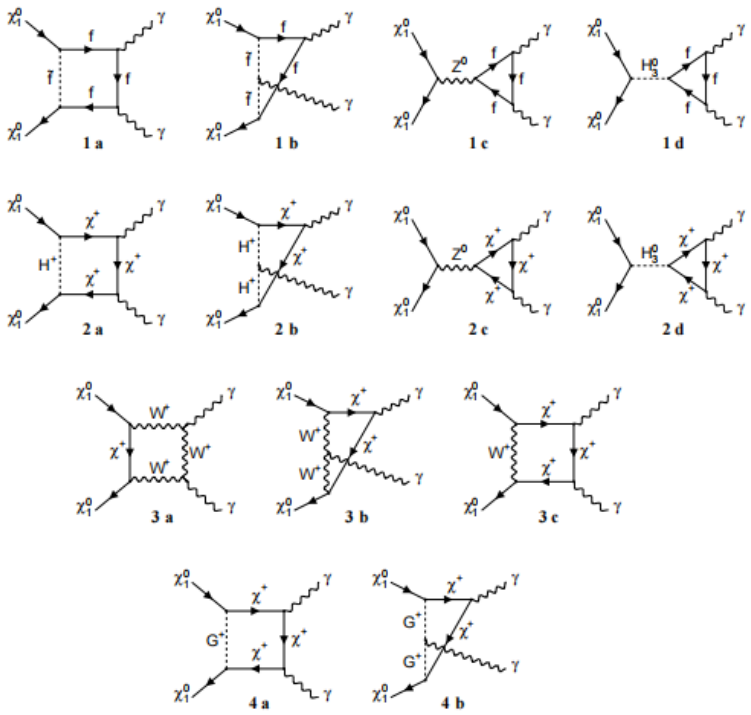

FIGURE 2.6: Diagrams contributing, at one loop level, to neutralino annihilation into two photons. Credit: [24][26]

where ϵ_1, κ_1 are polarisation tensor and momentum of the photon in the final state, and ϵ_2,κ_2 refer to the polarization tensor and the momentum of the Z^0. The cross-section is given as:

$$\sigma v_{Z\gamma} = \frac{\alpha}{32\pi^4} \frac{\left(m_\chi^2 - m_Z^2/4\right)^3}{m_\chi^4} |\bar{A}| \tag{2.40}$$

The total amplitude is given as $\bar{A} = \bar{A}_{f\bar{f}} + \bar{A}_H + \bar{A}_W + \bar{A}_G$ The details of the single contribution are listed in Ref[27]

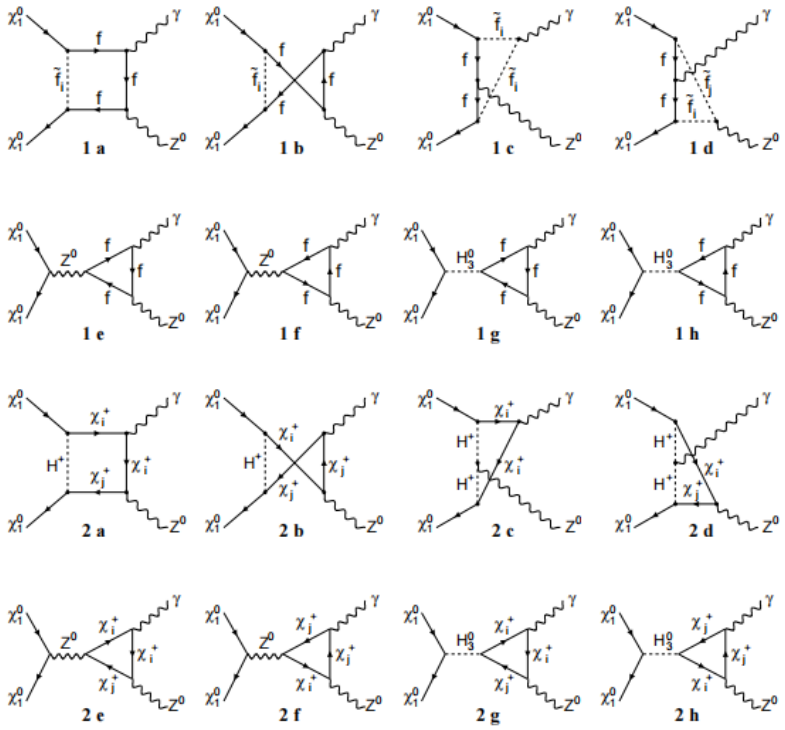

FIGURE 2.7: Diagrams contributing, at one loop level, to neutralino annihilation into a photon and a Z^0. Credit: [24][27]

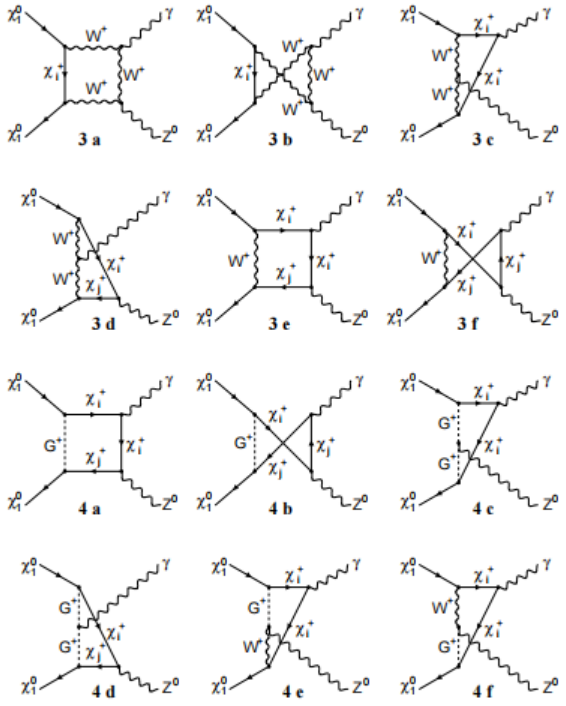

FIGURE 2.8: Diagrams contributing, at one loop level, to neutralino annihilation into a photon and a Z^0. Credit: [24][27]

Chapter 3

Dark Stars: A New Stage in Stellar Evolution

The dark ages came to an end when the first stars were born. These earliest stars are assumed to have been born inside halos of mass $\sim 10^6 M\odot$ which are made up of 85% dark matter and 15% baryons in the form of H and He at redshift $z = 10 - 15$ when the Universe was around 200 million years old. For reviews of standard picture of the formation of the first stars refer [29][30][31][32] to name a few. The baryonic matter cools and collapses via molecular hydrogen cooling [33] into a single small protostar [34] at the center of the halo.

Spolyar, Freese and Gondolo [1] proposed that these very first stars might use the energy released by dark matter-dark matter annihilation rather than fusion as their primary energy source to keep themselves in equilibrium against their own gravitational contraction. They called these stars "**Dark Stars**". As will be shown in Chapter 5 (Evolution of Dark Stars), these stars are much more colder and long lived than the fusion powered stars. For a star to be born as dark star the following three criteria has to be fulfilled[1][2]:

1. High Dark Matter Density inside the star
2. Dark Matter annihilation products become trapped inside the star
3. Dark matter-dark matter annihilation is the major heating/cooling mechanism in the star.

3.1 The Three Criteria

3.1.1 Criteria 1: High Dark Matter density

The energy source for Dark Stars is dark matter annihilation. The annihilation rate is given as [2]

$$n_\chi^2 \langle \sigma v \rangle \tag{3.1}$$

where n_χ is the WIMP number density and $\langle \sigma v \rangle$ is the annihilation cross-section. For various low velocity WIMP annihilation scenarios, the cross-section is given in Chapter 2. But for sake simplicity let us assume the standard annihilation cross-section which is equal to $3 \times 10^{-26} cm^3/s$ [2]. Since the WIMP mass is converted to energy in the annihilation, which produces energy at a rate per unit volume

$$Q_{DM} = n_\chi^2 \langle \sigma v \rangle m_\chi = \langle \sigma v \rangle \frac{\rho_\chi^2}{m_\chi} \tag{3.2}$$

where ρ_χ is the WIMP mass density[2].

Because two WIMP particles must discover each other to annihilate, the DM annihilation rate scales as WIMP density squared, as seen in Eq.(3.2). As a result, whenever the density is high enough, the annihilation is more significant. At redshift z, the density of dark matter increases by $(1+z)^3$ [2]. Since, the first stars are assumed to be born in the dark matter halos' cores, where the density of dark matter is highest, the formation of the protostar in the halo deepens the potential well at the core and draws in additional dark matter. This may be accomplished in two ways: the Blumenthal technique of adiabatic contraction [35] and Young's adiabatic model [36].

Blumenthal vs. Young

Blumenthal method [35] describes the response of a dissipationless halo to the infall of a small dissipational fraction of its mass. This model uses that for periodic orbits, $\oint pdq$ is an adiabatic invariant, where p is the conjugate momentum of the coordinate q. If the angular momentum of a particle is p, which is on a circular orbit inside a spherically symmetric mass distribution, $M(r)$, then $rM(r)$ remains constant for that particle as long as the mass inside to its orbit varies slowly over time. If $M(r)$ varies in a self-similar fashion, $r_{max}M(r_{max})$ is also constant for purely radial orbits.

Because nearly circular orbits have more accessible phase space, one can make the approximation that the orbits of dissipationless halo particles are circular. If the initial fraction of dissipational baryonic mass is $F \equiv M_b/M \ll 1$, even if dissipation happens fast, the mass internal to a dissipationless particle's orbit will not exhibit a big fractional change within one orbital period if the particle is relatively distant from the center. This ensures that, with the exception of the innermost halo particles, all orbits change adiabatically[35].

Let us look into the math done by the authors of [35]. Assume a spherically symmetric initial mass distribution. The dynamical equilibrium state $M(r)$ is represented by a constant fraction F of dissipational baryons as a function of r. The dissipated particles will then cool and fall into a final mass distribution $M_b(r)$. The dissipationless particle orbits' adiabatic invariance implies

$$r\left[M_b + M_\chi(r)\right] = r_i M_i(r_i) = r_i M_\chi(r)/(1-F), \tag{3.3}$$

Given the initial total mass distribution $M_i(r_i)$ and the final baryon mass distribution $M_b(r)$, Eq. 3.3 may be solved iteratively for the final dark matter mass distribution $M_\chi(r)$. Here r_i is the initial orbital radius and $M_\chi(r) = (1-F)M_i(r_i)$ with the assumption that the orbits of dissipationless particles do not cross. $M_i(r_i)$ is the initial mass distribution to be isothermal gas sphere with a core radius

$$a_{core} = \frac{3\sigma}{(4\pi G\rho_0)^2} \tag{3.4}$$

where σ is one dimensional rms velocity distribution and ρ_0 is the central density. The final baryonic mass distribution is assumed to be of form

$$M_b(r) \propto 1 - \left(1 + \frac{r}{b}\right)\exp(-r/b) \tag{3.5}$$

which describes radial mass distribution of a thin disk whose density in the plane of disk decreases exponentialy with the scale length b. Using the solution to Eq. 3.3 for $M_\chi(r)$ and for the relation between the initial and final dissipationless particle

radius, radial dependence density is given as

$$\rho(r) = \frac{\left[M_b^{'}(r) + M_\chi^{'}(r)\right]}{4\pi r^2} \tag{3.6}$$

where

$$M_\chi^{'}(r) = \frac{(1-F)[M_b(r) + rM_b^{'}(r) + M_\chi(r)]}{r_i - r(1-F) + \frac{M_i(r_i)}{M_i^{'}(r_i)}} \tag{3.7}$$

where the prime denotes differentiation.

While the Blumenthal method makes the restriction of only circular orbits so that only angular momentum is conserved, Young's method [36] describes an algorithm to take into account the conservation of angular momentum and radial action. The central idea of this method is to require the distribution function to be invariant during adiabatic changes[36][37],

$$f_i(J_r, J_\phi) = f_n(J_r, J_\phi) \tag{3.8}$$

where $J_r(E, L)$ is the radial action and $J_\phi \equiv L$ is the azimuthal action or total angular momentum per unit mass. The subscripts i and n refer to the initial and new halo profiles, computed in the changing potential well due to baryonic infall. This method was developed to understand the growth of black hole present at the center of star clusters adiabatically. One starts with an isothermal sphere containing a small black hole. This method can be applied to any spherically symmetric star cluster with any initial distribution function of energy E and angular momentum J. The black hole is allowed to grow for example by accreting gas, on a time scale that is slow compared to the dynamical time scale of the cluster, but is rapid when compared with relaxation time scale. It is also assumed that the relaxation time scale is much longer than Hubble time so the stellar population never has a chance to relax [37].

The authors of [37] attempted to simulate dark matter density profiles using the Blumenthal method and Young's method in order to increase the dark matter density at the center of the dark matter halo where the protostar is present, because of which the gravitational potential increases. If the fractional change in the interior mass is tiny in one dynamical crossing time, dark matter contracts adiabatically. As the collapse progresses, this dynamical crossing time decreases or becomes short at the center, meaning that the adiabatic approximation is adequate at the core. A precise calculation of dark matter density is required at this point. Because of longer crossing periods and varying fields, this estimate becomes less accurate at bigger radii. The results of star simulations done by, for example [38], show that events at greater radii have little effect on the baryonic collapse [37]. As a result, variations in the much lower density dark matter further out will have no effect on the closely linked dark matter in the core.

In the work of [37], the authors took an overdense region of $10^5 - 10^6 M_\odot$ with an NFW profile for both DM and gas, where the gas contributes 15% of that of the dark matter. The density profile of an NFW halo is[39][37]

$$\rho(r) = \frac{\rho_0}{x\,(1+x)^2} \tag{3.9}$$

where $x = r/r_s$,r_s is the break radius of the profile, and $\rho_0 \equiv 4\rho(r_s)$ sets the density scale. With redshift z, the critical density of the Universe varies as

$$\rho_c(z) = \frac{3H^2(z)}{8\pi G} \tag{3.10}$$

where for a flat Universe, the Hubble parameter is given as

$$H^2(z) = H_0^2 \left[\Omega_m(1+z)^3 + \Omega_\Lambda\right] \tag{3.11}$$

The authors of [37] assumed the values for the current matter density as $\Omega_m \sim 0.25$, and Ω_Λ, the dark energy term on the right hand side was neglected at the redshift being considered. For redshift $z = 19$, $H^2 \sim 2000H_0^2$, and Hubble constant $H_0 = 100hkms^{-1}Mpc^{-1}$ with $h^2 \sim 0.5$. Therefore, for an NFW halo mass $M = 7 \times 10^5 M_\odot$, and

$$\frac{3M}{4\pi r^3} = 200\rho_c(z) \tag{3.12}$$

gives $r \sim 123pc$.

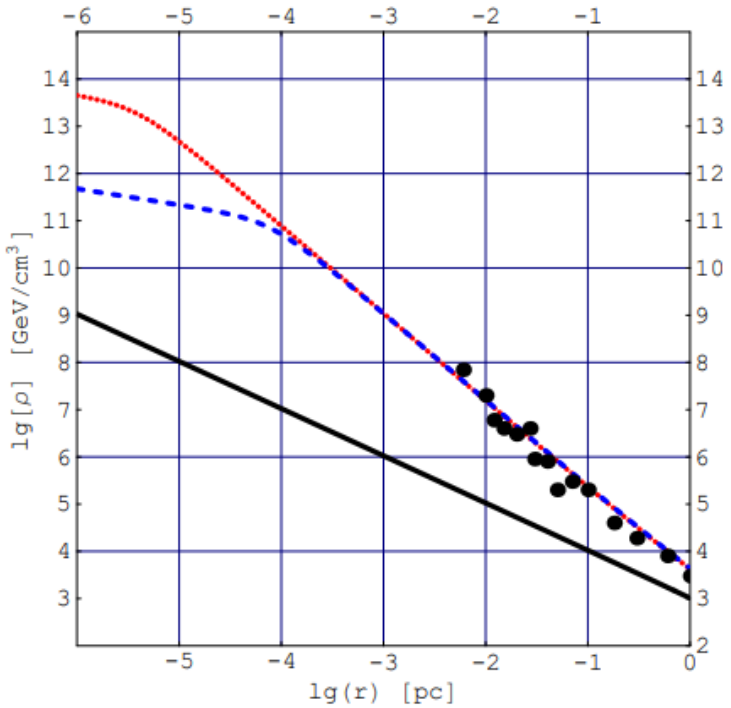

FIGURE 3.1: For an initial NFW profile, adiabatically contracted dark matter profiles for the first collapsing protostars utilizing the Blumenthal approach (solid black line). The blue dashed lines represent hydrogen densities of $n = 10^{13}cm^{-3}$, while the red dotted lines represent hydrogen densities of $n = 10^{16}cm^{-3}$. The black dots show the dark matter densities obtained from the simulations done by [38]. Credit: [37]

The Fig.3.1, (credit:[37]), shows the dark matter density profile contracted via Blumenthal method of adiabatic contraction[35]. The authors concluded that the dark matter density at the outer edge of the baryonic core is roughly given as $\rho_\chi \simeq 5GeV/cm^{-3}(n/cm^3)^{0.81}$ and scales as $\rho_\chi \propto r^{-1.9}$ outside the core. The black dots show the dark matter densities obtained from the simulations done by [38] Figure

2A, corresponding to $n = 10^{13} cm^{-3}$. One can see an excellent agreement among the two results.

The authors of [38] obtained excellent density profiles for the collapsing protostellar gas in to very small radii, they found dark matter density profiles only upto radii that are several orders of magnitude larger. The slope of the curves in Figure 3.1, the results of [37] and [38] are similar and scales as $\rho_\chi \propto r^{-1.9}$. The authors of [37] used the slope of [38] and extrapolated it inwards to smaller radii and to higher densities, and obtained the same dark matter densities as with their adiabatic contraction approach as one can see in Fig.3.1.

In the Fig. 3.2 (Credit: [37]), the authors started from initial NFW profile (represented by dashed lines) and plots contracted density profiles using the Blumenthal method for adiabatic contraction (represented by dotted lines) and the Young method (represented by the solid lines) for total dark matter halo mass $7 \times 10^5 M_\odot$ and concentration parameter $c = 2$ at redshift $z = 19$. The top panel depicts the dark matter density profile, while the bottom panel depicts the contained dark matter mass $M(r)$ as a function of radius. Both profiles are displayed in a $10^{-4} pc$ radius.

The main result of the paper [37] is that the densities computed in both ways differ by no more than a factor of 2. In certain cases, the Blumenthal method produces a greater density, while in others, the Young's method produces a higher density.The difference, however, is never more than a factor of 2. The density of dark matter does not increase at smaller radii for low gas densities $n = 10^4 cm^{-3}$ because of the minimal quantity of gas mass at these radii. However, at gas densities of $n = 10^8 cm^{-3}$ and above, the dark matter density is considerably increased owing to adiabatic concentration using either techniques. The plot indicates that for small radii, the Blumenthal technique predicts a lower density than the Young's method for the two lower density stars. This is due to the fact that a halo particle on a non-circular orbit spends some of its time at large radii, where the inner compressing mass is greater than when it is near to the center. As a consequence, even if there is little compressing material inside that radius, the mean density might be increased, which can happen only if the star has a diffused core.

For $n = 10^6 cm^{-3}$ and $n = 10^3 cm^{-3}$ curves do not look different in the plot. The curves begins to diverge at the radius $10^{-4} pc$ and the higher gas density would lead to very high dark matter density at smaller radii. The plot is unable to show this point because of lack of resolution.

The authors of [37] therefore concludes that, starting from an NFW profile, it can be confirmed that the dark matter density in the inner regions of the protostellar cloud is substantially enhanced due to contraction during gas collapse.

3.1.2 Criteria 2: Dark matter annihilation products gets trapped inside the star

WIMP annihilation generates energy at the rate per unit volume specified by Eq. 3.2. When the gas density is low in the early phases of PopIII star formation, much of the energy is radiated away [40]. When the gas compresses and density rises, however, a portion of the annihilation energy is absorbed by the gas, heating it up at a rate of $f_Q Q_{DM}$ per unit volume. The WIMP model determines the annihilation products and their energy spectrum.(For annihilation of Neutralinos at low velocity refer to Chapter 2.) For the neutralino dark matter, the annihilation products typically are 1/3 neutrinos, 1/3 photons and 1/3 charged stable particles i.e. electrons and positrons. Since neutrinos escape from the cloud without depositing significant

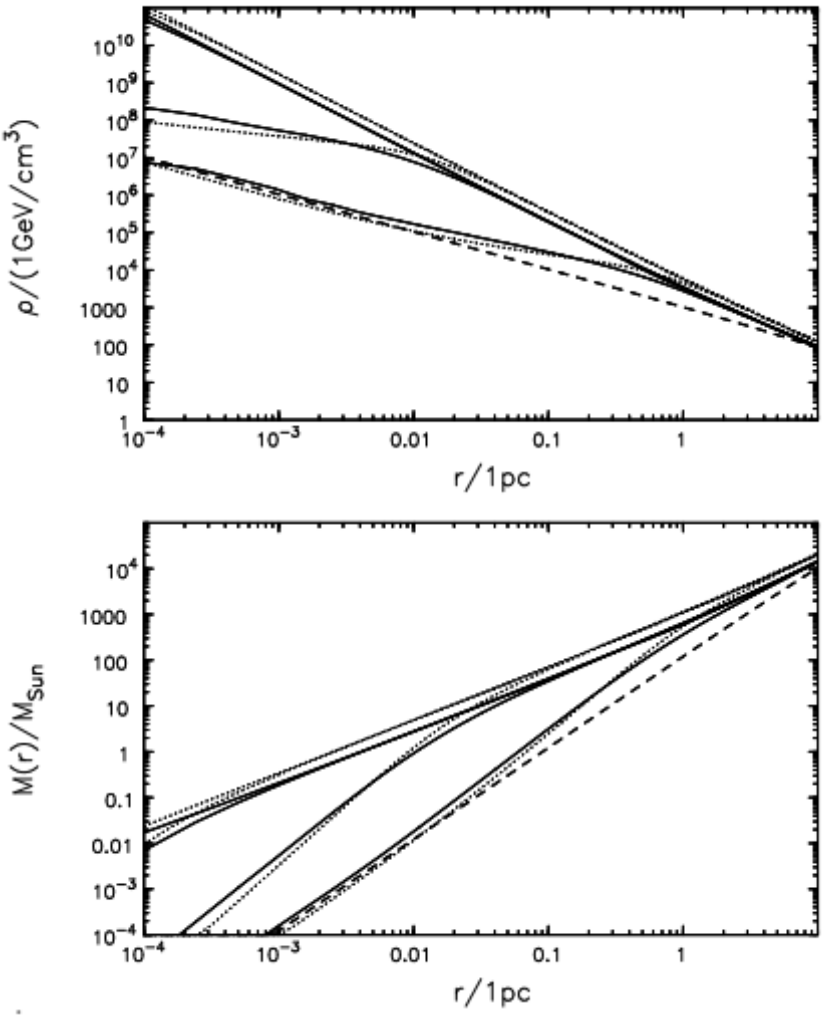

FIGURE 3.2: Adiabatic dark matter profiles for the first collapsing protostars using the Blumenthal approach (dotted line) and Young's technique (solid line) for an initial NFW profile (dashed line) for $M_{vir} = 5 \times 10^7 M\odot, c = 2$, and $z = 19$. The top panel depicts the density profiles of dark matter, while the bottom panel depicts the contained dark matter mass as a function of radius. The four sets of curves in each panel correspond to baryonic core densities of $n = 10^4, 10^8, 10^{13}$, and $10^{16} cm^{-3}$. The difference between these two approaches for determining DM densities is less than factor of two. Credit: [37]

amount of energy, the rest can deposit their energy to the core, therefore[1][2],

$$f_Q \simeq 2/3 \tag{3.13}$$

For a $100GeV$ WIMP, the energy due to electrons and photons is trapped inside the star once the hydrogen density exceeds $\sim 10^{13} cm^{-3}$. Around 2/3 of the annihilation energy is trapped inside the collapsing gas. This thermalizes the gas and provides a heat source for the resulting dark star[2].

Ionization causes electrons in hydrogen below the threshold energy $E_c \approx 280 MeV$ to lose energy. More energetic electrons lose energy to the gas through bremsstrahlung photon emission. When these bremsstrahlung photons pass near a gas nuclide, they

produce electrons and positrons, which can then produce more bremsstrahlung photons. This initiates an electromagnetic (EM) cascade, which is a series of photon, electron, and positron conversions. Photons with energies greater than $\approx 100MeV$ also start an EM cascade. Lower energy photons use Compton scattering to deliver the majority of their energy to electrons in gas.[1][2].

Analytic Prescription for WIMP Annihilation Heating

The author of [41] investigated the effects of WIMPs annihilation on the formation of PopIII.1 stars and derived an analytical expression for the dark matter heating rate, including a simplified treatment of radiative transport. We will look into it in detail. It should be noted that the following calculations are an approximation and does not solve the full radiation transfer problem. These calculations are done by authors of [41] and is presented as is and entire credit is given to the authors of [41].

Let us consider WIMPs with mass m_χ, $\langle \sigma_a v \rangle$ is the WIMP annihilation cross section times the relative velocity, averaged over the momentum distribution of the WIMPs, assuming to be equal to $3 \times 10^{-26} cm^3 s^{-1}$. The number of photons produced by WIMP annihilation per unit volume, per unit time and per unit energy, at point $r^{'}$ is given as

$$\frac{d\mathcal{N}_\gamma}{dE_\gamma} = \frac{\rho_\chi^2(r^{'}) \langle \sigma_a v \rangle}{2m_\chi^2} \frac{dN_\gamma}{dE_\gamma} \tag{3.14}$$

where $\rho_\chi(r^{'})$ is the WIMP density at $r^{'}$ and $\frac{dN_\gamma}{dE_\gamma}$ is the number of the photons produced per unit energy per annihilation.

Let us consider electron scattering at a location r, by photons produced at location $r^{'}$. Some of these photons produced at point $r^{'}$ will scatter off electrons before reaching point r. The number of photons reaching point r without scattering is smaller than the number produced at $r^{'}$ by the factor S given as:

$$S\left(r^{'}, r, E_\gamma, \theta\right) = \begin{cases} \exp\left[-\sigma_{e^-\gamma}(E_\gamma) \int_0^{S_+} ds n_e(s)\right] & r^{'} < r \\ \exp\left[-\sigma_{e^-\gamma}(E_\gamma) \int_0^{S_-} ds n_e(s)\right] \times \left(1 + \exp\left[-\sigma_{e^-\gamma}(E_\gamma) \int_{S_-}^{S_+} ds n_e(s)\right]\right) & r^{'} > r \end{cases} \tag{3.15}$$

where $s_\pm = r^{'} \cos\theta \pm \sqrt{r^2 - r^{'2} \sin^2\theta}$ and $\sigma_{e^-\gamma}$ is the cross section. The above equation takes the fact into consideration that photons can pass through the sphere $r = constant$ twice when $r^{'} > r$. It should also be noted that S is a function of the angle θ between the path of the photon and the line joining $r^{'}$ with the center of the spherical cloud.

Consider photons travel from $r^{'}$ to r. The number of scattering events per unit energy, per unit time, per unit volume at r, along the path θ is

$$\frac{d\mathcal{N}_s}{dE_\gamma} = \frac{\langle \sigma_a v \rangle}{2m_\chi^2} \frac{dN_\gamma}{dE_\gamma} \int dr^{'} r^{'2} \rho_\chi^2(r^{'}) S(r^{'}, r, E, \theta) \times \frac{n_e(r) \sigma_{e^-\gamma}(E_\gamma) \delta s(r^{'}, r, \theta)}{r^2 \delta r} \tag{3.16}$$

where δs is the distance between r and $r + \delta r$, along the path of the photon:

$$\delta s = \frac{\delta r}{\sqrt{1 - \frac{r^{'2}}{r^2} \sin^2\theta}} \tag{3.17}$$

Since all angles θ are equally probable, the angle averaged quantity is given as:

$$\left\langle \bar{S}(r^{'},r,E)\right\rangle = \frac{1}{2}\int_0^{\theta_{max}} sin\theta \frac{S(r^{'},r,E,\theta)}{\sqrt{1-\frac{r^{'2}}{r^2}sin^2\theta}}d\theta \tag{3.18}$$

where $\theta_{max} = \begin{cases} \theta_{max} = \pi & r^{'} < r \\ \theta_{max} = \sin^{-1}(r/r^{'}) & r^{'} > r \end{cases}$

If we set the limit that the wavelength of the incident radiation is much smaller than the Bohr radius, one may assume that the radiation sees a gas of electrons and protons, rather than bound atoms. Therefore the scattering cross section $\sigma_{e^-\gamma}(E_\gamma)$ is given by the *Klein-Nishina formula*(for example [42]):

$$\sigma_{e^-\gamma}(y) = \sigma_T f_\sigma(y), \tag{3.19}$$

where σ_T is the Thomson cross section for electrons and proton scattering is less important owing to the large mass. f_σ is given by

$$f_\sigma(y) = \frac{3}{8}\left[\frac{2(1+y)}{(1+2y)^2} + \frac{\ln(1+2y)}{y} - \frac{2}{1+2y} + \frac{2(1+y)^2}{y^2(1+2y)} - \frac{2(1+y)\ln(1+2y)}{y^3} + \frac{2}{y^2}\right] \tag{3.20}$$

where $y = E_\gamma/m_e$. E_{abs} is the average energy transferred to an electron in a scattering event:

$$E_{abs} = m_\chi f_E(E_\gamma) \tag{3.21}$$

where

$$f_E = \frac{E_\gamma}{m_\chi} + \frac{m_e}{m_\chi} - \frac{m_e}{2m_\chi}\ln\left(1+\frac{2E_\gamma}{m_e}\right). \tag{3.22}$$

Let us make assumption that the energetic electrons after scattering remain in the gas cloud and serve to heat up the cloud. As long as low energy photons do not contribute significantly to the heating rate, one may maintain the approximation that $E_\gamma >> 13.6eV$, while performing the integral:

$$H(r) = \frac{\langle\sigma_a v\rangle\, n_e \sigma_T}{2m_\chi r^2}\int_0^{m_\chi} dE_\gamma f_E(E_\gamma) f_\sigma(E_\sigma)\frac{dN_\gamma}{dE_\gamma}(E_\gamma)\int_0^r dr^{'} r^{'2}\rho_\chi^2(r^{'})\left\langle \bar{S}(E_\gamma,r^{'},r)\right\rangle. \tag{3.23}$$

$H(r)$ gives the heating rate, energy per unit volume per unit time, at point r due to primary photons, under the approximate assumption that all primary photon energy is transferred to the gas at the location of the first collision.

To calculate the heating rate at point r using the Eq(3.23), one need to consider dark matter in a finite volume around r. The size of this volume is determined by the function $\left\langle S(r^{'},r,E)\right\rangle$. When this volume is small compared to the size of the halo, one may expect most of the energy released by dark matter annihilation to be absorbed by the gas cloud. $\left\langle S(r^{'},r,E)\right\rangle$ is larger when $r^{'}$ is closer to r. More energetic photons penetrate farther through the gas because of their smaller scattering cross section.

3.1.3 Criteria 3: Dark matter-dark matter annihilation is the major heating/cooling mechanism in the star

For a WIMP mass $m_\chi = 100GeV$ and $1GeV$, a critical transition occurs when the gas density reaches $n > 10^{13}cm^{-3}$ and $n > 10^{9}cm^{-3}$ respectively. Above this gas density, dark matter heating dominates over all the relevant cooling mechanisms, the most important being H_2 cooling[2].

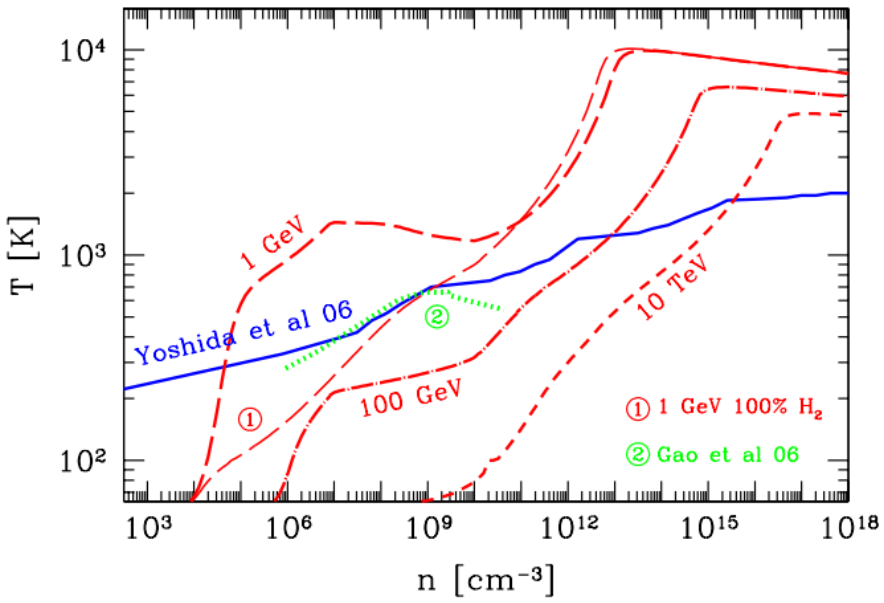

FIGURE 3.3: The critical temperature (red dashed lines) is compared to conventional evolution tracks in the temperature-density phase plane is shown. The solid blue and dotted green lines show the protostellar gas evolution from simulations of [43] and [44] respectively. The red dashed lines mark $T_c(n)$ for $m_\chi = 1GeV$ with H_2 density from simulations, $m_\chi = 1GeV$ assuming $100\%H_2$, $m_\chi = 100GeV$ and $m_\chi = 10TeV$. Dark matter heating supersedes over cooling in the evolution of the core of the star at the intersection of the blue/green and red lines.. Credit: [1]

Figure 3.3 is the simulation result of [1]. In the figure, it is shown a comparison of critical temperature ($T_c(n)$) to typical evolution tracks in the temperature-density phase plane. The solid blue line and dotted green line show the temperature evolution of the protostellar gas in the simulation without dark matter of [43] and [44] respectively. The critical temperature is indicated by the red dashed and dot-dashed lines. Dark matter heating takes precedence over all cooling/heating processes below these lines. The figure depicts findings for a canonical $3 \times 10^{-26}cm^3/sec$ annihilation cross section for a range of WIMP masses ranging from $1GeV$ to $10TeV$. Because the heating rate scales as $\langle\sigma v\rangle / m_\chi$, these similar curves apply to a wide range of cross sections for a given WIMP mass.

The authors of [1] (from the figure 3.3), concluded that the blue/green and red lines always cross, regardless of WIMP mass or H_2 fraction. "*This is a robust result*". As soon as the core density hits this critical threshold, dark matter heating takes over inside the core, altering its evolution.The crossing point for tiny H_2 fractions for $m_\chi = 1GeV$ is at low densities, approximately $n \sim 10^5cm^{-3}$. When the H_2 fraction is increased, cooling prevails for a longer period of time, but not forever.

At constant density and composition, the crossover point is stable despite temperature variations. If the temperature rises over the critical point, cooling takes over and pushes the temperature back down to the critical point. When the temperature drops, heating takes over and the temperature drops. This is due to the fact that the H_2 cooling rate rises with temperature, but dark matter heating is temperature independent. Once the dark matter annihilation products are trapped within the protostellar core, heating takes precedence over H_2 cooling. Therefore for $100GeV$ neutralino dark matter, the heating rate from dark matter annihilation exceeds the rate of hydrogen cooling when the gas density reaches critical value of $\sim 10^{13}cm^{-3}$, and for $1GeV$ dark matter the critical gas density is 10^9cm^{-3}. The protostellar core is prevented from collapsing and cooling further.

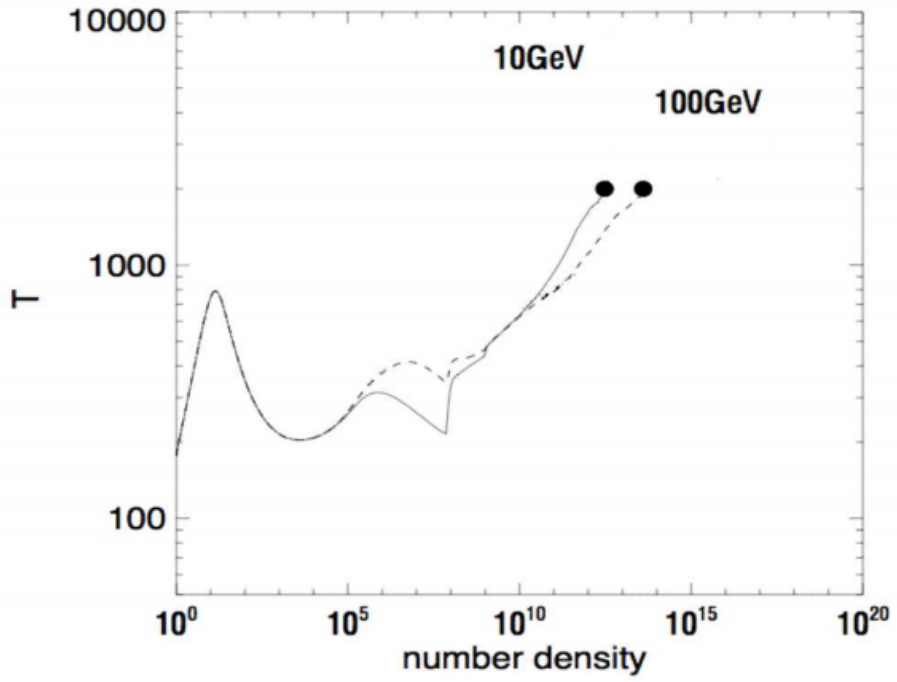

FIGURE 3.4: Temperature (in degrees K) vs hydrogen density (in cm^{-3}) for the protostars, including dark matter annihilation, for two unique dark matter particle masses, 10 GeV and 100 GeV. Moving to the right in the image refers to moving ahead in time. When the "dots" are achieved, dark matter annihilation overcomes H2 cooling, and a Dark Star is created. Credit [2][45]

The figure 3.4 (credit: [2][45]), shows the evolutionary tracks of the protostar in the temperature-density phase plane with dark matter heating included for the two dark matter particle masses i.e. $10GeV$ and $100GeV$. Moving towards right in the plot is like moving ahead in time. Once the black dots are approached, dark matter annihilation heating overshadows the cooling inside the star and *Dark Star* phase commences. The size of the core is $\sim 17A.U.$ and mass $0.6M_\odot$ for $100GeV$ mass WIMPs.

In the work [41], following results were further presented: If one assumes the dark matter profile is self similar, and extending inwards from the dark matter dominated regime with $\rho_\chi \propto r^{-\alpha_\chi}$, then for $100GeV$ dark matter particle and $\alpha_\chi \simeq 2.0$, the dark matter annihilation heating exceeds baryonic cooling for densities $n >$

$10^{14} cm^{-3}$, in agreement to [1]. The authors of [41] also concluded that if adiabatic contraction occurs on the scales $0.03pc$ to $\sim 1pc$ and creates an approximately self-similar power law density structure, then the dark matter annihilation heating dominates cooling for all halos and all WIMP masses considered on scales inside $\sim 3 \times 10^{-5} pc$ and more typically inside $\sim 10^{-4} pc$ or $\sim 20 AU$.

The restriction imposed by third condition for dark star formation is best expressed in terms of quantity $f_Q \langle \sigma v \rangle / m_\chi$, where, f_Q is the fraction of energy trapped by the gas, $\langle \sigma v \rangle$ is the annihilation cross section, and m_χ is the dark matter particle mass [46]. Figure 3.5 (credit: [46]) shows the critical lines for the dark star formation. The third condition, therefore, mathematically can be written as [46]

$$f_Q \frac{\langle \sigma v \rangle}{m} > 1 \times 10^{-32} cm^3 s^{-1} GeV^{-1} \tag{3.24}$$

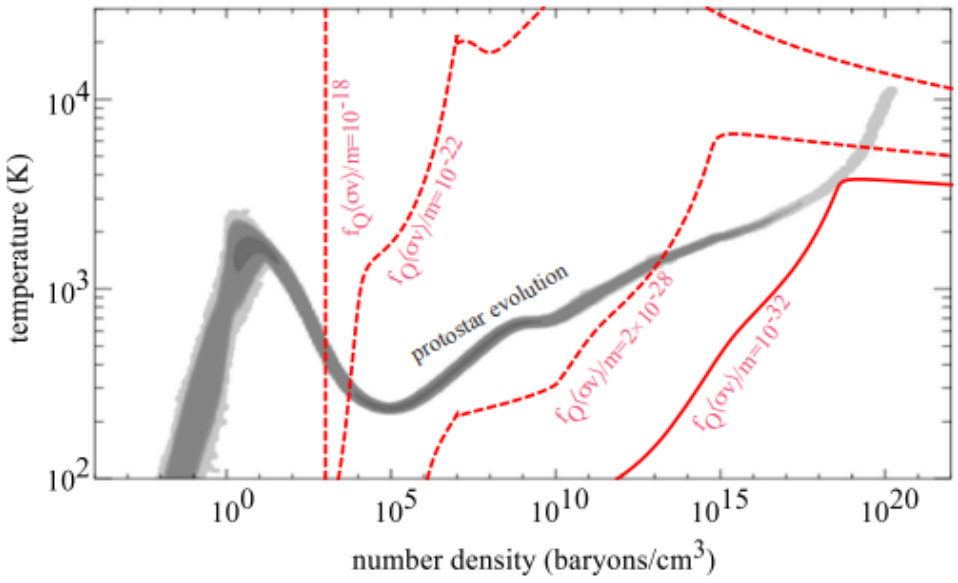

FIGURE 3.5: The following conditions must be met in order for a dark star to form. The gray band illustrates possible protostar formation routes generated from Λ CDM cosmology numerical simulations. The red lines are crucial curves when the rate of dark matter annihilation equals the rate of protostellar gas cooling. At the junction of a critical line and the gas evolution track, a dark star is born. No dark star can form for $f_Q \frac{\langle \sigma v \rangle}{m} < 10^{-32} cm^3 s^{-1} GeV^{-1}$ Credit:[46]

3.2 Models of Dark Matter that can form Dark Stars

Till now we have seen that WIMP model is the favoured dark matter model for Dark Star formation. This section will discuss the work of [46] that looks into different models of dark matter, if the dark star formation is possible or not. This work looks into MSSM, Kaluza-Klein, Leptophilic, and Neutrinophilic dark matter models. All the calculations and arguments discussed here are work of [46] and all credits are given to the authors of [46].

The motivation of [1] to choose $\langle \sigma v \rangle = 3 \times 10^{-26} cm^3 s^{-1}$ was by the assumption that the dark matter WIMPs are produced thermally in the early Universe, i.e. the

WIMPs are generated in the matter-antimatter collisions at temperatures higher than $T_{fo} \sim m/20$, which is the temperature after which WIMP production freezes out and the comoving WIMP number density remains approximately constant given by Eq.1.1[46]. Furthermore, the authors of [1] assumed that the velocity-averaged annihilation cross-section times the relative velocities at the freeze out time and in a dark star are equal i.e., $\langle \sigma v \rangle_{ds} = \langle \sigma v \rangle_{fo}$. But the relation between $\langle \sigma v \rangle_{fo}$ and Ω_χ is more complex and $\langle \sigma v \rangle_{ds}$ may differ from $\langle \sigma v \rangle_{fo}$ because the cross section depends on the velocity of the WIMP[46].

Therefore the average WIMP speed at freeze-out is of the order[46]

$$v_{fo} \sim \sqrt{\frac{T_{fo}}{m}} \sim \frac{c}{\sqrt{20}} \sim 7 \times 10^4 km/s \tag{3.25}$$

but the typical speed of WIMPs in a dark star can be estimated from the orbital velocity

$$v_{ds} \sim \sqrt{\frac{GM}{r}} \sim 30 - 300 km/s \tag{3.26}$$

3.2.1 MSSM

Since there are more than 100 free parameters, the MSSM provides a variety of examples in which the annihilation cross section in the dark star is different from the annihilation cross section at the time of freeze out. There are various ways in which $\langle \sigma v \rangle_{fo} \neq \langle \sigma v \rangle_{ds}$. The quantity σv depends on the relative velocity. This includes three cases[46]:

- p-wave annihilation in which $\sigma v = a + bv^2$ is dominated by the term bv^2 at freeze out, where a and b are constants;
- resonant annihilation where σv follows a Breit-Wigner function $\frac{(1+v^2)^c}{[(v^2+\delta^2)+\gamma^2]}$, where δ, γ. and c are constants.
- Owing to the increasing particle kinetic energy, a threshold annihilation channel is kinematically available at freeze-out but not in a dark star.

Moreover, the annihilation reactions that define the length of the freeze-out may or may not be related to the star's neutralino-neutralino annihilation. The freeze-out temperature is most likely high enough to transform neutralinos into heavier supersymmetric particles that annihilate considerably more quickly, a process known as coannihilation. The annihilation cross section of the heavier supersymmetric particles, which is not the same as the neutralino-neutralino annihilation cross section, determines the neutralino relic density[46].

To illustrate these cases, the authors of [46] considered effective MSSM (effMSSM) with 8 free parameters fixed at electroweak scale. These are:

1. CP-odd Higgs Boson mass (m_A)
2. the ratio of neutral Higgs vacuum expectation values (tan β)
3. the Higgs mass parameter (μ)
4. the gaugino mass parameter $(M_1 and M_2)$
5. the slepton mass parameter $(m_{\tilde{l}})$

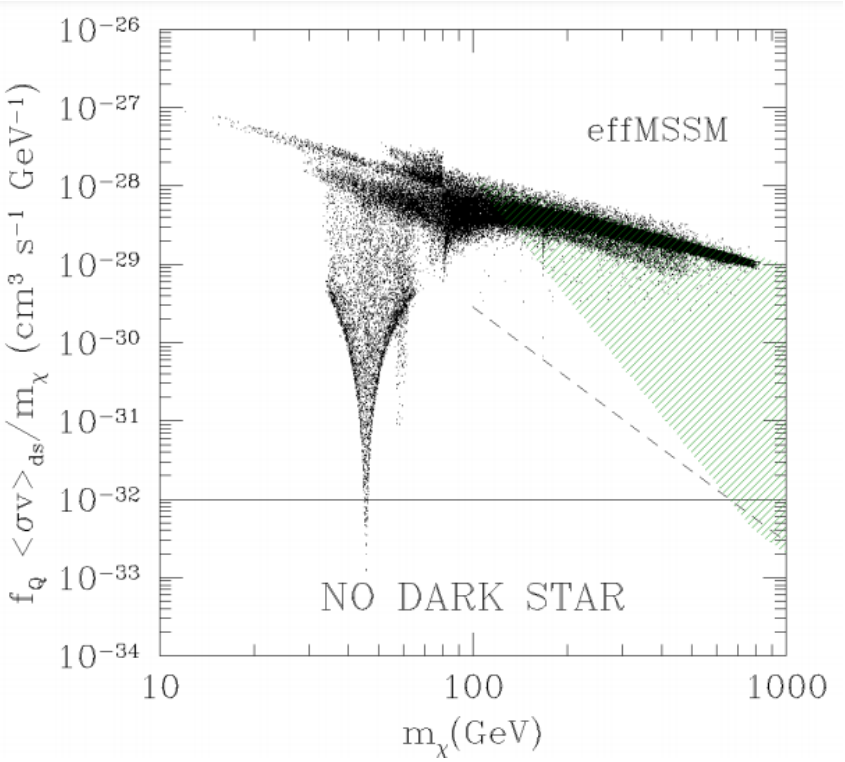

FIGURE 3.6: For an eight-parameter effective MSSM model, the figure shows a scatter plot for $f_Q \langle\sigma v\rangle_{ds} / m_\chi$ which is function of the neutralino mass m_χ. A dark star cannot form below the horizontal line($f_Q \langle\sigma v\rangle_{ds} / m_\chi = 10^{-32}$). Credit:[46]

6. the squark mass parameter ($m_{\tilde{q}}$)
7. the ratio $A_{\tilde{\tau}}/m_{\tilde{l}} = A_{\tilde{t}}/m_{\tilde{q}} = A_{\tilde{b}}/m_{\tilde{q}}$
8. the trilinear couplings $A_{\tilde{\tau}}$, $A_{\tilde{t}}$ and $A_{\tilde{b}}$ of the third generation of sleptons and squarks.

Fig.3.6(credit: [46]) shows the values of combination $f_Q < \sigma v > /m_\chi$ as a function of neutralino mass m_χ. Figure 3.6 depicts the following: (i) P-wave annihilation causes the spread of points along path sloping down to the right; (ii) resonant annihilation through Z-boson causes the V-shaped pattern at $m_\chi \sim 45GeV$. Other resonant annihilations are visible at $m_\chi \sim 60GeV$, such as the lightest Higgs boson with a mass ranging from $115GeV$ to $120GeV$; (iii) threshold annihilation causes the "fingers" of points descending from the p-wave band points; and (iv) the shaded region on the right of $m_\chi \sim 100GeV$ is caused by possible coannihilation with staus. An equivalent boundary for sneutrino coannihilations is shown by the dashed line [46].

The p-wave term bv^2 in σv makes a major contribution at the freeze out. But contribution to σv is suppressed in terms of the evolution of the dark star. Therefore, for a $1M_\odot$ dark star, $(v_{ds}/v_{fo})^2 \sim 2 \times 10^{-9}$. In this instance, $\langle\sigma v\rangle_{ds} \simeq a$; $\langle\sigma v\rangle_{fo} \simeq b\langle v^2\rangle \simeq b/20$. Their ratio is determined by the particle physics parameters inside the coefficients a and b. In the plot, p-wave annihilation gives rise to a spread in $f_Q \langle\sigma v\rangle_{ds} / m$ of about one order of magnitude, shown by bands of points sloping down to the right[46].

The z-resonance at $m_\chi \sim 45GeV$ is an example of resonant annihilation. The resonant part of the neutralino-neutralino annihilation cross section is given by[46]

$$(\sigma v)_z = \beta_f \frac{g_{eff}^4}{m_\chi^2} \frac{(s - m_Z^2)^2}{(s - m_Z^2)^2 + \Gamma_Z^2 m_Z^2} \tag{3.27}$$

where β_f is the speed of the final products in the units of speed of light, and g_{eff} has the coupling constants and the mixing angles of the neutralinos and of the final particles involved. The velocity dependence of the cross section can be calculated by putting $s = 4m_\chi^2(1 + v^2)$ and neglecting mass of the final products,

$$(\sigma v)_Z = \frac{g_{eff}^4}{m_\chi^2} \frac{(v^2 + \delta)^2}{(v^2 + \delta)^2 + \gamma^2} \tag{3.28}$$

where $\delta = 1 - m_Z^2/(4m_\chi^2)$ and $\gamma = \Gamma_Z m_Z/(4m_\chi^2)$[46]. On resonance, $2m_\chi = m_Z$ or $\delta = 0; \gamma = \Gamma_Z/m_Z = 0.0273$, the velocity-averaged $\langle(\sigma v)_Z\rangle$ has varied values when it comes to freeze out ($v \simeq 0.2c$) and in dark stars ($v \simeq 0$). During freeze out, using $T_{fo} = m_\chi/20$, the thermal average of $(v)_Z$ is given as

$$\langle(\sigma v)_Z\rangle_{fo} = 0.97 \frac{g_{eff}^4}{m_\chi^2} \tag{3.29}$$

In dark star, for $v = 30km/s$ the resonance occurs

$$\langle(\sigma v)_Z\rangle_{ds} = 1.3 \times 10^{-13} \frac{g_{eff}^4}{m_\chi^2} \tag{3.30}$$

Since $\langle(\sigma v)_Z\rangle_{fo} \sim 3 \times 10^{-26} cm^3/s$ gives the correct relic density, therefore,

$$\langle(\sigma v)_Z\rangle_{ds} = \frac{1}{13} \langle(\sigma v)_Z\rangle_{fo} \tag{3.31}$$

This difference in values give rise to the V-shape around $m_\chi = m_Z/2 \sim 45GeV$. At $m_\chi = m_H/2 \sim 60GeV$ similar resonant characteristics through the lightest Higgs boson emerge superposed[46].

In a particular channel, threshold annihilation happens when the mass of neutralino is little less than half of the total mass of the by products of the annihilation ($\chi\chi \to WW$). The reaction needs kinetic energy, which is accessible during the freeze out time, due to the neutralinos' relatively high temperature, but not at their low velocities in a dark star. As a result, these annihilations occur at freeze out rather than in stars. Therefore, $\langle(\sigma v)_Z\rangle_{ds} < \langle(\sigma v)_Z\rangle_{fo}$. Figure 3.6 depicts the "fingers of points" falling from the p-wave band at $m_\chi \sim 80GeV$ for the WW channel and again at $m_\chi \sim 190GeV$ for the $t\bar{t}$ channel. Even after the suppression of $\langle(\sigma v)_Z\rangle_{ds}$, it is not that big enough to get it outside the region in which dark star formation is possible[46].

Finally, for coannihilation, effective annihilation cross section determines the relic density, $\langle(\sigma v)_Z\rangle_{eff}$. This is the average of all reactions which involves neutralino and coannihilation particles' annihilation cross sections. In case of stau coannihilation (because the experimental lower bound on the stau mass i.e. $m_{\tilde{\tau}} \gtrsim 98GeV$, is smaller than the lower bound on squark masses and thus coannihilation region in

parameter space is larger), the effective annihilation cross section is given approximately as[46]

$$\langle\sigma v\rangle_{eff} = \frac{\langle\sigma v\rangle_{\chi\chi} + \langle\sigma v\rangle_{\chi\tilde{\tau}}\, e^{-(m_{\tilde{\tau}}-m_\chi)/T_{fo}} + \langle\sigma v\rangle_{\tilde{\tau}\tau}\, e^{-2(m_{\tilde{\tau}}-m_\chi)/T_{fo}}}{1 + e^{-2(m_{\tilde{\tau}}-m_\chi)/T_{fo}} + e^{-(m_{\tilde{\tau}}-m_\chi)/T_{fo}}} \tag{3.32}$$

where, total annihilation cross section, $\langle\sigma v\rangle_{\chi\chi}$ for $\chi\chi$ →anything; $\langle\sigma v\rangle_{\chi\tilde{\tau}}$ for $\chi\tilde{\tau}$ →anything; $\langle\sigma v\rangle_{\tau\tilde{\tau}}$ for $\tilde{\tau}\tilde{\tau}$ →anything

Also, since $\tilde{\tau}\tilde{\tau} \rightarrow \tau\tau$ are electromagnetic processes, then $\langle\sigma v\rangle_{\tilde{\tau}\tilde{\tau}} \sim \frac{\alpha^2}{m_{\tilde{\tau}}^2} >> \langle\sigma v\rangle_{\chi\chi} \sim \frac{\alpha^2 m_\tau^2}{m_{\tilde{\tau}}^4}$(for $\chi\chi \rightarrow \tau\tau$)

For $m_{\tilde{\tau}} = 100GeV$, we have $\langle\sigma v\rangle_{\tilde{\tau}\tilde{\tau}}$ / $\langle\sigma v\rangle_{\chi\chi} \sim m_{\tilde{\tau}}^2/m_\tau^2 \gtrsim 3\times10^3$.

For $m_{\tilde{\tau}} = 1TeV$, $\langle\sigma v\rangle_{\tilde{\tau}\tilde{\tau}}$ / $\langle\sigma v\rangle_{\chi\chi} \sim m_{\tilde{\tau}}^2/m_\tau^2 \gtrsim 3\times10^5$

With a right choice of the mass difference of $m_{\tilde{\tau}} - m_\chi$ in equation 3.32, it is possible to have a three-order-of-magnitude larger effective annihilation cross section than that of the $\chi\chi$ annihilation cross section and a three-order-of-magnitude lower relic density compared to without coannihilations. This arguments allows us to estimate a lower limit on $\langle\sigma v\rangle_{ds}$ in a dark star using just annihilation cross section for $\chi\chi \rightarrow \tau\tau$, without requiring to compute the relic density in presence of coannihilation [46]

$$\langle\sigma(\chi\chi \rightarrow \tau\tau)v\rangle_{ds} \geq \frac{\pi\alpha^2}{32\cos^4\theta_W}\frac{m_\tau^2}{m_{\tilde{\tau}}^2} \tag{3.33}$$

Setting $m_{\tilde{\tau}} = m_\chi$ as the suitable value for stau coannihilations, bremsstrahlung ($\chi\chi \rightarrow \tau\tau\gamma$) contributes to $\langle\sigma v\rangle_{ds}$ which, at large neutralino masses, exceeds the lower limit already computed in equation 3.33. Therefore[46],

Therefore,

$$\langle\sigma(\chi\chi \rightarrow \tau\tau\gamma)v\rangle_{ds} \simeq \frac{\alpha^3}{m_\chi^2} \tag{3.34}$$

Equations 3.33 and 3.34 are used to plot the shaded region to the right of $m_\chi \sim 100GeV$ in figure 3.6[46]

$$f_Q\frac{\langle\sigma v\rangle_{ds}}{m_\chi} \geq \begin{cases} 1.2\times10^{-28}\frac{cm^3}{sGeV}\left(\frac{100GeV}{m_\chi}\right)^5 & m_\chi \lesssim 800GeV \\ 2\times10^{-30}\frac{cm^3}{sGeV}\left(\frac{100GeV}{m_\chi}\right)^3 & m_\chi \gtrsim 800GeV \end{cases} \tag{3.35}$$

For the bremsstrahlung of gamma rays, $f_Q = 1$, dark stars can form for $m_\chi \leq 880GeV$. If $f_Q \leq 0.86$, bremsstrahlung has no effect on the largest possible mass of neutralino generating dark stars, which may develop for $m_\chi \leq 830GeV$. The annihilation cross section in dark stars can be as low as the shaded area's bottom boundary, but the correct relic density is formed by a considerably greater effective annihilation cross section. Dark stars can still develop in the majority of the shaded zone, with the exception of larger masses when the shaded area surpasses the "no dark stars" sector limit.[46].

Therefore it can be seen that MSSM model of dark matter does support the formation of the dark stars.

3.2.2 Kaluza-Klein Model of Dark Matter

With the scenario that the Standard Model exists in five or six dimensions and the extra dimensions are compressed at radius $\simeq 1/TeV$, the lightest Kaluza-Klein particle is stable and can be a suitable dark matter candidate. The Kaluza-Klein number can be retained in a consistent manner in all interactions involving an even number of odd Kaluza-Klein number particles[47].

The KK photon (more accurately the KK modes of the $U(1)_Y$ gauge boson), and the KK neutrinos are two major KK candidates for dark matter. Through the t-channel exchange of KK fermions, the KK photon annihilates to quarks and leptons, and its relic abundance is consistent with its mass measurement of roughly $1TeV$. A KK neutrino's annihilation cross section to quarks and leptons is mediated by t- or s-channel gauge boson exchange, but annihilation into gauge bosons is governed by t-channel KK lepton exchange or s-channel gauge bosons. If we consider only one flavour of the KK neutrino, we get the right relic density for a mass of about $1.5TeV$. Including three flavours, because of coannihilation between distinct flavors, the effective cross section shrinks, and the mass required to achieve the right relic density is roughly $1TeV$ [46].

In the situation of KK dark matter, the s-wave annihilation cross section is always substantial for both the KK photon and the KK neutrino, hence the difference between $\langle\sigma v\rangle_{fo}$ and $\langle\sigma v\rangle_{ds}$ is small. Furthermore, the temperature within the dark star is very low in relation to the freeze out temperature, and coannihilations with the other particles, with the exception of precise mass degeneracy, have no effect on the effective cross section. Because the coannihilation cross section for KK dark matter is either less than the one without coannihilation or the difference between the two is insignificant, $\langle\sigma v\rangle_{ds}$ is anticipated to always be greater or equivalent to $\langle\sigma v\rangle_{fo}$ [46].

The above-mentioned scenario has two exceptions: resonant annihilation with level-2 KK particles and coannihilation with the KK gluon[46]. The discussion for so is over the expertise of the present work. But to conclude, if $\langle\sigma v\rangle_{fo} = 3 \times 10^{-26} cm^3 s^{-1}$ is imposed in order to explain the observed relic density, the condition for the dark star formation is always satisfied[46]. Therefore, the authors of [46] concluded that KK dark matter that explains the observed relic density can always form dark stars.

3.2.3 Leptophilic Models

Leptophilic dark matter models have grown in popularity as a means of explaining the excess in PAMELA positrons, the excess in Fermi-LAT electrons, and the perfect agreement between the observed antiproton spectrum and the corresponding standard expectation[46]. To account for the excesses, the mass of dark matter is limited to be greater than $100GeV$. If the electron Fermi-LAT measurements are used, the mass constraint can be written as $m > 400GeV$.In this model, the dark matter particles annihilate exclusively to either of only one type of charged leptons(electrons, taus or muons), or democratically to all the three families [46].

In the figure 3.7(credit:[46]), it is assumed that the $\langle\sigma v\rangle$ does not depend on the temperature, in order to directly compare constraints relative to different epochs. The thick and thin solid line closed contours show the range of the values which is compatible with the PAMELA positron excess[48] and the Fermi-LAT $e^+ - e^-$ data[49] respectively. The two solid open lines represent conservative 2σ C.L. upper bounds for $f_Q \langle\sigma v\rangle_{ds} / m_\chi$ obtained from the flux of $e^+ - e^-$ observed by FERMI,

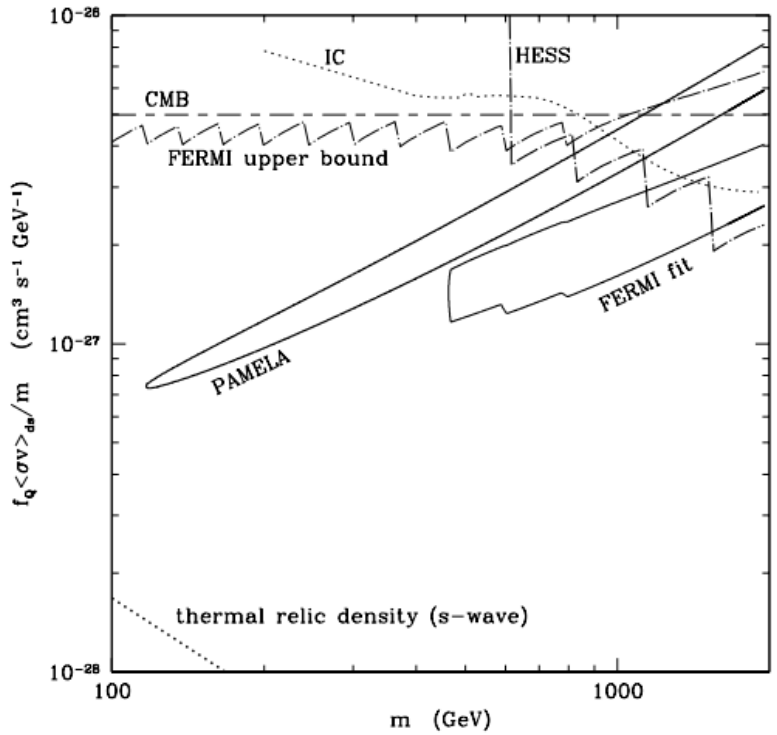

FIGURE 3.7: As a function of mass m, $f_Q \langle\sigma v\rangle_{ds} / m$ for a DM candidate annihilating to charged leptons of the three families, assuming that $\langle\sigma v\rangle$ is temperature independent. The thick solid line contour shows the range of values compatible with the PAMELA positron excess[48];the thin solid contour is the range compatible with the observed $e^+ + e^-$ flux measured by FERMI-LAT[49]; the thin solid line is the 2σ upper bound from the observed $e^+ + e^-$ flux of FERMI; the thick solid open line is the 2σ upper bound from the $e^+ + e^-$ HESS measurement[50]; the dot–dashed line represents the upper bound on $\langle\sigma v\rangle$ from the CMB[51][52][53]. The dotted line shows the upper bound on $\langle\sigma v\rangle$ obtained by comparing the expected gamma-ray flux produced by Inverse Compton(IC) scattering of the final state leptons to be FERMI-LAT measurement of the diffuse gamma ray emission with subtraction of the expected standard background[54]. Credit: [46]

represented by thin line, and the $e^+ - e^-$ flux observed by HESS[50], represented by the thick line. The dotted line represents the upper bounds on $f_Q \langle\sigma v\rangle_{ds} / m_\chi$.This is determined when the anticipated gamma ray flux which is caused by Inverse Compton scattering (IC) scattering of the final state leptons is compared to the diffuse flux of the gamma rays measured by the FERMI at intermediate Galactic latitudes. The long and short dashed line shows the upper bound on $f_Q \langle\sigma v\rangle_{ds} / m_\chi$ obtained by considering the imprint on the Cosmic Microwave Background (CMB)[51][52][53] from the injection of charged leptons from dark matter annihilations at the recombination epoch.

It is seen in the plot that the values of the combination $f_Q \langle\sigma v\rangle_{ds} / m_\chi$ are compatible with to the dark star formation when $\langle\sigma v\rangle_{ds} = \langle\sigma v\rangle_{gal}$, with range $m \gtrsim 1TeV$ is disfavored. Large annihilation cross sections $10^{-25} \sim \langle\sigma v\rangle_{gal} \sim 10^{-23}$ at the velocity $v_{gal} \simeq 300km/s$ of dark matter particles in our galaxy are required to explain

the PAMELA and Fermi-LAT excess. These values are up to two orders of magnitude bigger than $\langle\sigma v\rangle_{gal} = \langle\sigma v\rangle_{fo}$, which is consistent with a conventional thermal relic abundance in agreement with observations. Leptophilic models suggest another possibility for the production of dark stars: a significant annihilation cross section over the Universe's history and/or at the low temperatures at which dark stars form. Assuming $\langle\sigma v\rangle_{ds} = \langle\sigma v\rangle_{gal}$ this implies that $7 \times 10^{-28} cm^3 s^{-1} GeV^{-1} <\sim f_Q \langle\sigma v\rangle_{ds} / m_\chi \gtrsim 8 \times 10^{-27} cm^3 s^{-1} GeV^{-1}$). From the figure it can be seen that the condition given by equation 3.24 is easily verified and leptophilic models also satisfy the condition to form dark stars [46].

3.2.4 Neutrinophilic Model

Neutrinophilic dark matter is the model that annihilates exclusively into neutrinos. If only neutrinos are being produced in the annihilation, then the neutriniphilic dark matter would not be able to sustain the dark star as the neutrinos escape the gas without depositing any energy to the gas. The Z and W bosons, on the other hand, are projected to be created by the final state neutrinos' bremsstrahlung radiation. If we assume that the annihilation cross section of neutrinophilic dark matter in the dark star is equal to the cross section that produces a thermal relic density, i.e. $\langle\sigma v\rangle_{ds} = 3 \times 10^{-26} cm^3 s^{-1}$, if bremsstrahlung radiation is ignored, the branching ratio to $\nu\bar{\nu}$ is 1. When $2m > m_W$ or m_Z, the bremsstrahlung process, which can be considered as a three-body decay followed by the decay of the W or Z gauge bosons, is dominated by on-shell generation of W-bosons or Z-bosons. As a result, the apparent energy fraction of the W- and Z- boson decays is of order 1[46]. Therefore,

$$f_Q \sim \frac{g^2}{16\pi^2}\frac{E_W}{2m} > \frac{g^2}{16\pi^2}\frac{m_W}{2m} \tag{3.36}$$

where E_W is the W-boson's energy. In this situation, the criteria for the formation of a dark star may always be checked mathematically. However, when the value is $2m < m_W$, off-shell bremsstrahlung occurs. In the case of $2m << m_W$, it may be considered as a four-body decay in the limit of a 4-Fermi interaction. From the work of [46], it can be concluded that a dark star can be formed if the mass of the neutrinophilic dark matter is larger than $\sim 50GeV$[46].

Internal bremsstrahlung of charged particles, however, was not taken into account in their research, and lower the mass limit for the generation of dark stars to less than $50GeV$, depending on the particle physics model used. Neutrinophilic dark matter serves as a limiting scenario, demonstrating that any thermal dark matter candidate heavier than $m \gtrsim 50GeV$ may lead to the formation of dark star as long as $\langle\sigma v\rangle_{ds} = \langle\sigma v\rangle_{fo}$[46].

3.2.5 Summarising section 3.2

In this section, the work of [46] have been discussed. The authors of [46] concluded that the most popular examples of thermal dark matter candidates, i.e. "the neutralino in the MSSM; leptophilic models that might explain recent observations in the cosmic rays; the KK-photon and the KK-neutrino in UED models and a conservative neutrinophilic model where the dark matter particles annihilates exclusively to neutrinos, lead to the formation of dark stars". Few exceptions like: "heavy neutralinos in the presence of coaanihilation; annihilations that are resonant at dark matter freeze-out but not in dark stars; neutrinophilic dark matter lighter than about $50GeV$".

The authors of [46] further concluded that the discussion of neutrinophilic dark matter scenario allows us to conclude that a thermal dark matter candidate always forms a dark star as long as its mass is heavier than $\simeq 50GeV$ and the thermal average of its annihilation cross section is same at the decoupling temperature and during dark star formation, for example in the case of a cross section with a non-vanishing s-wave contribution. The formation of dark stars as first generation star is almost inevitable if the mechanism of [1] works and thermal dark matter when a standard thermal history of the Universe is assumed.

3.3 Energy Sources of Dark Stars

So far we have discussed the important criteria that are important for the formation of dark stars. In this section we will discuss the sources of energy that keep the star shinning. The possible energy contribution for dark star are[2]

$$L_{tot} = L_{DM} + L_{grav} + L_{nuc} + L_{cap} \tag{3.37}$$

The total luminosity or energy contributors are annihilation of adiabatically contracted dark matter, gravitational contraction, nuclear fusion, and annihilation by captured dark matter.

The energy released by the dark matter annihilation in course of adiabatic contraction dominates all other heating/cooling processes since the birth of the dark star until the dark matter runs out. The luminosity of the dark star by dark matter annihilation is given as[2]

$$L_{DM} = \frac{2}{3}\frac{1}{m_\chi}\int \rho(r)^2_{DM}\,\langle\sigma v\rangle\, dV \tag{3.38}$$

where m_χ,ρ_{DM}, and $\langle\sigma v\rangle$ are the mass, ambient density inside the star calculated via adiabatic contraction, and annihilation cross section of dark matter. The density of the dark matter depletes unless the loss cone is refilled.

When the dark matter fuel is exhausted, the star contracts in order to sustain pressure support, and the dark star era comes to an end. The contribution L_{grav} from gravitational energy release momentarily powers to the star. The star then compresses further, increasing density and temperature to the point where nuclear fusion occurs L_{nuc}[2].

The stellar densities get large enough to efficiently capture Dark Matter as the star collapses and moves into the fusion fueled main sequence. The collected dark matter annihilates, slowing the collapse and, for a short period, powering the star. WIMPs from the halo orbit the star, scattering off hydrogen and helium and lose enough energy to get entangled with it. The captured dark matter forms a Boltzmann distribution ρ_{cap} inside of the star. The captured dark matter annihilation rate will equal the capture rate with[2]

$$L_{cap} = 2m_\chi\Gamma_{cap} = 2f_Q\int \rho^2_{cap}\,\langle\sigma v\rangle\,/m_\chi dV \tag{3.39}$$

where $f_Q = 2/3$. The factor 2 comes from the fact that the energy released each annihilation is twice the mass of the WIMP. Dark stars fueled by captured dark matter are significantly hotter and denser than those powered by gravitationally captured dark matter due to their more compact form [2]. Chapter 4 discusses the capture of dark matter by star as energy source in detail.

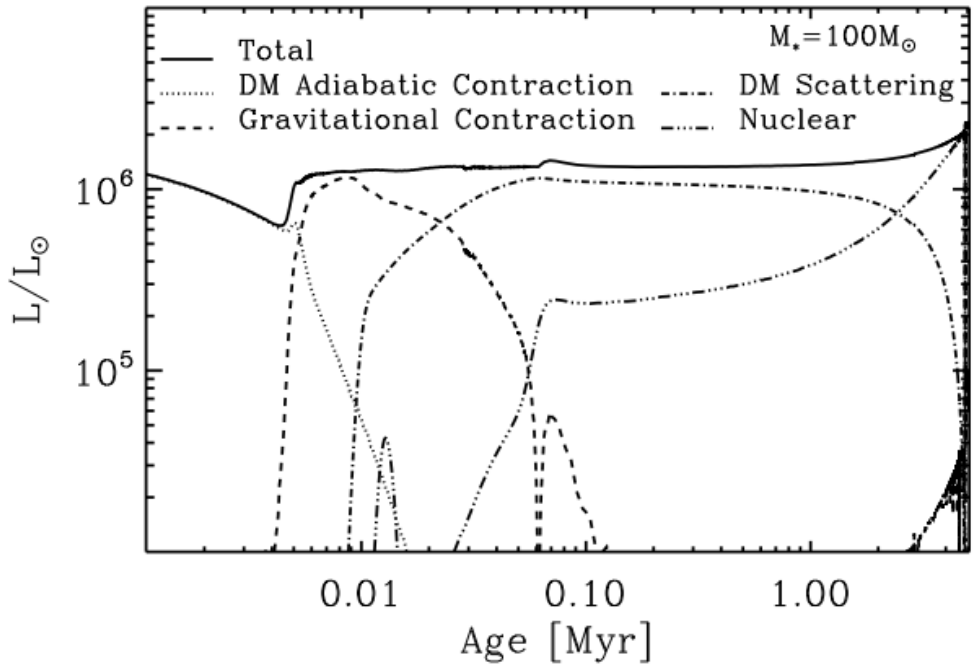

FIGURE 3.8: The total luminosity of a $100M_{\odot}$ star vs its age. The different curves show the inputs from adiabatic contracted dark matter annihilation (dotted line), gravitational contraction (short dashed line), scattered captured dark matter annihilation (dot–dashed line), and nuclear reactions (dot-dot-dot–dashed line). Credit: [55]

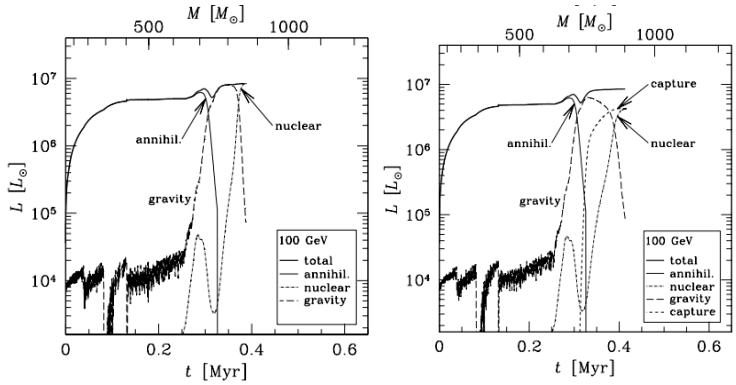

FIGURE 3.9: Luminosity evolution for the 100 GeV case as a function of time (lower scale) and stellar mass (upper scale). The total luminosity is represented by the solid (red) top curve. The bottom curves show the fractional contributions of various energy sources powering the star, (a) without capture (left frame) and (b) with "minimum" capture (right frame). In both frames, DM annihilation dominates total brightness at first (until around 0.3 Myr after the simulation begins, the total and annihilation curves are identical);eventually gravity takes over, and nuclear fusion follows. Capture becomes vital at the proper frame at the right moment. Credit:[56]

Figure 3.8 shows a total luminosity of a $100M_{\odot}$ star as a function of its age. This

is a evolution simulation of the work [55]. The dotted line show the energy input from adiabatically contracted dark matter annihilation, short dashed curve show contribution for gravitational contraction. Nuclear fusion contribution is shown via dot-dot-dot-dashed curve and scattering capture dark matter annihilation via dot-dashed curve. It can be seen clearly that the dominant contributor to the total luminosity of the star is dark matter annihilation during its early ages. Again, when the star is able to collect dark matter via scattering capture, the dark matter annihilation again dominates over other energy sources.

Figure 3.9 depicts the work of [56]. The figure depicts the evolution of dark star luminosity as a function of time for the case of $100GeV$ WIMP mass at the bottom scale and stellar mass at the top scale. The dark stars' interiors were assumed to be polytropic in order to get these results. The overall luminosity is shown by the top solid curve. The bottom curves indicate the partial contributions of various energy sources supplying energy to the star, a) without capture (left plot) and b) with 'minimal' capture (right plot). Dark Matter annihilation dominates the total luminance in both panels at first. The total and annihilation trajectories are indistinguishable until around 0.3 Myr after the start of the simulation of [56]'s work.After then, gravity takes over, followed by nuclear fusion. At the correct point in the story, capture becomes crucial.

Chapter 4

Capture of Dark Matter by the Stars

Capture of dark matter becomes important once the dark star is already large i.e. hundreds of solar masses, and only with the additional particle physics ingredient of a significant WIMP-nucleon elastic scattering cross section at or near the current experimental bounds [57].

WIMPs can scatter off the nuclei in a star with the scattering cross section σ_c as they move through it. The majority of these WIMPs pass directly through the star, but some lose enough energy to be caught. It is denoted by the capture rate $C(s^{-1})$. The WIMPs subsequently sink to the star's core, where they can annihilate one another at the annihilation rate $\Gamma_A(s^{-1})$.

The number of WIMPs N in the star is determined by difference between capture rate and annihilation rate given by equation[57]

$$\dot{N} = C - 2\Gamma_A \equiv C - C_A N^2 \tag{4.1}$$

The factor 2 represents the fact that two particles are annihilated in each events and therefore,

$$C_A = 2\Gamma_A / N^2 \tag{4.2}$$

is the defined as an N-independent annihilation coefficient. On solving this equation we get

$$\Gamma_A = 1/2C \tanh^2(t/\tau); \tau = (CC_A)^{-1/2} \tag{4.3}$$

Here τ is the equilibrium timescale. Equilibrium corresponds to a balance between the capture and annihilation rate i.e.

$$\Gamma_A = \frac{1}{2}C. \tag{4.4}$$

The annihilation rate

$$\Gamma_A = \int n_\chi^2(r) \langle \sigma v \rangle_{ann} \, d^3r \tag{4.5}$$

where $n_\chi(r)$ is the density of captured dark matter at point r inside of the star. The amount of energy ΔE lost by a WIMP in a scattering event with a proton (since it is assumed that the star is a POPIII star and it mostly consists of hydrogen) of mass M_P in the star ranges from

$$0 \leq \frac{\Delta E}{E} \leq \frac{m_\chi M_P}{[(m_\chi + M_P)/2]^2} \tag{4.6}$$

The average energy loss is $2M_P/m_\chi$ if we assume a flat distribution and take $M_P <<$

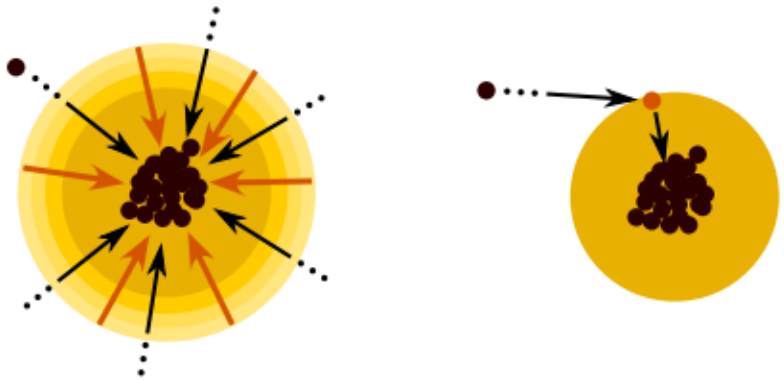

FIGURE 4.1: The two basic methods by which dark stars collect dark matter are shown. Gravitational contraction, seen on the left, happens when the baryonic collapse of a star-forming gas cloud increases the gravitational potential, attracting dark matter along with the baryons. Nuclear scattering, seen on the right, is based on weak scattering events between WIMPs and nucleons, during which the dark matter particles lose energy and be gravitationally bounded to the star. Credit: [58]

m_χ. Thermalization requires $\Delta E/E \sim 1$ i.e. there must be $m_\chi/2M_P$ scatters. Thus, for $m_\chi >> 1GeV$, the timescale for thermalization can be estimated as

$$\tau_{th} \approx \frac{1}{\sigma_c v_{esc} n_H} \frac{m_\chi}{2M_H} \tag{4.7}$$

where v_{esc} is the escape velocity of a dark matter particle from the surface of the star and n_H is the average density of the star. For example for a $100GeV$ WIMP, $\sigma_c = 10^{-39} cm^{-2}$ and $n_H = 10^{24} cm^{-3}$, the thermalization is calculated to be 3 months[57].

Using an isothermal distribution for dark matter,

$$n_\chi(r) = n_c e^{-m_\chi \phi/\kappa T} \tag{4.8}$$

where n_c is the central number density of dark matter and T is the central temperature of the star and $\phi(r)$ is the gravitational potential at radius r with respect to the center written as

$$\phi(r) = \int_0^r \frac{GM(r)}{r} dr \tag{4.9}$$

where $M(r)$ is the mass interior to radius r, one can define effective volumes as

$$V_j = 4\pi \int_0^{R_*} r^2 e^{-jm_\chi \phi/T} dr \tag{4.10}$$

which on integrating gives

$$V_j = [\frac{3m_{pl}^2 T}{2jm_\chi \rho_c}]^{3/2} \tag{4.11}$$

Here m_{pl} is the Planck mass and ρ_c is the core mass density of the star. The term effective volume is suggestive since we have $N = n_o V_1$ and total annihilation rate is given as

$$\Gamma = \langle \sigma v \rangle_{ann} n_o^2 V_2 \tag{4.12}$$

One can solve equation equation 4.1 to find the N-independent annihilation coefficient defined in equation 4.2,

$$C_A = \langle \sigma v \rangle_{ann} \frac{V_2}{V_1^2} \tag{4.13}$$

WIMP interacts with nuclei via two kinds: i)spin-independent, which scales as A^2, where A is the number of nucleons in the nucleus, and ii)spin-dependent, which requires the nucleon to have spin.

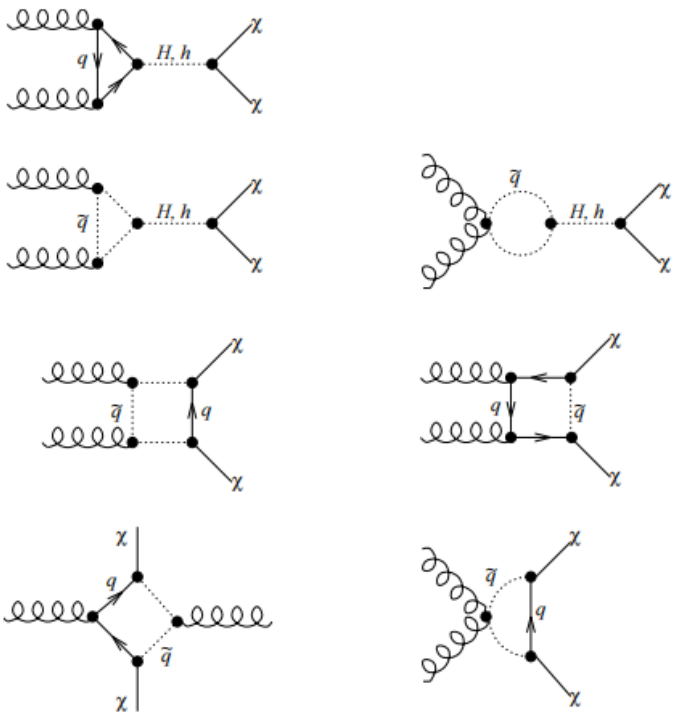

FIGURE 4.2: Feynman diagrams for neutralino-gluon scalar (spin-independent) elastic scattering.Credit:[24][25]

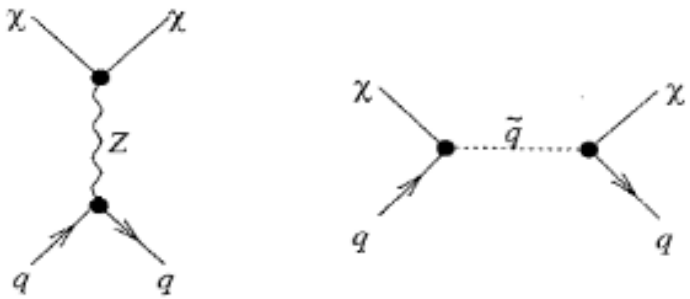

FIGURE 4.3: Tree level Feynman diagrams for neutralino-quark axial-vector (spin dependent) elastic scattering. Credit:[24][25]

The capture rate per unit volume at distance r from the center of the star for an observer at rest with respect to the WIMP distribution is[57]

$$\frac{dC}{dV}(r) = \sqrt{\frac{6}{\pi}} n(r) n_\chi(r) (\sigma_c \bar{v}) \frac{v^2(r)}{\bar{v}^2} \left[1 - \frac{1 - exp(-B^2)}{B^2} \right] \tag{4.14}$$

where n is the number density of nucleons, here hydrogen, n_χ is the WIMP number density, $v(r)$ is the escape velocity of WIMPs from the star at a given radius r, $\bar{v}^2 \equiv \frac{3\kappa T_\chi}{M}$ is velocity dispersion of WIMPs in the dark matter halo. Furthermore;

$$B^2 \equiv \frac{3}{2} \frac{v^2(r)}{\bar{v}^2} \frac{\mu}{\mu_-^2} \tag{4.15}$$

where $\mu = \frac{m_\chi}{M_N}$ is the ratio of WIMP to nucleon mass and $\mu_- = (\mu + 1)/2$. For an observer moving with respect to the WIMPs, the quantity in the square bracket in the equation 4.14 becomes more complicated function of B.

The capture rate for the entire star is then given as

$$C = \int_0^{R_*} 4\pi r^2 dr \frac{dC}{dV}(r) \tag{4.16}$$

where R_* is the radius of the star. To get a conservative and fairly accurate estimate of the capture rate, one may take

$$v^2(r) = v^2(R_*) = \frac{2GM_*}{R_*} \equiv v_{esc}^2 \tag{4.17}$$

for all r, assume the term in square brackets in equation 4.14 is very close 1 because the hydrogen has spin and helium generally does not. The spin-independent contribution of hydrogen and helium scattering in stars could be considered. This has not been done because the authors of [57] believed that this contribution to be subdominant. Taking a uniform dark matter density, the integration of equation 4.16 simplifies to give

$$C = \sqrt{\frac{6}{\pi}} \left(\frac{M_*}{m_p} f_H \right) (\sigma v) \left(\frac{v_{esc}}{\bar{v}} \right)^2 \frac{\rho_\chi}{m_\chi} \tag{4.18}$$

where M_* is the stellar mass, m_p is the mass of proton, and f_H is the fraction of hydrogen in the star.

To estimate $\bar{v}$ (as per [59]) virial velocity of dark matter halo is,

$$\langle \bar{v}^2 \rangle = \frac{|W|}{M_{halo}} \tag{4.19}$$

where

$$W = -4\pi G \int \rho_{halo} M_{halo}(r) dr \tag{4.20}$$

A typical dark matter halo containing a POPIII star has $M_{halo} = 10^5 - 10^6 M_\odot$. For ρ_{halo} NFW or Navarro, Frenk White profile[39] for the dark matter is assumed

$$\rho_{halo} = \frac{\rho_0}{\frac{r}{r_s} \left(1 + \frac{r}{r_s} \right)^2} \tag{4.21}$$

where r_s is the scale radius. The normalization ρ_0, known as the central density,

depends on the concentration parameter C_{vir} and on the redshift when the halo virializes Z_{vir}. These parameters range from $C_{vir} = (1-10)$ and $Z_{vir} = 10-50$. With $r_s = 15-100pc$, we find that $\bar{v} = 1-15km/s$ (authors of [57] took $\bar{v} = 10km/s$ as their fiducial value). For $B >> 1$, the square bracket term in equation 4.14 is very close to 1, which holds for all stellar and WIMP masses considered by the authors of [57](Refer to table 1 and table 2 of [57]). For example, for a solar mass star, one have $v_{esc} = 618km/s >> \bar{v} = 10km/sec$; then for $m_\chi = 100GeV$, $B \sim 100$. Thus one may ignore the square bracket term in the equation 4.14. However, when a star moves through the WIMP halo instead of being stationary, the phrase in the square bracket changes.

For using properties of POPIII stars assumed by authors of [60] and using the numbers $\rho_\chi = 10^9 GeV/cm^3, m_\chi = 100GeV and \sigma_c = 10^{-39}cm^2$ the capture rate scales as

$$C \propto \rho_\chi \sigma_c / m_\chi \tag{4.22}$$

For general values[57]:

$$C = 4.9\times10^{34}s^{-1}\left(\frac{M_*}{M_\odot}\right)\left(\frac{v_{esc}}{618km/s}\right)^2\left(\frac{\bar{v}}{10km/s}\right)^{-1}\left(\frac{\rho_\chi}{10^9GeV/cm}\right)\left(\frac{m_\chi}{100GeV}\right)^{-1}\left(\frac{\sigma_c}{10^{-39}cm^2}\right) \tag{4.23}$$

Further, using equation 4.17 and noting that for the POPIII models, it can be roughly stated that $R_* \propto M_*^{0.45}$, one can write[57]

$$C \approx 4.9\times10^{34}s^{-1}\left(\frac{M_*}{M_\odot}\right)^{1.55}\left(\frac{\bar{v}}{10km/s}\right)^{-1}\left(\frac{\rho_\chi}{10^9GeV/cm}\right)\left(\frac{m_\chi}{100GeV}\right)^{-1}\left(\frac{\sigma_c}{10^{-39}cm^2}\right) \tag{4.24}$$

4.1 Luminosity due to WIMP annihilation

The luminosity due to WIMP annihilation is [57]

$$L_{DM} = f_Q \Gamma_A (2m_\chi) \tag{4.25}$$

where factor 2 indicates that two WIMP particles need to find each other to annihilate and $f_Q = 2/3$ since neutrinos escape without depositing energy to the gas(1/3). The rest are electrons, positrons, and photons that are trapped in the star and hence their energy is thermalized.

Using equation equation 4.4 for $t >> \tau$ we have[57]

$$L_{DM} = \frac{f_Q}{2} C(2m_\chi) \tag{4.26}$$

From the simulation work of [57] one can write luminosity as

$$L_{DM} = 5.2\times10^{33}erg/s\left(\frac{M_*}{M_\odot}\right)^{1.55}\left(\frac{\rho_\chi}{10^9GeV/cm^3}\right)\left(\frac{\sigma_c}{10^{-39}cm^2}\right)\left(\frac{\bar{v}}{10km/s}\right)^{-1} \tag{4.27}$$

The luminosity depends linearly on the WIMP density passing through the stars. The density ρ_χ is the dark matter ambient density, which is the density in the ambient medium (NFW profile plus adiabatic contraction), but not the densities after capture. It is this density that specifies the annihilation rate, capture rate and therefore the luminosity of dark star. For any density higher than this value the star's

luminosity is, rather than conventional fusion, is dominated by WIMP annihilation energy. Also it can be noted that $L_{DM} \propto M_*^{1.55}$ whereas for a zero-metalicity star $L_* \propto M_*^2$

The Eddington luminosity is defined as

$$L_{Edd} = \frac{4\pi c G M_*}{\kappa_p} \tag{4.28}$$

where G is the Newton's constant, c is the speed of light, M_* is the mass of the star and κ_p is the opacity of the stellar atmosphere. Since the first stars' atmospheres are hot and nearly metal free, the opacity is dominate by the Thompson scattering, therefore[57],

$$L_{Edd} = 1.4 \times 10^{38} erg/s \left(\frac{M_*}{M_\odot}\right) = 3.5 \times 10^4 \left(\frac{M_*}{M_\odot}\right) L_\odot \tag{4.29}$$

Since Eddington luminosity scales as $L \propto M_*$, and the dark matter luminosity scales as $L \propto M_*^{1.55}$, for a large enough dark matter density the two curves will cross for some stellar mass. The lightest mass for which $L_{DM} > L_{Edd}$ is then an approximation of the top mass limit for the initial stars. The radiation pressure from the WIMP annihilation prevents the stars of that mass from accreting any more.

Assuming that the accretion efficiently boosts the mass of every POPIII star, the mass of the initial star will be governed only by dark matter characteristics. Therefore, using equation 4.27 and equation 4.28 one gets[57]

$$M_*^{max} = 1.1 \times 10^8 M_\odot \left(\frac{\rho_\chi}{10^9 GeV/cm^3}\right)^{-1.8} \left(\frac{\sigma_c}{10^{-39} cm^2}\right)^{-1.8} \tag{4.30}$$

Chapter 5

Evolution of Dark Stars

A simple idea of the evolution of dark star has been introduced in the section3.3. Once the star exhaust its dark matter via annihilation which the star collected via adiabatic contraction, the star begins to contract which gives to the star energy contribution, paving the way for nuclear fusion phase of the star and the dark star phase terminates. If the star finds itself again surrounded by a high dense dark matter halo, the star then can capture dark matter whose annihilation surely does have an effect on the evolution of star.

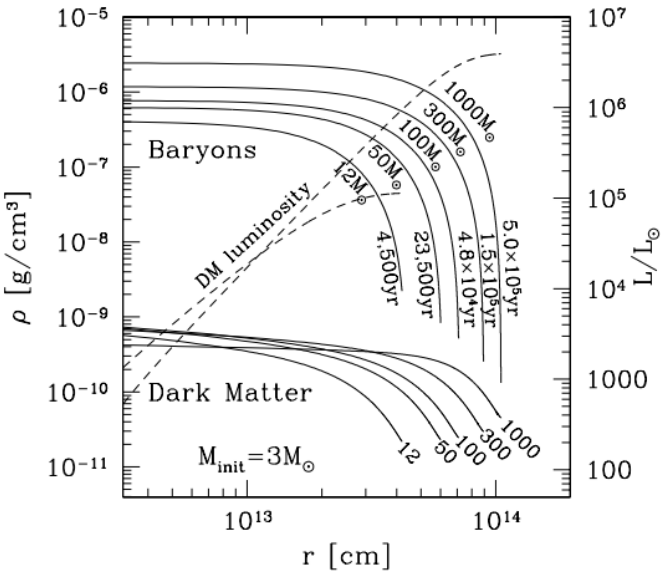

FIGURE 5.1: The evolution of a dark star is shown, as mass is accreted onto the initial protostellar core of $3M_\odot$. At different masses and times, the top solid curve represents the baryonic density profile, while the bottom solid curve depicts the dark matter density profile (values provided on left axis).The luminosity L_{DM} integrated out to radius r in solar units for masses 12 and $1000M_\odot$ is shown on the dashed lines, with values on the right axis.Credit:[61]

Figure 5.1 shows the stimulative work of [61]. The authors assumed that the dark stars can be described as polytropes in the hydrostatic equilibrium

$$P = K\rho^{1+\frac{1}{n}} \tag{5.1}$$

where P is the pressure, ρ is the density, and the constant K is determined once

the total mass and radius are specified [62]. Polytropes in the range $n = 1.5$ (totally convective) to $n = 3$ (pre-main-sequence stellar models) characterise pre-main-sequence stellar models (fully radiative). The authors repeat the radius of the model for a given mass to discover the point of thermal equilibrium, where the total dark matter heating equals the emitted luminosity. Then adding $1M_{\odot}$, a new equilibrium is calculated, and is continued up to $1000M_{\odot}$. In the standard scenario of the birth of the first stars, it was discovered that the mass of the protostellar cloud surpasses the Jeans mass at $n \sim 10^4 cm^{-3}$. This quantity of baryonic matter, $\sim 1000M\odot$, may fall upon a dark star, bringing in even more dark matter with it. The dark matter densities in the protostar are calculated using the method given in [1].(Refer [61] for details.)

The figure 5.1 (Credit: [61]) illustrates the results for standard parameters for $M_* = 10M_{\odot} - 1000M_{\odot}$ for $n = 1.5$. Figure 5.1 shows the plot of the baryon and dark matter density profiles. Dark matter density is several orders of magnitude smaller than baryon density during evolution, yet the star is fueled by dark matter annihilation. Dark matter is depleted in the interior regions of the star as a result of annihilation, and the density becomes nearly constant. In the figure 5.1, for $L_{DM}(r)$, the dark matter luminosity integrated out to radius r, displays that the heating is scattered over a vast fraction of the volume of the dark star, rendering it insensitive to changes in the adiabatic contraction model parameters. As the star reaches $1000M_{\odot}$, the total amount of dark matter left in the star is only one-third solar mass, and $1/3$ is annihilated away. L_* is generally an order of magnitude less than that of the Eddington luminosity of a star of that mass and radius for every evolutionary state. Dark star is fully convective for mass below $100M_{\odot}$. It starts to make transition from convective to radiative in the mass range $100 - 200M_{\odot}$, and then become fully radiative for $M_* > 200M_{\odot}$ but for a small convective region on the surface. For $M_* = 600M_{\odot}$, the $n = 3$ case gives surface temperature $T_{eff} = 9100K$; Photospheric radius $R_S = 6.0 \times 10^{13} cm$; Stellar luminosity $L_* = 4.6 \times 10^6 L_{\odot}$ and central temperature $T_c = 6.88 \times 10^5 K$. In the lack of dark matter, which radiates at $T_{eff} > 30,000K$, dark stars have significantly lower T_{eff} than ordinary metal free POPIII main-sequence stars. This difference is an observable signal for dark stars as opposed to ordinary POPIII stars.

The work of [63] formed a "base model" with mass of dark matter $100GeV$ and accretion rate $dM/dT = 1.0 \times G - rate M_{\odot} yrs^{-1}$, where $G - rate = 0.18 \times M^{-0.6} M_{\odot} yrs^{-1}$, where M is the mass of the star.This base model demonstrates dark star phase characteristics, such as how much dark matter annihilation energy expands the star, causing it to be in gravitational equilibrium. One of the dark star's peculiarities is its lower temperature. This stable stage lasts until the dark matter annihilation energy supply is inadequate to keep the structure stable. Finally, the star rapidly collapses and approaches the main-sequence phase. At this moment, the star's mass approaches $M \sim 900 - 1000M_{\odot}$, corroborating the work of [1]. Massive dark stars inevitably collapse gravitationally, becoming massive black holes with masses of up to $1000M_{\odot}$. The authors of [63] also find that all of the models they worked on went through the dark star phase, which was sustained by a little amount of dark matter fuel equal to less than 0.1% of the stellar mass. Figure 5.2 shows the HR-diagram made by the authors of [63], for various dark matter models and no dark matter model.

Figure 5.3[63] depicts the evolution of several stellar properties for various dark matter masses. For smaller dark matter particle masses, dark matter annihilation is greater, and the star expands more, lowering temperature and density. The time of dark star phase is similarly extended for lower dark matter masses, and the final

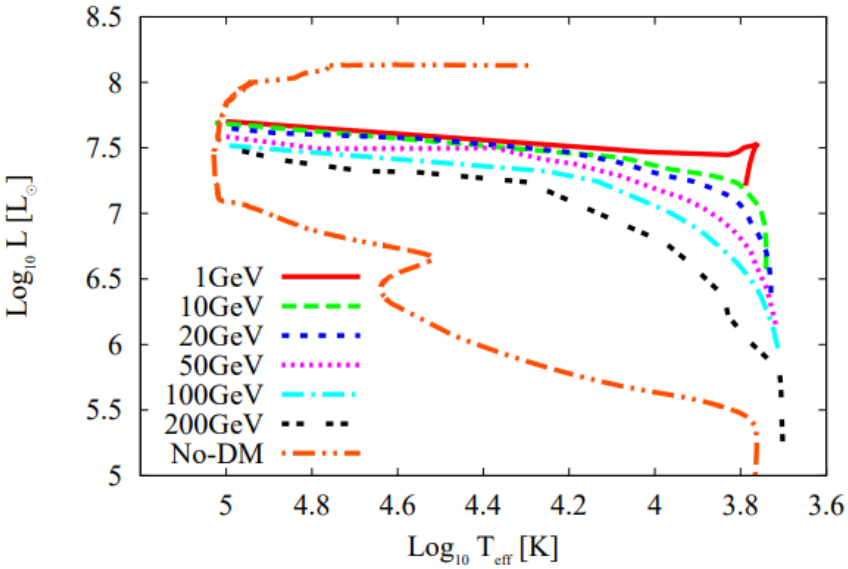

FIGURE 5.2: HR Diagram for dark stars with dark matter particle having various mass models. Each line represents a model with dark matter particle masses $m_\chi = 1, 10, 20, 50, 100, 200 GeV$ and the no-Dark Matter model. Credit:[63]

stellar mass is greater than the base model.

The work of [64] incorporates the the effects of WIMPs annihilation in the Geneva stellar evolution code[65], and followed the evolution of a $20 M_\odot$ and $200 M_\odot$ stars for different dark matter densities. The WIMPs here are fueled via scattering capture. In this work[64], the authors concluded that above a critical dark matter density, the annihilation of WIMPs captured by the POPIII stars can significantly alter the evolution of these objects and prolong their lifetime beyond the age of the Universe. For dark matter density higher than $10^9 GeV cm^{-3}$, in comparison to the standard scenario, the luminosity of nuclear fusion is overwhelmed by the WIMP annihilation luminosity produced at the star's core, causing the star to inflate and decrease the effective temperature, as well as a moderate decrease in star luminosity at the ZAMS (zero age main sequence) position. The nuclear processes are delayed, and therefore the core H-burning lifespan is extended, which is a significant divergence from the typical evolution. When the dark matter fuel runs out, the star returns to the ZAMS and continues to evolve. In comparison to typical stars of the same mass and metallicity, these "frozen stars" would seem significantly larger and have a much lower surface temperature.

Furthermore, [3][66] introduced a dark star evolution code which incorporates the scattering capture of dark matter, called "DarkStars"(detailed discussion in section 7.5). This code can be used to study evolution of dark stars.

Figure 5.4, credit: [67], shows the evolutionary tracks followed by the HR diagram by stars of various masses, when WIMPs provide different fractions of their total energy budgets. Filled, unlabelled circles indicate the starting points of tracks. The filled marked circles, on the other hand, show the age of $1.4 M_\odot$ dark star evolution stages. When the star runs out of hydrogen in its core or reaches the present age of the Universe, the tracks were stopped. Because of the energy intake from WIMP annihilation, the time required to burn core hydrogen is lengthened, resulting in a longer effective main-sequence lifetime, as seen in figure 5.5. The increase

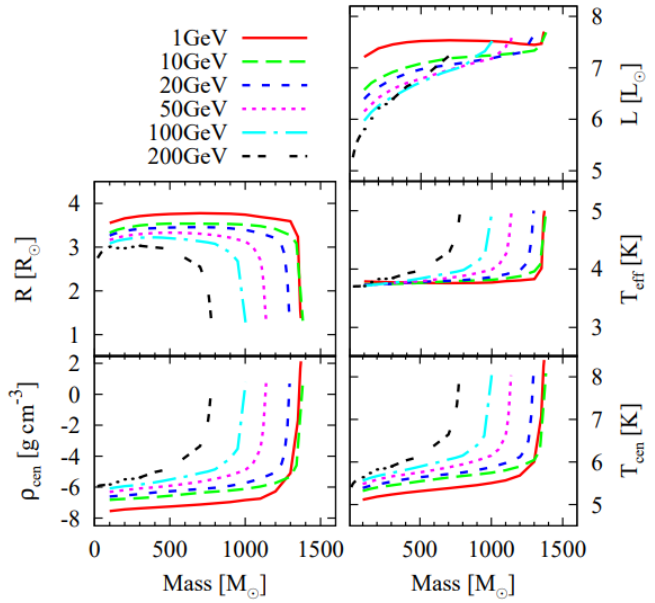

FIGURE 5.3: Evolution of different stellar values for dark star models using dark matter particle mass parameters. Logarithmic scale is used to plot all vertical axes.Credit:[63]

in main sequence lifespan is noticeable at all metallicities, but is most noticeable at low redshift. This is due to the fact that conventional main-sequence lifetimes are shorter at lower metallicities. In the extreme event of a very large WIMP luminosity, it is exceedingly unlikely that a star would have ever entered the main sequence at all, or that it would have simply stopped during its first descent of the Hayashi track. The lifetimes of stars with smaller masses and metallicities are more impacted by a particular WIMP-to-nuclear burning ratio than their more massive, metal-rich counterparts.

The authors of the work [55] have treated separately the mechanism of adiabatic contraction and scattering capture of dark matter and showed the effects on the pre-main sequence phase of stellar objects with masses $5M_{\odot} < M_{*} < 600M_{\odot}$(HR diagram of the work of[55] is shown in figure 5.6). They presented the following conclusions:

1. The luminosity produced by dark matter annihilation during the adiabatic contraction regime generates a temporary halting period early in the proto-stellar evolution. For typical durations varying from 2.1×10^3 years for $600M_{\odot}$ star to 1.8×10^4 years for $9M_{\odot}$ star, all proto-stellar objects become dark stars.

2. This halting time happens when the stars are on the Hayashi track. The adiabatic contraction moderates the effective temperature of the star by maintaining an equilibrium condition during the early evolutionary phases, which is characterized by large radii when the effective temperature is $\approx 5 \times 10^3 K$.

For fiducial set of parameters for scattering capture of dark matter ($\bar{v} = 10km/s, \rho = 10^{11} GeV/cm^3, \sigma_0 = 10^{-38} cm^2$), the following conclusions were presented by [55]:

1. The scattering capture luminosity is perhaps most effective for stars $M_{*} < 40M_{\odot}$, and on the HR diagram, just as they near ZAMS, their development is interrupted.

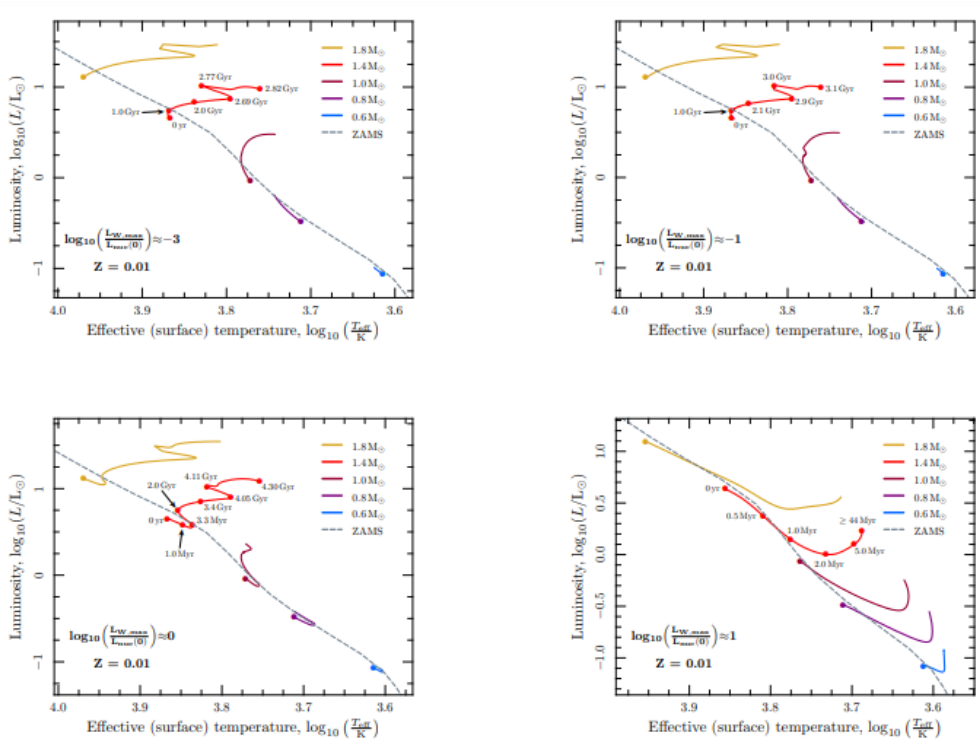

FIGURE 5.4: For WIMPS supplying different portions of their entire energy budget, evolutionary paths are followed in the HR diagram by stars of different masses. Credit:[67]

2. Dark Stars can sustain by scattering capture luminosity as long as the environmental circumstances do not change. Since, unlike adiabatic contraction, scattering capture luminosity is dependent on the flux of dark matter particles flowing through the star from outside. As a result of consuming from a reservoir that is nearly limitless, dark stars stay "frozen" on the HR diagram.

3. Stars with masses $\geq 40M_\odot$ are able to begin nuclear reactions and go through the main sequence with the help of an extra energy source: Dark matter annihilation increases their lives by a factor of 2 for a $600M_\odot$ star and by a factor of 5 for a $40M_\odot$ star.

Finally, the following concluding remarks of the simulation work of [68] for the properties of dark stars are as follows:

- The fundamental properties of the dark stars are not sensitive to the exact treatment of the fraction of the energy injected per WIMP annihilation, f_Q, into the surface of the star. This shows that the largest fraction of the energy is produced in the core where the dark matter and baryonic densities are highest.

- The growth of dark stars up to $\sim 1000M_\odot$ is not limited by the dynamical instabilities. A star is dynamically unstable, if it collapses upon a small, initial compression. This is the case if the weight and increase arising from the compression is larger than the increase in the pressure.

- Dark stars of $10 - 1000M_\odot$ are not subject to mass loss driven by the super-Eddington winds. The Eddington limit refers to a condition in the star where the outward acceleration due to radiation pressure balances the inward force

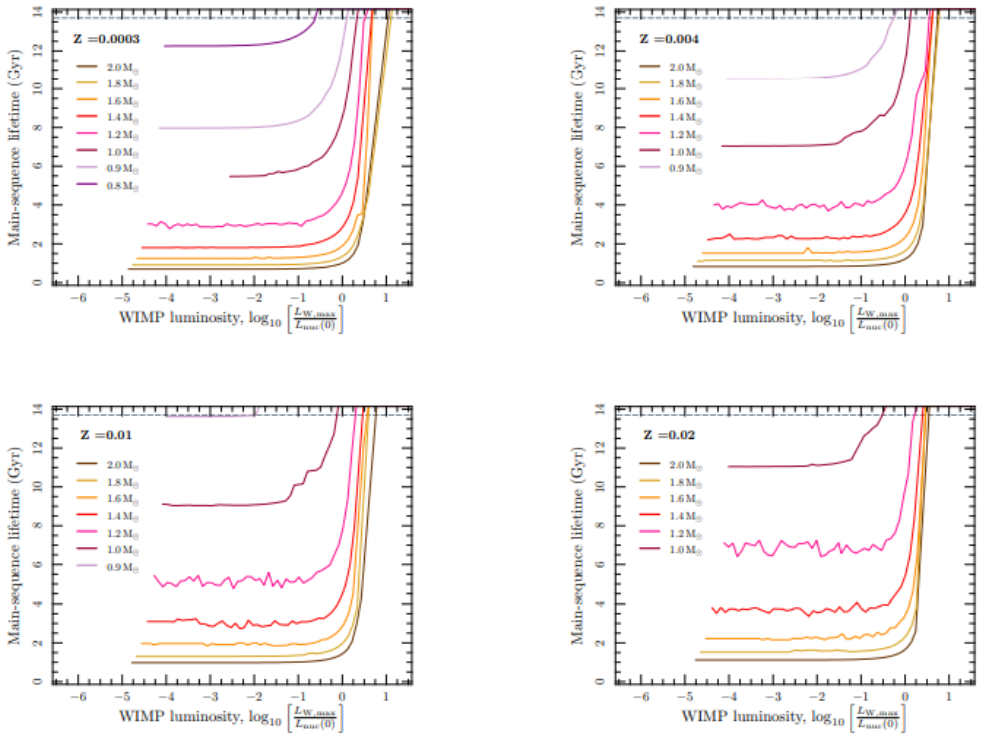

FIGURE 5.5: Stars with varying masses, metallicities, and WIMP luminosities have different main-sequence lifetimes which is shown in this figure. The dotted lines represent the Universe's current age. Stars that get a larger portion of their energy from WIMPs burn hydrogen more slowly and spend longer time on the main sequence. Credit:[67]

due to gravity in hydrostatic equilibrium. If this limit is surpassed at the surface, it is believed that mass outflows should arise.

- Dark stars with masses $\lesssim 200 M_{\odot}$ can pulsate with periods of $\sim 60 - 600$ days in their rest frame.
- The growth of dark stars with pulsations is not affected by mass outflows arising from the excited radial pulsation modes. Even under conservative assumptions, the mass loss rate stays at least one order of magnitude below the accretion rate.

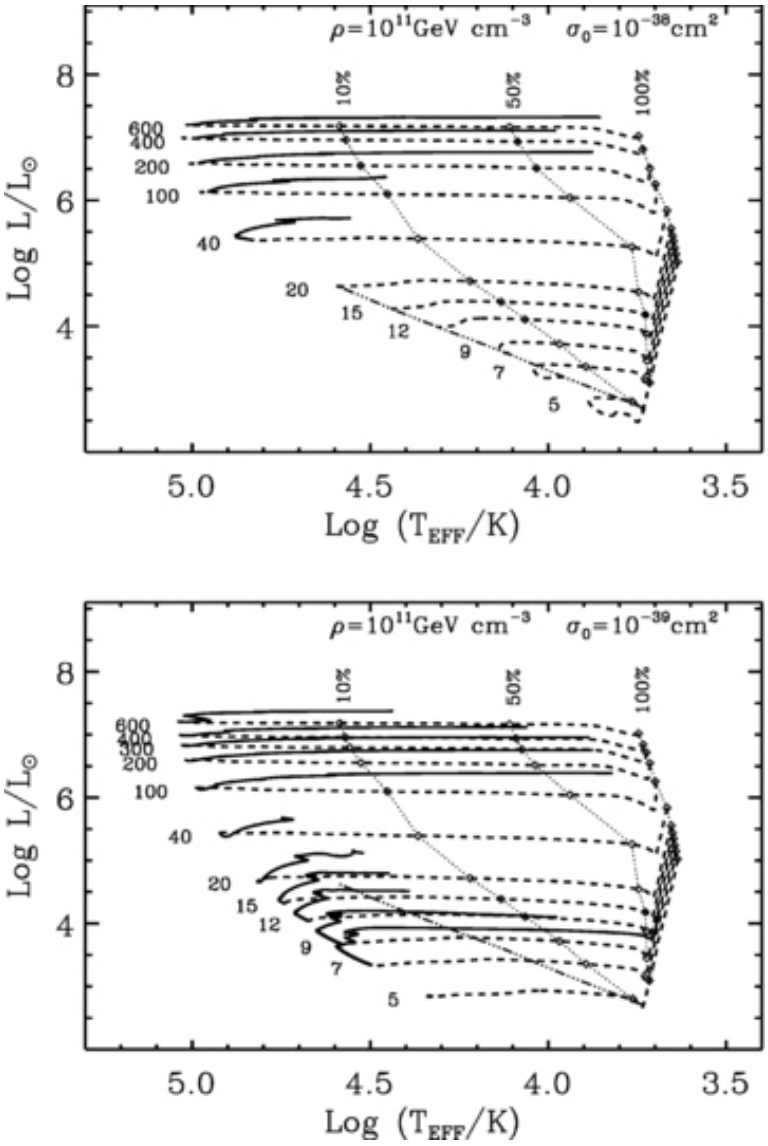

FIGURE 5.6: For a grid of star masses, the HR diagram is shown. The dashed line represents the pre-Main Sequence phase while the solid line represents the Main Sequence phase for each star model. Dotted diagonal lines show the evolutionary stages when $L_{AC}/L_* = 1, 0.5 and 0.1$. The dot–dashed line illustrate the locus of the 'freezing' points, when the evolution is halted by SC DM annihilation luminosity before the ZAMS. The results in the upper panel were obtained using fiducial DM parameters $\sigma 0 = 10^{-38} cm^2$ and $\rho = 10^{11} GeV cm^{-3}$. The tiny loops in the $5M_\odot$ and $7M_\odot$ models are caused by WIMP thermalization, which leads in an effective delay of the effects of SC DM annihilation luminosity. The stellar models in the lower panel were conducted with the same DM density but $\sigma_0 = 10^{-39} cm^2$. Credit:[55]

Chapter 6

Observations of High Red-shifted Dark Stars

In this chapter we will discuss the possible ways in observing Dark Stars. This chapter is divided into three sections. The first section discusses the expected spectral energy distribution of the dark stars for a supermassive dark stars (SDMS) and stars with mass $< 10^6 M_\odot$. The second section will discuss the direct detection of dark stars i.e. how James Webb Space Telescope or JWST, which has been launched successfully on December 25^{th} 2021, be able to observe these stars. Furthermore, we will also look into whether the Hubble Space Telescope (HST) can observe these stars.

The third section will discuss the indirect ways through which we can detect dark stars. Since the dark stars are theorised to be the first stars, they should have some signatures in the Cosmic Microwave Background and reionization.

The James Webb Space Telescope is an international collaboration between NASA, the European Space Agency (ESA), and Canadian Space Agency (CSA). It is a large infrared telescope with an approximately 6.5 meter primary mirror. It is capable to study every phase of the history of the Universe, ranging from first luminous glows after the Big Bang, to formation of solar systems[69].

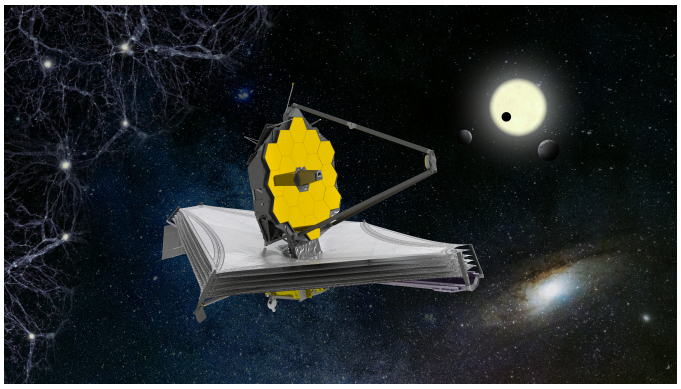

FIGURE 6.1: Artistic impression of the James Webb Space Telescope. Credit: https://www.esa.int/ESA_Multimedia/Images/2021/03/Artist_s_impression_of_the_James_Webb_Space_Telescope

6.1 Spectral energy distribution of Dark Stars

The work of [70] and [71] provided a synthetic stellar atmosphere spectra for dark stars. Figure 6.2 shows spectral energy distribution of Supermassive dark stars, with mass of $10^6 M_\odot$[70]. Because dark stars are largely formed of primordial hydrogen and helium (if they are born in early Universe), and other elements are thought

to be non-existent in the stellar atmosphere, all spectral lines found are those of hydrogen and helium. In the figure 6.2, the left panel shows the spectral distribution of a $10^6 M_\odot$ formed via adiabatic contraction and the right panel shows the spectral distribution of dark stars formed via capture of dark matter.

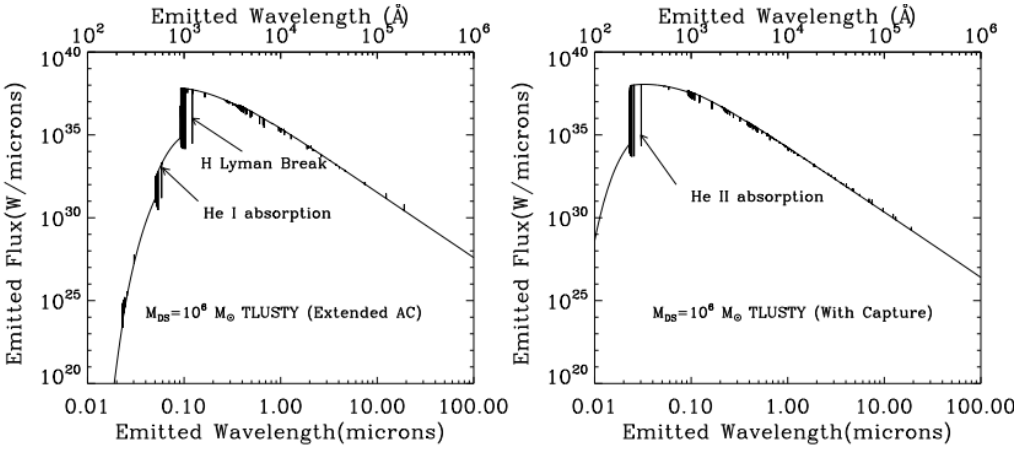

FIGURE 6.2: Anticipated SEDs of a $10^6 M_\odot$ SMDS. Left-hand panel: Dark Star created by the extended AC only mechanism with a surface temperature of $1.9 \times 10^4 K$. Right-hand panel: Dark star born using 'with capture' with surface temperature of $5.1 \times 10^4 K$. Credit:[70]

The left panel of figure 6.2 (Credit: [70]) shows the expected spectral energy distribution of a SMDS of mass $10^6 M_\odot$ with effective temperature $T_{eff} = 1.9 \times 10^4 K$ which grew via extended adiabatic contraction. The Lyman edge is visible at roughly 0.1 microns. Photons have often been shifted to higher wavelengths (lower energy), which were below the Lyman edge when compared to a blackbody of the same temperature by absorption and rescattering. The excess visible at wavelengths slightly below the Lyman edge, on the other hand, is caused by photons emitted from deeper within the star. Because of the lower surface temperature, a considerable amount of neutral hydrogen and helium persist in the stellar atmosphere, leading to a strong absorption lines at Lyman series wavelengths ($0.1216\mu m - 0.0912\mu m$). Another break in the spectrum can be seen at shorter wavelengths owing to neutral helium HeI absorption ($\sim 0.05\mu m - 0.06\mu m$). HeI lines appear at wavelengths $\sim [0.3\mu m - 0.45\mu m]$, HeII lines at $\sim 0.46\mu m$, and more HeI lines at $\sim [0.47\mu m - 0.7\mu m]$.

The right panel of figure 6.2 shows the spectrum of a $10^6 M_\odot$ and $T_{eff} = 5.1 \times 10^4 K$ dark star which grew via captured dark matter. The most visible difference seen between right and left panels is a shift in the spectrum's peak to lower wavelengths and a sharper UV continuum slope. Regardless of the fact that SMDS produced by capture are hotter, their significantly smaller radius makes them harder to detect in the near - infrared region at redshifts of ~ 10 and higher. In the right panel, the higher the surface temperature, the more hydrogen is ionised, and hence the Lyman absorption lines are weak. The sequence break correspond to absorption by singly ionized HeII at wavelengths in the range from $0.023\mu m$ to $0.030\mu m$. The HeI lines also appear at wavelengths $\sim [0.3\mu m - 0.45\mu m]$, HeII lines at $\sim 0.46\mu m$, and more HeI lines at $\sim [0.47\mu m - 0.7\mu m]$, but weaker. In both cases(left and right panel) one can note a sequence of absorption lines between $\sim [0.8\mu m - 1.0\mu m]$, which correspond to HeI absorption.

Figure 6.3 shows synthetic stellar atmosphere spectra compared to blackbody spectra for dark stars, a work done by authors of [71]. To compute the expected

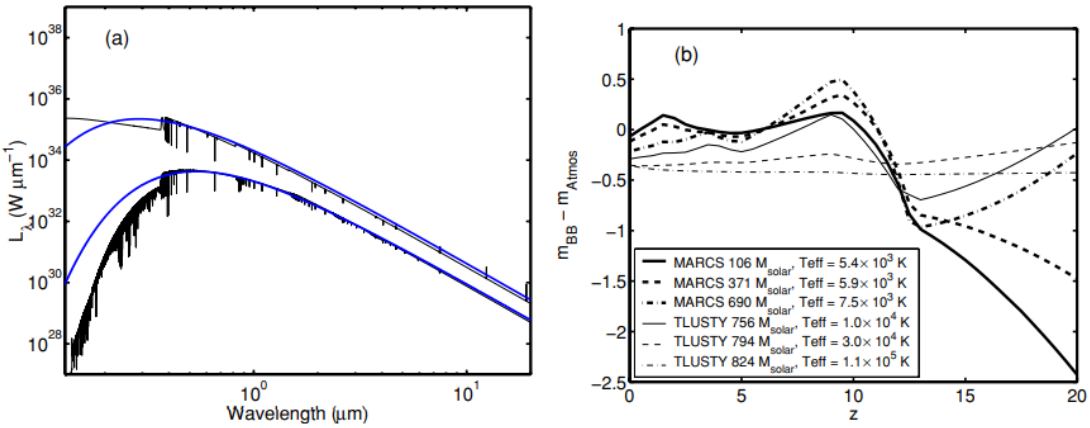

FIGURE 6.3: Synthetic stellar atmosphere spectra are compared to dark star black body spectra. SEDs of the $106M_{\odot}$ $T_{eff} = 5400K$ (lower SEDs) and $756M_{\odot}$ $T_{eff} = 10000K$ (upper SEDs, multiplied by 100 to prevent cluttering) dark stars predicted for a $1GeV$ WIMP. The black lines represent to synthetic stellar atmosphere SEDs created using MARCS (for lower $T_{eff} = 5400K$ spectra) and TLUSTY (for upper $T_{eff} = 10000K$ spectra), whereas the blue lines represent black body spectra made for identical temperatures and bolometric luminosities. Credit:[71]

spectral energy distributions of dark stars, the authors of [71] used the MARCS stellar atmosphere code [72] for $T_{eff} \leq 8000K$ objects and the TLUSTY code[73] for $T_{eff} \geq 10000K$. Because none of the codes is able to handle objects in the $T_{eff} \approx 8000 - 10000K$ range, whenever possible, the evolutionary tracks are interpolated to provide replacement points barely outside this temperature range. All models assume primordial H and He abundances. The MARCS atmospheres are assumed to have an overall metallicity of $Z = 2.5 \times 10^{-7}$, whereas the TULSTY atmospheres are assumed to have an overall metallicity of $Z = 0$.

The left panel of figure 6.3 (Credit:[71]) shows the SEDs of the $106M_{\odot}$, $T_{eff} = 5400K$(lower SEDs) and the $756M_{\odot}$, $T_{eff} = 10000K$ dark stars predicted for a $1GeV$ WIMP (upper SEDs multiplied by 100 to eliminate cluttering). The black lines correspond to synthetic stellar atmosphere SEDs created by MARCS for lower $T_{eff} = 5400K$ spectra and TLUSTY for higher $T_{eff} = 10000K$ spectra.The blue lines are black body spectra computed for identical temperatures and bolometric luminosities. The differences are the absence of breaks and absorption lines in the black body spectra. The most notable break is at $\approx 0.36\mu m$. Because of the MARCS spectrum's low but non-zero luminosity, $[Fe/H] = -5$, $106M_{\odot}$ and $T_{eff} = 5400K$ dark star, several metal lines may be detected in the lower SED below $0.36\mu m$.The right panel depicts the difference in black body AB magnitudes m_{BB} and synthetic stellar atmosphere AB magnitudes m_{Atmos} in the James Webb Space Telescope's NIRCam F444W filter. The various lines correspond to the six dark star models for $1GeV$ WIMP. There are discrepancies between m_{BB} and m_{Atmos} for colder dark stars, $\leq 10,000K$, but the differences for hotter dark stars are less than $0.5mag$. This is largely due to the fact that hotter stars become more blackbody-like at the appropriate wavelengths[71].

6.2 Direct detection using JWST and HST

In this section we will discuss the possibility of observing dark stars using the JWST and Hubble space telescope. This section is divided into two parts. The fist part will be dedicated towards observing dark stars of masses upto $10^3 M_\odot$ and discussion of the work of [71]. The second part will be dedicated towards the discussion of work [70], i.e. observation of supermassive dark stars with mass range $10^6 - 10^7 M_\odot$.

The projected lifetime of dark stars is critical in determining the detectability of them at high redshifts. In theory, these stars may exist endlessly as long as there is an abundance of dark matter to feed them. But since the stars use dark matter annihilation, which makes the dark matter deplete in the stellar core if it is not replenished, the fusion will take over and the star will transform into a conventional POPIII star. These stars, however, would be more massive since the longer duration of the formation phase enabled them to accrete more gas.

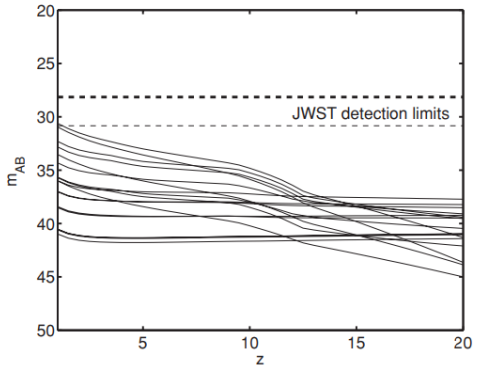

FIGURE 6.4: The estimated apparent AB magnitudes of dark stars in the NIRCam/F444W filter at $z = 1 - 20$. The horizontal dashed lines shows JWST detection limits for a 10σ point source detection after 10^4s of exposure (thick dashed) and a 5σ point source detection after 3.6×10^5s ($100h$) of exposure (thin dashed). The dark stars are $4 - 14$ magnitudes too weak to distinguish at $z = 10 - 20$. As a result, JWST will be unable to distinguish distinct population III dark stars at the redshifts at which they are created without the magnification boost given by a neighboring galaxy cluster. Long-lived dark stars ($z \approx 6$) that survive until the end of reionization seem slightly brighter, but are still at least 2 magnitudes underneath the detection limit. Credit:[71]

Figure 6.4, credit given to the authors of [71], shows the AB magnitudes of all dark star models, the authors of [71] worked on (Refer to table 1 in [71] for dark star models), as a function of redshift ($z = 1 - 20$) in the NIRCam F444W filter. The plot also shows two estimated JWST detection thresholds for point sources, which are represented by dashed horizontal lines. The thick dashed line is based on 10σ detection for 10^4s exposures, and the thin dashed line is based on 5σ detection after $100h$ or 3.6×10^5 s exposures. The former are the fiducial JWST detection limits, which can be seen on the JWST web page. (`http://www.jwst.nasa.gov/`).The latter, on the other hand, broadly match to the magnitude limitations anticipated for extremely deep field observations. The figure clearly shows that all of the dark star models are far below both of these detection limits at high redshifts. The intrinsic luminosities of dark stars transform to apparent magnitudes that are $4 - 14$ magnitudes too weak at redshifts $z = 10 - 20$. As a result, without the magnification boost provided by a nearby galaxy cluster, JWST will be unable to see individual POPIII dark stars at

the redshifts at which they are formed. Long-lived dark stars that survive until the end of reionization seem slightly brighter, but they are still at least two magnitudes below the detection limit[71].

In figure 6.5, the authors of [71] display AB magnitude for all dark matter models they worked on at redshift $z = 6$ and $z = 10$ as a function of central wavelengths of all broad JWST filters.The JWST detection limitations are also included, as shown in figure 6.4. All dark star models considered by the authors of [71] lie significantly faint of these thresholds, regardless of which filter is used, the authors of [71] concluded. A magnification of $\mu = 160$ owing to gravitational lensing by a foreground galaxy cluster, on the other hand, would shift all models upwards by ≈ 5.5 magnitudes, as indicated by the the upward arrow in the figure, and shift certain types of dark stars into the brightness regime observable by the NIRCam but not by MIRI[71].

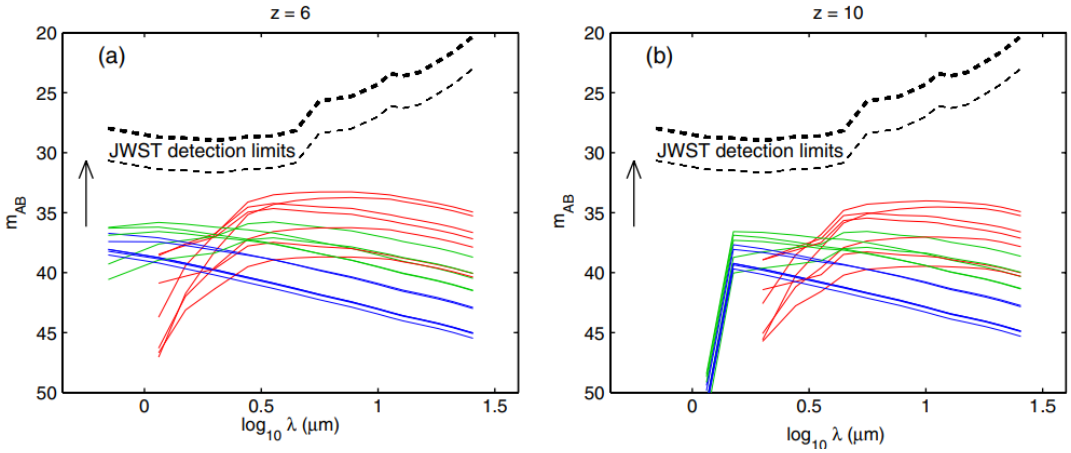

FIGURE 6.5: The predicted apparent AB magnitudes of dark stars at z=6 (a) and z=10 (b), as a function of the JWST broadband filters' center wavelength. Each solid line represents a different dark star model. Credit:[71]

Each solid line in the figure 6.5(credit:[71]) represents an individual dark star model, colour coded according to the effective temperature of the star. For $T_{eff} \leq 8000K$, they are represented by red, for $8000K < T_{eff} \leq 30000K$ by green and $T_{eff} > 30000K$ is represented by blue. As mentioned before, all dark star models are faint for the JWST to observe, but the gravitational lensing will help magnify the star and in this case for some of the $T_{eff} \leq 30000K$ dark stars (green and red lines) at both $z = 6$ and $z = 10$. The red lines end abruptly at $1.15\mu m$ or $log_{10}\lambda = 0.06$ for $z = 6$ and at $2.0\mu m$ or $log_{10}\lambda = 0.3$ for z=10 is that the short-wavelength limit of the MARCS model (refer to table 1 of [71]) spectra have entered the bluer filters at these redshift.At $z = 10$, the steep decline in brightness at $\lambda \leq 1.5\mu m(log_{10}\lambda \leq 0.17)$ along the blue (dot-dashed) and green (thick solid) lines is caused by HI absorption in the foreground intergalactic medium[71].

Therefore, one can conclude from figure 6.4 and figure 6.5, all dark star models are too faint at $z \geq 6$ to be detected by JWST, even if the exposure times are as large as $100h$[71]. The hope to observe high redshift isolated dark stars is via gravitational lensing provided by the foreground galaxy cluster. Galaxy clusters at redshift $z \approx 0.1 - 0.6$ can in principle boost the fluxes of high redshift objects by up to factors ~ 100 [71].

The cool $(T_{eff} \leq 30000K)$ and long-lived stars with lifetime $\tau \gtrsim 10^7 yr$ dark stars may well be detected at $z \approx 10$ is sizeable numbers within a single, ultra deep JWST

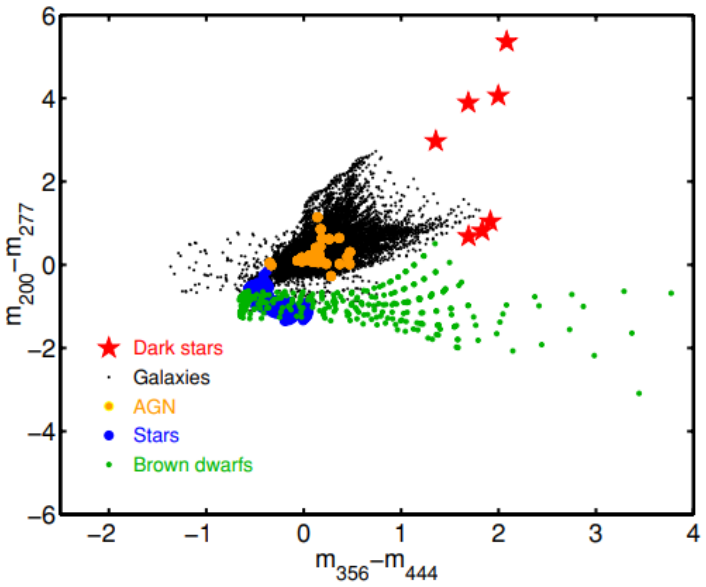

FIGURE 6.6: In multiband surveys, the JWST/NIRCam $m_{356}m_{444}$ vs. $m_{200}m_{277}$ colours of $T_{eff} < 10000K$ dark stars at z= 10 (red star symbols) were compared to a number of potential interlopers. Because dark stars dwell in an area of this colour-colour diagram that is distinct from the regions inhabited by these other objects, deep multiband JWST/NIRCam surveys should be able to locate potential dark star candidates. Credit:[71]

field if one take advantage of the magnifying power of a foreground galaxy cluster. In case of high lifetimes for example $\gtrsim 10^8 yr$ and cosmic star formation scenarios which imply significant dark star formation at $z < 15$, several dark stars may be seen even if only a minor fraction of all POPIII stars forming in minihalos become dark stars with temperatures in the detectable range[71].

Now the question rises how to distinguish the isolated dark stars from other objects observed by the JWST. This is demonstrated by figure 6.6, where the authors of [71] plot the colour indices $m_{356} - m_{444}$ vs $m_{200} - m_{277}$ at redshift $z = 10$ for all dark star models assumed by the authors of [71] with $T_{eff} < 10000K$. The colour of these models, red star symbols, are compared to a number of potential interlopers in multiband surveys: star clusters or galaxies at $z = 0 - 15$(black dots)[74], Active Galactic Nuclei template spectra at $z = 0 - 15$(yellow dots)[75], Milky Way stars with $T_{eff} = 2000 - 50000K$ and metalicity $Z = 0.001 - 0.020$(blue dots)[76] and Milky Way brown dwarfs with $T_{eff} = 130 - 2200K$(green dots)[77][78]. Because dark stars dwell in an area of this colour–colour diagram that is distinct from the regions inhabited by these other objects, deep multiband JWST/NIRCam surveys should be able to find potential dark star candidates.

The Hubble Space Telescope has conducted a number of deep imaging surveys, including the Hubble Ultra-Deep Field (HUDF) and Extreme Deep Field (XDF). HST has successfully identified galaxies at redshifts $z \sim 7 - 10$, using the dropout technique, which is pioneered by [79]. [80] and [81] found a candidate $z \sim 10$ object in the co-added first and second year observation of the HUDF with the new WFC3/IR camera as a J-band dropout. This object is assumed to be a galaxy since its spectral energy distribution matches that of galaxies at $z > 9$ and it looks to be clearly extended[81]. But the absence of spectra and the poor spatial resolution of the image allow us to consider the possibility that this object could be a SMDS candidate. It is

hard to identify a dark star uniquely with the Hubble space telescope, it can be said that at most one candidate has been found that can be used to place bounds on the number of dark stars at redshifts up to $z = 10$[70].

Figure 6.7 and 6.8 (credit: [70]), show the predicted apparent magnitudes of dark stars of $10^6 - 10^7 M_\odot$ at various redshifts and compare these predictions to sensitivity of various HST surveys, plotted as thin horizontal lines, in two HST filters, J-band coloured blue and H-band coloured in red. The author assumed in these figures that the SMDS born at $z = 15$ and sustained through different redshifts are depicted. In figure 6.7, the dark stars are assumed to be developed by the extended adiabatic contraction process, with no captured dark matter, whereas figure 6.8 considers the capture situation.

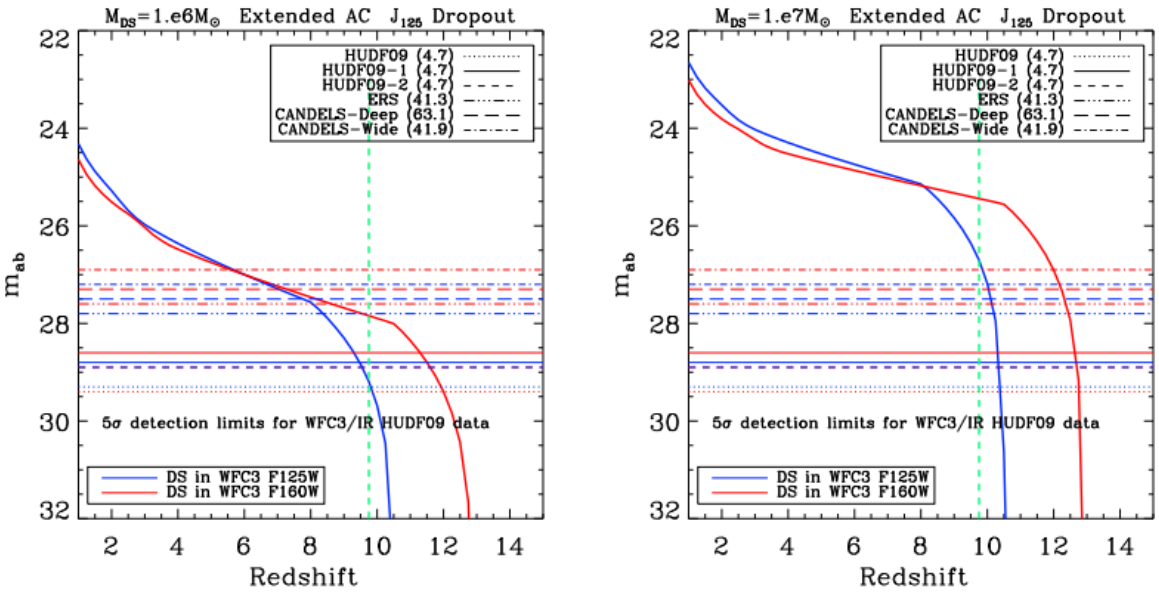

FIGURE 6.7: The thick curves represent the apparent magnitudes. The apparent magnitudes in the H and J bands for $10^6 M\odot$ vs the redshift detection for Dark Stars generated by extended AC in a $10^7 M_\odot$ halo at redshift of 15 are shown in the left panel. For the right panel, apparent magnitudes in the F160W(solid red), and F125W (blue curves) for a $10^7 M_\odot$ halo at redshift 15 vs the redshift of observation for dark stars generated by extended AC in a $10^8 M_\odot$ halo. The 5σ detection limits of the several deep field surveys gathered by [81] are represented by thin horizontal lines, with the survey areas in $arcmin^2$ stated in the legends. HUDF09 is the most comprehensive survey to date (lowest dotted horizontal lines). The vertical dashed line represents the minimal redshift at which the J-band dropout requirement is met ($z \sim 10$). Credit:[70]

The super massive dark stars which grew via capture of dark matter are hard to detect because since they are hotter, their peak output is at lower wavelengths where Lyman-α absorption is worse. Furthermore, their radii are 5-10 times smaller than the dark stars which grew via adiabatic contractions, thus lowering their bolometric luminosities.

For dark stars with masses $\leq 10^5 M_\odot$, the fluxes are too low for the filters to be seen in the HST data. The only way around is that these stars are gravitationally lensed as discussed earlier in this section, i.e. the work of [71]. On the other hand

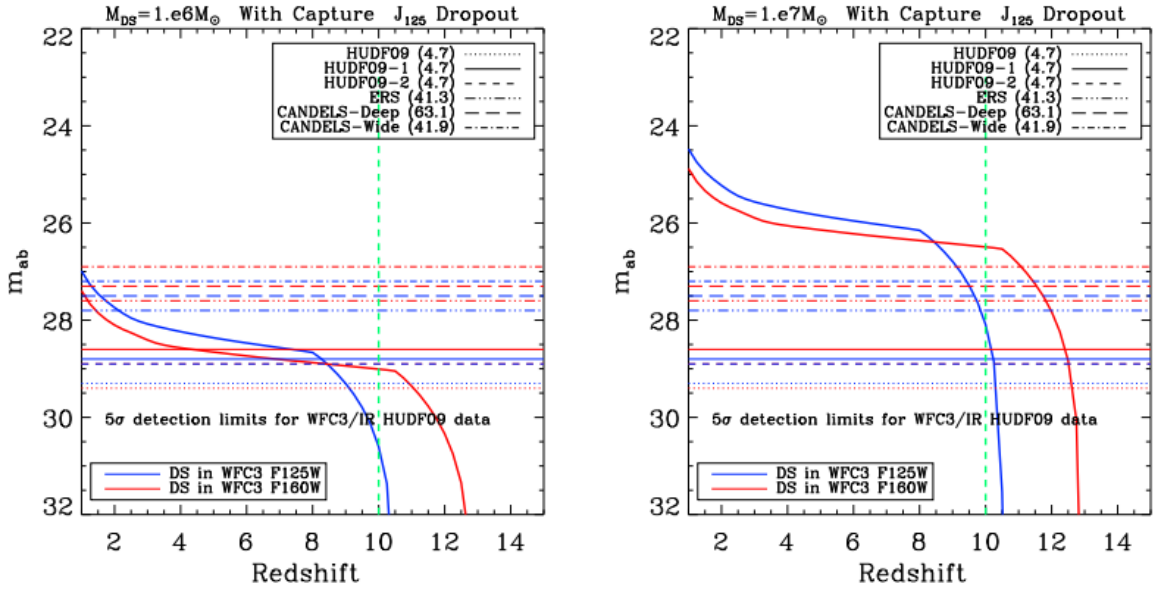

FIGURE 6.8: For 10^6 and $10^7 M_\odot$ dark stars powered by captured Dark Matter. The sensitivity limits for the deepest survey available, HUDF09, are represented by the dashed horizontal lines. The green vertical line represents the lowest redshift at which the dropout criteria is met. Credit:[70]

$10^6 M_\odot$ dark stars can be seen in the F125 (F160) passbands out to redshifts of 9(11.5) while the $10^7 M_\odot$ dark star would be detectable out to redshifts of 10(13)[70].

Because the $10^7 M_\odot$ dark stars are too bright to be consistent with HST data and many magnitudes brighter than the HST sensitivity, the candidate discovered at $z = 10$ is just bright enough to be observed. Therefore, [70] concludes that the object cannot be a dark star of mass $10^7 M_\odot$. But the authors put forward the argument that if any super massive dark stars that continued to exist to $z = 6$ would have been seen as an i_{775} dropout in the HUDF which has a $29.9 m_{AB}$ detection limit for 10σ detection in the i_{775} passband [72]. As no candidates are found in the data, it is apparent that SMDS did not survive until $z = 6$, and it may be inferred that the $10^6 M_\odot$ SMDS is the best potential explanation for the J-band droupout observed by the HST at $z = 10$. Using the plots shown in figure 6.7 and 6.8 the authors of [70] have also put constrain on the number of dark stars. Putting constrains on dark stars requires a more detailed discussion. Kindly refer to [70][82][83] for so.

Supermassive dark stars are visible in all wavelength bands of the JWST's NIR-Cam, however observation is more challenging in less sensitive higher wavelength MIRI camera. The authors of [70] showed that the supermassive dark stars could be seen as J-band, H-band, or K-band dropouts, which would identify them as $z \sim 10, 12, and 14$ objects respectively. In case of finding J-band dropouts, JWST is not that much better than the HST as concluded by the authors of [70]. They also conclude that the the JWST is much more better in finding dark stars in H-band and K-band dropouts and therefore predicted the number of dark stars observed by JWST:

For H-band dropout[70]

$$N_{obs} = \begin{cases} 4.4 \times 10^5 f_{smds} f_{\Delta t} \, (\theta/150 arcmin)^2 & M_{DS} = 10^6 M_\odot \\ 2.4 \times 10^3 f_{smds} f_{\Delta t} \, (\theta/150 arcmin)^2 & M_{DS} = 10^7 M_\odot \end{cases} \tag{6.1}$$

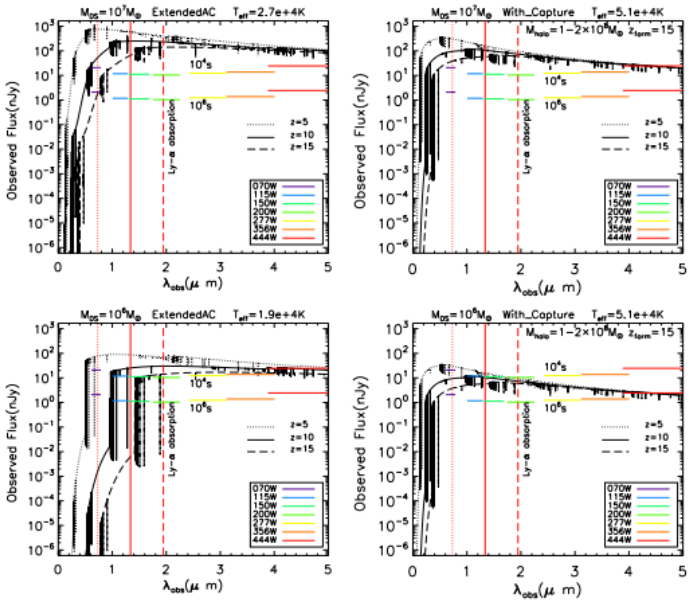

FIGURE 6.9: In comparison to the sensitivity of the JWST filter, SMDS spectra were created at $z_{from} = 15$. The masses of the dark stars (in solar masses), the birth process (extended AC or with capture), and the surface temperature T_{eff} are all displayed above in each panel. The fluxes are plotted at z=15 (dashed line), 10 (solid line), and 5 (dotted line), and are thus compared to the detection limit of the NIRCam broad passband filters. The colored horizontal lines show the filters' sensitivity limitations for exposure periods of 10^4s (upper lines) and 10^6s (lower lines), as specified in the caption. The $Ly\alpha$ line ($1216\dot{A}$) is redshifted from the rest frame of the star, and IGM absorption decreases measured fluxes at wavelengths shorter than the vertical red lines, which indicate the $Ly\alpha$ line ($1216\dot{A}$).Credit:[70]

Similarly, the number of dark stars observed by the K-band dropouts are[70]:

$$N_{obs} = \begin{cases} 7 \times 10^4 f_{smds} f_{\Delta t} \, (\theta/150 arcmin)^2 & M_{DS} = 10^6 M_{\odot}(AC) \\ 120 f_{smds} f_{\Delta t} \, (\theta/150 arcmin)^2 & M_{DS} = 10^7 M_{\odot} \end{cases} \tag{6.2}$$

The authors of [70] also concluded that "$10^6 M_{\odot}$ dark stars formed via Capture are not detectable" for K-band dropout. The authors throughout their work emphasised that $f_{SMDS} f_t 1$.

The fraction of dark matter halos in a given mass range that may host a dark star is f_{smds}, and the fraction of the observational window of time (Δt) during which the dark star is alive is $f_{\Delta t}$. The cosmic period passed between the minimum and highest redshifts at which the dark star might be detected as a dropout is Δt. θ is the total area examined in which the SMDS may have been discovered.

From equations 6.1 and 6.2 it is evident that the number of dark stars that can be observed is large but the main issue is to distinguish them with galaxies containing POPIII stars. The authors of [70] in their work conclude that the best bet is to look for emission lines of $He1640$ or $H\alpha$, if JWST is used for observation.If these lines are detected, the observed object is most likely a POPIII galaxy rather than an SMDS. If these lines are not found then JWST will have trouble in differentiating between SMDS and POPIII galaxies.Therefore, more estimations utilizing telescopes like as the Giant Magellan Telescope, TMT, LSST, and others are necessary.

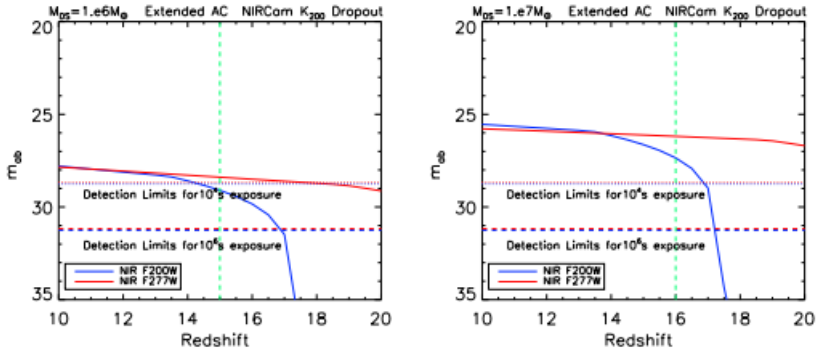

FIGURE 6.10: SMDS observed as K200-band dropouts with JWST: apparent magnitudes for SMDS created not by DM capture using the NIRCam filters F200W and F277W. The $10^6 M_\odot$ DS is represented by the left-hand panel. The right-hand panel is for the $10^7 M_\odot$ DS. The minimal redshift at which the DS will come up as a dropout is indicated by the vertical green dashed line.Credit:[70]

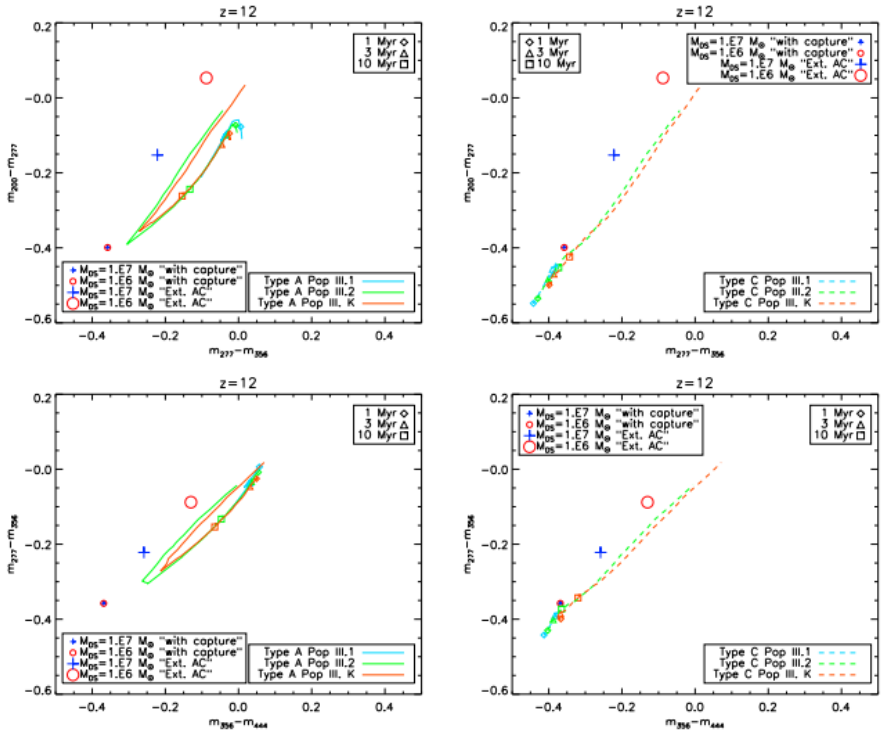

FIGURE 6.11: Signatures of SMDS and instantaneous burst Pop III galaxies in $m_{277} - m_{356}$ vs. $m_{200} - m_{277}$ (top row) and $m_{356} - m_{444}$ vs. $m_{277} - m_{356}$ (bottom row) colour diagrams. Type A Pop III galaxies (maximal nebular emission) are represented on the left column, whereas type C Pop III galaxies are represented on the right column (no nebular emission). The solid lines are evolutionary tracks for Pop III galaxies obtained using the YGGDRASIL model grids introduced in [84]. The points on the evolutionary tracks distinguish the evolution of the galaxies at three distinct ages. $10^6 M_\odot (10^7 M_\odot)$ SMDS, in the diagrams are represented by circle (cross) symbols. For the extended AC case, we chose a larger size symbol compared to the SMDS formed 'with capture'.Credit:[70]

6.3 Dark Star signatures in CMB and Re-ionization

As evident from section 6.2, observing dark stars directly is a difficult task. For observing dark stars using JWST with mass $\leq 10^5 M_\odot$, the star needs to be isolated and magnified by gravitational microlensing or they are present together in a cluster, i.e. a star cluster with majority of them are dark stars. Furthermore the SMDS are infact visible with JWST but distinguishing them from POPIII galaxies is a difficult job and therefore require more observations from other telescopes.

In this entire section the work of [85] has been discussed which looks into whether the dark star's life have an effect on the Cosmic Microwave Background and re-ionization of the Universe. If these signatures can be seen on the CMB or reionization history of the Universe, we can, therefore, observe dark star indirectly. The authors of [85] defined different structural forms for dark stars, depending upon the degree to which they are dominated by the dark matter.

1. Dark Star Proper (DSP) occurs when the dark matter annihilation contributes a substantial amount to the energy budget of the star and shows characteristics as shown by [1]. These objects are located far off to the right of the HR diagram, in the protostar area.

2. The Dark Star Near Main Sequence (DSNMS) structure develops when dark matter provides just a small portion of the overall energy budget of the star and is very similar to the main sequence star. They are slightly to the right of a normal POPIII major sequence on the HR diagram.

The structure of a dark star is determined by its age and the pace at which dark matter is captured and annihilated into heat. Usually the DSNMS stage always following the DSP stage. Sustained high rates of capture and annihilation of dark matter effectively increases the duration of the DSP. However, sustained moderate capture rates lengthen the DSNMS stage because the star is sustained by both dark matter annihilation and nuclear fusion in a significantly cooler form than the corresponding main sequence structure.

Three distinct capture scenarios are defined by the authors of [85]:

1. No Capture (NC) is the canonical scenario. Because the annihilation of gravitationally constricted dark matter at their core hinders the collapse, dark stars form as a result of gravitational collapse and evolve to be larger in mass than typical POPIII. 1 star. After the first gravitationally squeezed dark matter is depleted, the star completes its contraction and enters the main sequence, where it lives like any other $\sim 800 M_\odot$ star.

2. The Meager capture (MC) scenario is one in which we have quite enough dark matter capture to prolong the DSNMS phase's duration.

3. The Extreme capture (EC) scenario captures enough dark matter to lengthen the duration of the dark star's DSP phase.

Refer to Table 1 of [85] for various parameters and results of the models the authors used to simulate the effects of dark stars on the CMB and reionization. The authors of [85] provided the following results. All the credit is given to them.

6.3.1 Effects on Reionization

Under the NC scenario, the Universe's reionization history is substantially alike for all values of the dark star fraction, f_{DS}, where the dark stars are powered only by

gravitationally contracted dark matter. This is despite the fact that the dark stellar population contributes nothing to reionization during the first $0.4Myr$ of star formation, reducing Q_{tot} to $(1-f_{DS})Q_{PopIII}$, where Q_{tot} is the combined star population's weighted-average, mass-normalized, hydrogen-ionizing photon output. and Q_{PopIII} is the photon flux output per unit mass by the POPIII stars[85].

Because $Q_{DSNMS} > Q_{POPIII}$, the earlier shortage of ionizing photons is accounted for in the subsequent DSNMS phase by an excess relative to the canonical condition in which $f_{DS} = 0$ and only typical POPIII stars followed by POPII stars exist. The net consequences of these two effects on the reionization redshift balance out.

Figure 6.12 (Credit: [85]) depicts a zoomed-in portion of the entire history of reionization for a few choices of f_{DS} and the DSNMS lifespan t_{DSNMS} in the MC scenario. Increasing the f_{DS} and t_{DSNMS} causes reionization to occur sooner. This is due to the fact that $Q_{DSNMS} > Q_{POPIII}$, therefore prolonging the DSNMS phase and ramping up the proportion of baryons included in it allows reionization to occur more quickly than with just a regular POPIII IMF. With rising f_{DS} and t_{DSNMS}, these effects get stronger. The MC scenario has a far lesser influence on reionization in comparison to EC, since its duration is already highly controlled, in this case by the core hydrogen fusion-burning period during the DSNMS.

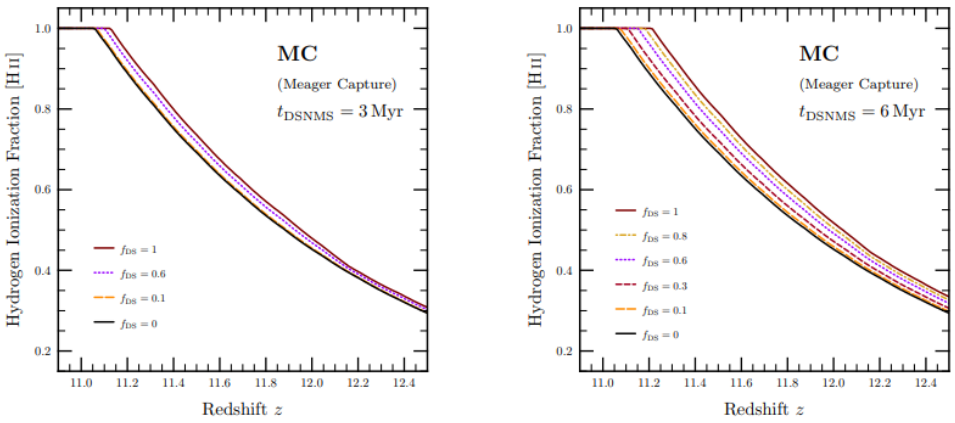

FIGURE 6.12: The meager capture (MC) scenario of dark star , ionization histories of a Universe is shown. The two panels examine histories for various dark star fractions f_{DS}, where they (dark stars) spend near to the maximum time allowed by core hydrogen depletion in the DSNMS phase ($t_{DSNMS} = 3$ and 6 Myr). DSNMS lifespans that are long and bigger dark star fractions cause a modest increase in reionization speed. Credit:[85]

The ionization histories in the EC scenario are shown in Figure 6.13 (credit: Credit:[85]) for various combinations of f_{DS} and t_{DSP}. Because Q_{tot} remains at lower levels for longer durations during the early phases of star formation in each halo, reionization delays with large f_{DS} and t_{DSP}. The higher the values of f_{DS} and t_{DSP}, the larger the impact. Following the death of the dark star population, they are either promptly replaced by new Pop II stars, or by newborn Pop III stars, who eventually die and are replaced by new Pop II stars, depending on the period of death.

For longer delays, as IGM ionization becomes more capable of building up quickly, reionization happens more quickly. This is due to two factors: the major source of ionizing photons coming on at lower redshifts, and the IGM density quickly reducing as redshift decreases, resulting in longer IGM recombination durations at later

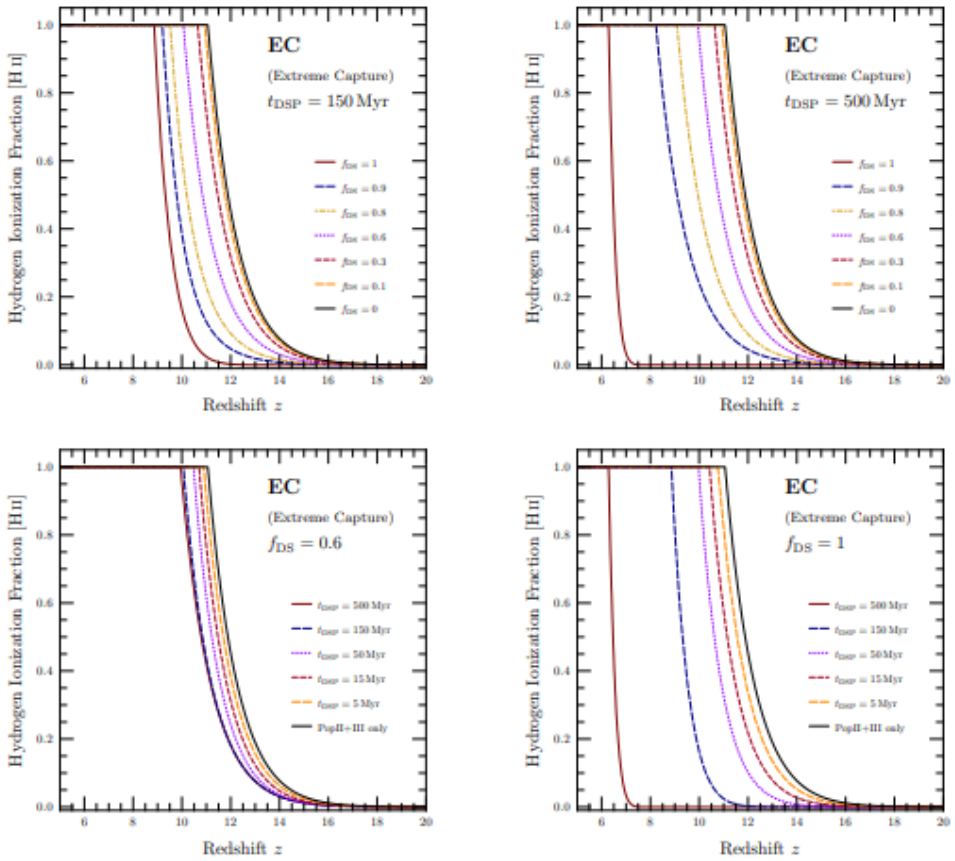

FIGURE 6.13: In the extreme capture (EC) scenario, the ionization histories of a Universe with dark or semi-dark star populations is shown. The plot shown depicts the proportion of hydrogen in HII as a function of redshift. In scenarios when dark stars spend a long period in the DSP phase (t_{DSP}= 150 Myr and 500 Myr), the top panels analyse histories for various dark star fractions f_{DS}. Bottom panels analyse histories for various DSP lifetimes when dark stars account for a significant portion of the mass budget of the initial stars' population (f_{DS}= 0.6 and 1). Longer-lasting and more abundant EC dark stars postpone reionization. Credit:[85]

cosmic periods. This explains why raising t_{DSP} rather than increasing f_{DS} increases the speed of reionization [85].

6.3.2 Impacts on Cosmic Microwave Background

The NC case have no impacts on the optical depth of electron scattering as they don't have any effect on the Universe's reionization history. The electron scattering optical depth is less for longer lived and more numerous dark stars in the EC case, as predicted, because they reionize the Universe later. The authors of [85] also depict τ_e as a continuous function of t_{DSP} and f_{DS} in Figure 6.14, which summarizes the integarted optical depths over the full EC parameter space.

Figure 6.15 (Credit:[85]) shows a zoomed-in segment of the optical depth curves for the MC case's longest-lived dark star. Smaller variations in reionization history have a smaller and opposite effect on τ_e, resulting in somewhat larger optical depths than in the absence of a dark star.

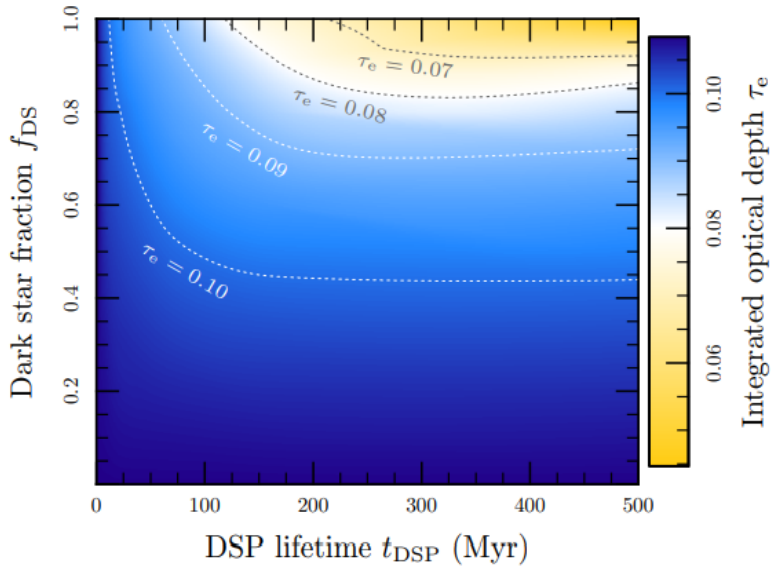

FIGURE 6.14: In the EC scenario, profiles of equal integrated CMB optical depth to $z = 1090$ as a function of f_{DS} and t_{DSP}. Longer lives and higher dark star fractions results in reduced integrated optical depths; the modest upturn in the $\tau_e = 0.08$ and 0.09 contours at large t_{DSP} is an interpolation artifact.Credit:[85]

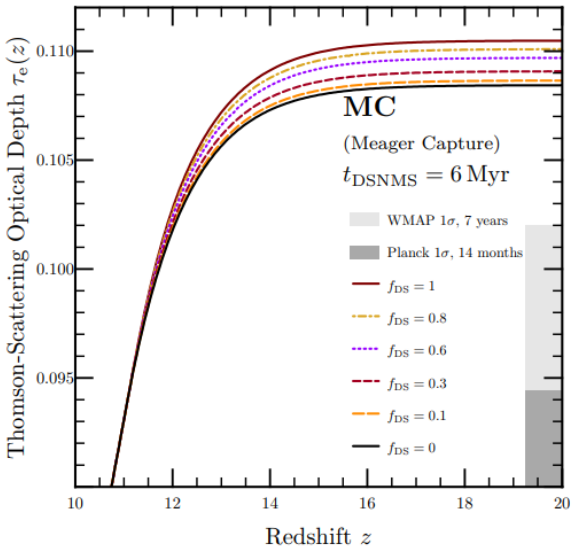

FIGURE 6.15: For MC dark stars with the maximum allowable DSNMS lifetime ($t_{DSNMS} = 6Myr$), the evolution of the lookback optical depth from now to redshift z. Early reionization in the MC scenario is induced by increasing f_{DS} values, which results in a minor rise in optical depth. Credit:[85]

Figure 6.16 (Credit:[85]) depicts the effects of several astrophysical factors on the evolution of the electron scattering optical depth with redshift (left panel) and EE polarization angular spectra (right panel).

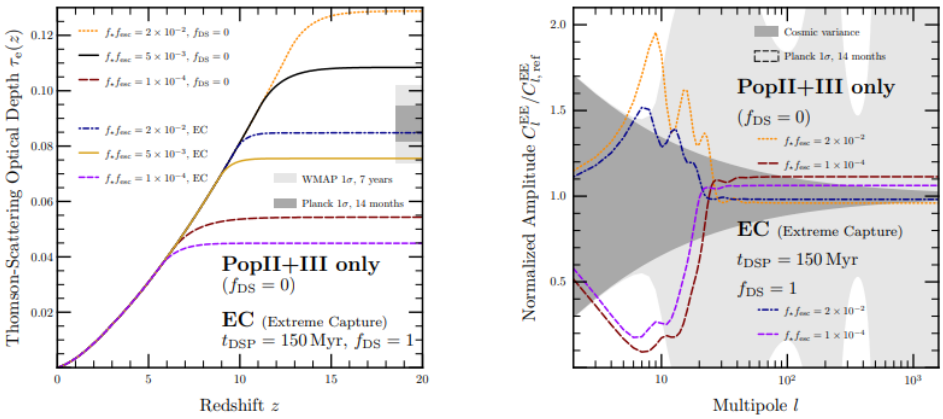

FIGURE 6.16: Variable astrophysical factors' effects on the evolution of electron-scattering optical depth with redshift (left) and EE polarization angular power spectra (right) is shown. The consequences of varying the product $f_* f_{esc}$ are demonstrated, both for a universe with no dark stars ($f_{DS} = 0$) and one with EC dark stars with $t_{DSP} = 150 Myr$, $f_{DS} = 1$. The curves in the right panel have been normalized to the appropriate EE spectra obtained by setting $f_* f_{esc} = 0.005$. As with EC dark stars, changes in astrophysical parameters might cause variations in optical depths and EE spectra.In contrast to EC dark stars, which can only stall reionization, changes in f_* and f_{esc} can also speed reionization, resulting in larger optical depths and enhanced large-scale power in the EE spectrum.Credit:[85]

6.4 Signatures on EBL

The extragalactic background light (EBL) is a fundamental cosmological observable quantity, defined as emission in the wavelength range of 0.1 to 1000μm. It is comprised of light from resolved and unresolved extragalactic sources, as well as any really diffuse background other than the cosmic microwave background (CMB). Since the recombination, it has served as a reservoir for all energy created by nuclear and gravitational processes. Cosmic expansion and dust absorption and reradiation shift a considerable portion of this radiation into infrared (IR) wavelengths. As a result, its spectral structure and intensity have provided critical information on the formation and evolution of galaxies, as well as their stellar and interstellar constituents, across cosmic history. The integrated light from resolved galaxies, also known as the integrated galaxy light(IGL), provides a stringent lower limit on the EBL intensity[86].

The work of [87] investigates the detectability of dark star generated signatures in the EBL. This method provides a new way for looking for dark matter effects ,the near-infrared spectrum (NIR). The formula giving the peak EBL contribution at z = 0 from a DS population normalized to the fiducial DS parameters[87]:

$$(\nu I_\nu)_{max} = 2 \times 10^{-5} nW m^{-2} sr^{-1} \times \left(\frac{\Delta t_{DS}}{10^7 years}\right) \times \left(\frac{SFR_{Norm}}{10^{-5}}\right) \times \left(\frac{LMR}{10^3 L_\odot / M_\odot}\right) \times \left(\frac{z_{min}}{10}\right)^{-2.5} \tag{6.3}$$

where SFR is Star Formation Rate, LMR is luminosity-to-(stellar)mass ratio.

Figure 6.17 depicts the peak EBL contribution for three values of z_{min} with regard to varied dark star lifetimes. For dark stars with lifetimes smaller than $(t(z_{min}) - t(z_{max}))$, the resultant EBL scales linearly with rising Δt_{DS}. At lifetimes higher than

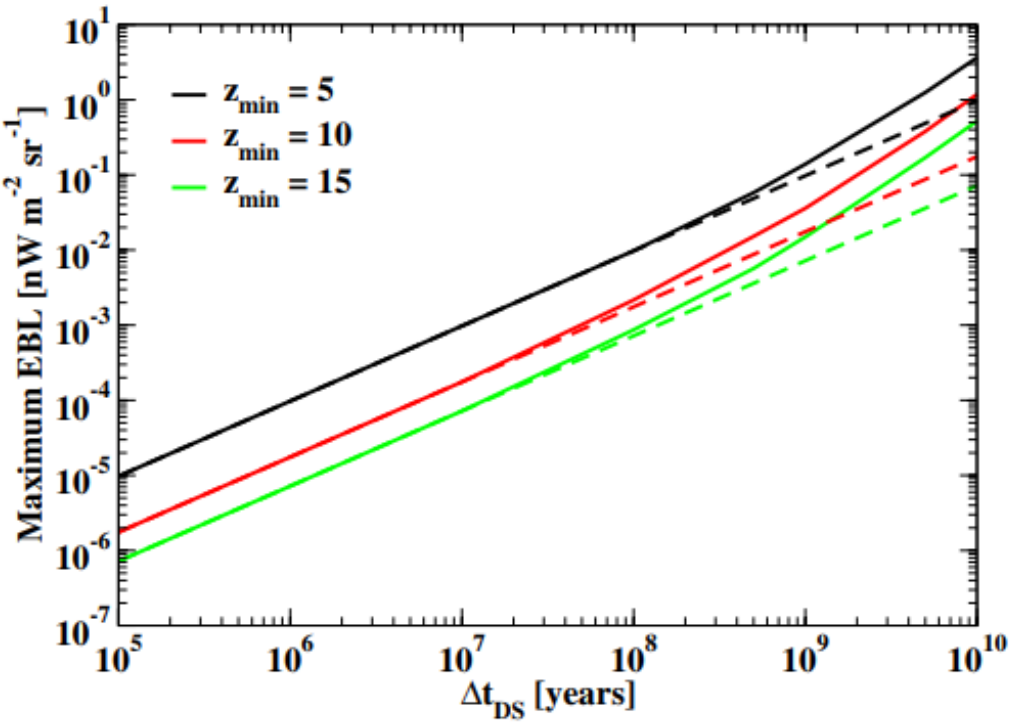

FIGURE 6.17: Peak EBL contribution for the 7500K dark star model[87] as a function of dark star lifetime; for SFR_{Norm} the fiducial value of 10^{-5} is used.Credit:[87]

$\sim 10^8$ years, the strength of the EBL increases, and the peak value of the dark star signature shifts to lower wavelengths (Figure 6.18). This is due to contribution from residual emissivity at lower redshifts z. If Δt_{DS} is short enough, the end of dark star formation is nearly comparable to the end of dark star photon emission, since the number of dark stars reduces practically quickly. The dashed lines shows a linear relationship between Δt_{DS} and the maximum EBL flux. For dark stars with lifetimes $\Delta t_{DS} 10^{10}$ years, as displayed in Figures 6.17 and 6.18, would be still present in today's universe and therefore most likely to be detected[87].

The work of [88] puts constraints for massive as well as light dark matter candidates from the observed x-ray, gamma-ray, and neutrino background, considering dark matter profiles which have been steepened during the formation of dark stars.The authors, furthermore, showed that in order to satisfy the WMAP (Wilkinson Microwave Anisotropy Probe) optical depth constraint and the Gunn-Peterson constraint at $z \sim 6$, such dark star models might need a somewhat an artificial reionization history based on a double-reionization phase and a late star burst close to redshift $z \sim 6$. If dark stars were common in the early universe, models that anticipate a large amount of UV photons, similar to conventional Pop. III stars, are preferred.

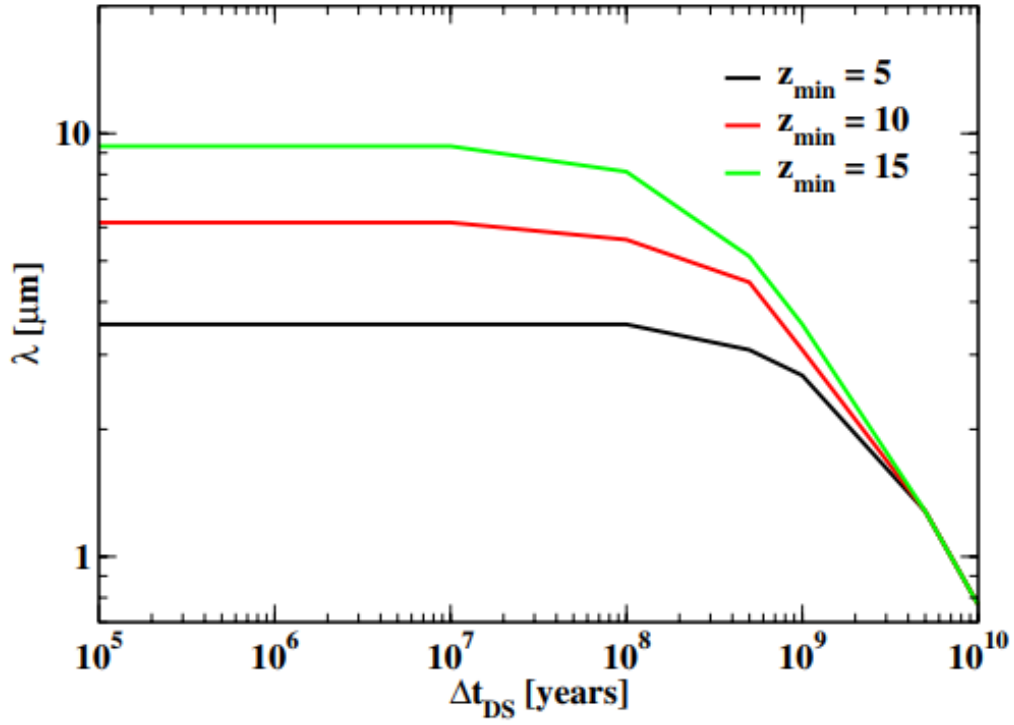

FIGURE 6.18: For the 7500 K dark star model, the location wavelength of the peak in the EBL SED as a function of dark star lifetime is shown. The results converge toward the intrinsic emission maximum for $\Delta t_{DS} > 10^9$ years, suggesting that dark stars still produce light at z = 0.Credit:[87]

Chapter 7

Open Questions and Discussion

7.1 Paradox of Youth

The surprising fact that the central parsec contains $\sim$ 200 young and massive stars, and is one of the richest massive star formation region in the Milky Way[89]. The presence of a super-massive black hole associated with Sagittarius A^* makes it unexpected to find so many young stars in its vicinity[89].The central $30pc$ of the Milky Way contains a $3-4\times10^6 M_\odot$ black hole, but also two of the densest star clusters in the Galaxy which includes the Arches cluster(figure 7.1). For gravitational collapse to happen in the presence of the tidal shear from the central black hole, gas clouds have to be denser than the critical *Roche* density

$$n_{Roche}(R) \sim 6\times10^{10}\left(\frac{R}{0.1pc}\right)^3 cm^{-3} \tag{7.1}$$

which exceeds several orders of magnitudes the density of any gas currently observed in the central region($\sim$ $10^3 to 10^8 cm^3$) [90][91][92]. In the late 1980s, a star with broad HI and HeI emission lines was detected less than $0.5pc$ from the central compact radio source, $SgrA^*$ [93][94]. Over next few years, an increasing number of such stars were discovered, which appear to be helium-rich blue super giants and Wolf-Rayet stars, with masses of up to $100M_\odot$[95][96].

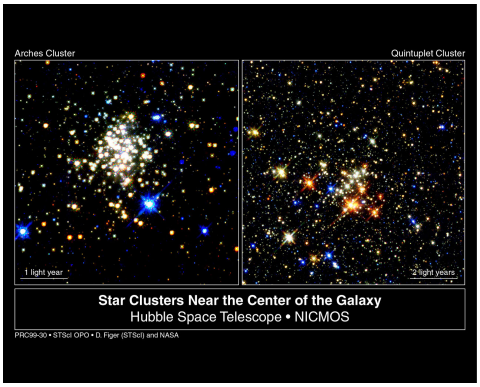

FIGURE 7.1: Star Clusters near the center of the galaxy. Credit: Don Figer (Space Telescope Science Institute) and NASA/ESA, https://esahubble.org/images/opo9930a/

This unexpected presence of young stars close to galactic center is known as the "*Paradox of Youth*"[97][98][99]. Recent work has increased the number of known OB stars in the central parsec of the Galaxy to close to 100, excluding the central square arc-second [100]. These young stars appear to form two counter-rotating discs, implying that they may be related with distinct star formation processes amid dense

accreting matter[100][101][102]. The work of Andrea M. Ghez and Reinhard Genzel, who were the recipient of the Nobel Prize 2020 ,along with Sir Roger Penrose[103], gave us the fact that the $SgrA^*$ is the location of the supermassive black hole candidate.

With the subsequent tracking of stars even closer than the young HI stars, a cluster of stars was discovered in the 1990s within the central square arcsecond and named as $SgrA^*$ stellar cluster[104]. This cluster's stars, known as S stars, E stars, or SO stars, travel incredibly near to the central black hole. The star which has been observed moving closest to the central black hole are S14, E2 or SO-16, and was seen within $45AU$, or only 600 Schwarszchild radii, of the black hole [105]. The $SgrA^*$ cluster's kinematics are such that stars have randomly oriented, extremely elliptical orbits rather than circular ones bound to a single disc. Near-infrared observations of the S stars made with the Keck and VLT telescopes showed that their atmospheres did not contain CO[104] which set a lower bound on their surface. Furthermore, it was concluded that the S stars are in fact simply $10 - 15M_\odot$ main-sequence stars[105][106].

Several scenarios have been proposed to solve this paradox: in situ formation in a dense gas accretion disk that can overcome the tidal forces[107]; rapid in-spiral of a compact, massive star cluster that formed outside the central region [108], and re-juvenation of older stars by collisions or stripping [102][109][110]; efficient transport mechanisms, such as relaxation by massive perturbers and three-body collisions[111][112][113][114] that act on time scales faster than the classical two-body relaxation time[89].

How dark stars can be involved in solving this paradox? We have seen that the stars that use dark matter annihilation as their main source of energy have significantly increased main-sequence lifetimes. Subsequently there's the possibility that stars form elsewhere and then move to the Galactic center, where the abundance of dark matter prolong their lives. This might provide an alternative explanation for either the S stars or the outer stellar discs of the OB-type stars [67]. However, the issue with models in which stars are born elsewhere and then move to the galactic center is that the inspiralling timescale is generally large in comparison to their main sequence lifetime; thus, one would expect the stars to exit their main sequence phase once they reach the galactic center. Also, we have seen in chapter 4, more the massive is the star more dark matter density it needs to become a dark star. Therefore it is unlikely that a star as massive as $10M_\odot$ can capture enough WIMPs to have some effects on its structure [67].

In [67], the authors further stated that such stars can reach the end of its main sequence lifetime during migration. When they arrive at the Galactic center, these stars can start capturing large amount of WIMPs. If the burning of dark matter throughout a star's post-main-sequence growth led it to resemble an OB or Wolf-Rayet star, or if it returned to looking externally like a main sequence star, this may explain thick stellar discs or S stars. Such explanation for the paradox should be considered improbable, but it is interesting to consider that the S stars are indeed on more elliptical orbits than other stars at galactic center[115] which will be an excellent condition for these stars to accrete more dark matter than others.

To support the last statement i.e., more elliptical orbits are an excellent situation for increased dark matter accretion, the authors of [67] presented a series of detailed grids of WIMP-influenced stellar models for main sequence stars (for example Figure 5.4). They also illustrate what rates of energy injection may be obtained using actual orbital parameters for stars in the galactic center, including careful consideration of the velocity and density profile of dark matter. The authors of [67] concluded

the following:

1. Stars in the Milky Way with circular orbits are highly unlikely to acquire significant capture rates. However, if the stars in a binary system are on circular orbits, the capture rates can be increased.

2. Stars in elliptical orbits near to the Galactic center have significantly higher capture rates than those in circular orbits.

3. The velocity distribution of dark matter close to the Galactic center might be extremely non-Gaussian, increasing the rate of dark matter capture by stars in elliptical orbits in the Galactic center.

4. Supposing that the nuclear-scattering cross-sections are equal to their present experimental limits, dark matter makes up a spike around the Galactic center, and that the dark matter distribution has gone through adiabatic contraction at a larger scale, stars of solar mass and less will reach break-even between annihilation and fusion energy on orbits with periods of up to 50 years and eccentricities as low as 0.9. Stars with a mass of $1.5M_{\odot}$ can attain the same objective with comparable eccentricities if they orbit the core black hole in fewer than 10 years.

5. Without adiabatic contraction of the galactic halo, stars of a solar mass or less must have orbits as shorter as 10 years and eccentricities as low as 0.99.

6. The above-mentioned conditions are expected to be greatly eased for stars in a binary system. The impact of WIMP dark matter annihilation would be difficult to ignore in a system composed of a low mass protostar and a extremely evolved massive star.

7.2 Effects of dark matter at different stellar phases

In Chapter 3 we have seen that a protostar can collect dark matter by adiabatic contraction. This can be described either using Blumenthal method of adiabatic contraction or Young's method. Both method are successful to accrete enough dark matter to annihilate and dominate over rest of the heating/cooling mechanisms in the star. In Chapter 4 we have discussed another way via which a star can capture dark matter that is via scattering capture. Till now we have seen the effects of dark matter on stars when they are in the main sequence stages which has been covered in chapter 5.

But not much work has been done on the effects of dark matter on the stars when they exist their main sequence stages.[116] and [117] studies the effects of dark matter on low mass red giants with masses $< 2.3M_{\odot}$ and $0.8 - 1.4M_{\odot}$ respectively. Both work concluded that the dark matter makes the helium burning phase begin earlier i.e. early ending of the RGB phase. This is due to the increased mass of the core due to dark matter collection, which in turn increases the luminosity of the star and making the condition ideal for early beginning of the helium burning phase of the red giant. No work has been done so far for intermediate $(> 2.5M_{\odot})$ and massive $(> 8M_{\odot})$ red giant stars.

The end stages of stellar evolution is marked by an explosion, depending on the properties of the red giant, is either a Type I Supernova, Type II Supernova or a Nova. The remnants are either a black hole or neutron star for the former two and

a White Dwarf for the latter. The works of [118][119][120][121][122], to name a few, discusses various aspects of effects of capture of dark matter on neutron stars and how these stars can be an excellent laboratories to study the properties of dark matter. The works of [123] looks into the capture of dark matter by white dwarfs. Being the most abundant compact stars in the Galaxy, the authors of [123] worked on the dark matter capture rates in the white dwarfs, for dark matter scattering either with nuclei in the stellar interior, or with the degenerate electron component. They also concluded that the old massive white dwarfs in the globular cluster M4 can constrain dark matter-nucleon spin-independent cross-sections beyond the capabilities of current and future direct detection (DD) studies.

The asymmetric dark matter model's effects are also studied in the work of [124], where the authors studies their effects on low mass stars and brown dwarfs. The works of [125][126] studies the dark stars that uses asymmetric dark matter model as fuel. The work of [127] studies the formation and evolution of young low mass stars($0.7 - 3M_{\odot}$) in high dark matter density halos of $10^9 GeVcm^{-3}$.

7.3 Dark Stars in Stellar clusters

Star clusters can be the best places to look for dark stars. They are among oldest objects and contain not hundreds but thousand stars that can be studied effectively. Our own galaxy have about hundred or more clusters, which provide us a huge database to study the stellar evolution. During the birth of a star cluster, if there is enough dark matter accretion via adiabatic contraction on the protostars, then there can be signatures detected of dark matter annihilation and there will be effects on stellar evolution. On the other hand, if a star cluster finds itself in a dense dark matter halo, then the stars can capture dark matter to such an extend that the dark matter annihilation takes over the dominant energy source of the stars, and hence dark stars are born.

The work of [128] tried to see what signatures can be expected from such a scenario. In order to characterise how dark matter annihilation inside stars changes the aspect of a stellar cluster, the authors of [128] computed the evolution until the ignition of the He burning of stars from $0.7M_{\odot}$ to $3.5M_{\odot}$ within halos of dark matter with different characteristics. They came to the conclusion that when a cluster is enveloped by a dense dark matter halo, the cluster's stars positions in the H-R diagram have a brighter and hotter turn-off point than in the traditional scenario without dark matter. This makes the cluster look younger. The high dark matter densities necessary for such effects are only expected in certain regions, such as the Galactic center. If dark matter is a WIMP particle with a mass of 8GeV, this signature is anticipated for a dark matter halo with a density of $\rho_{\chi} = 3 \times 10^5 GeVcm^{-3}$. The gradient in dark matter density within the star cluster would result in a larger main sequence, turn-off, and red giant branch area [128]. The bottom of the isochrones in the H-R diagram rises to greater luminosities for large dark matter halo concentrations, leaving a distinctive imprint on the star cluster. The authors also argue that such signs might be used to infer the presence of dark matter in the cluster's location.

More detailed spectrum energy distribution of various star and dark matter masses are required to fully understand how dark matter effects the stellar evolution. The spectrum energy distribution shown in this thesis work in section 6.1 are either for supermassive dark stars or dark stars with masses from $\sim 100M_{\odot}$. Furthermore, the case study of globular cluster $NGC2419$[129], concludes that the presence of a dark

matter halo around $NGC24194$ cannot be fully ruled out at present, yet any dark matter within the 10 arcmin visible extent of the cluster must be highly concentrated and cannot exceed $1.1 \times 10^6 M_\odot$ (99% confidence), in stark contradiction to expectations for a probable progenitor halo of this structure, which makes them a suitable site for dark star observation.

7.4 Dark Stars as Black Holes

It is now believed that at the center of spiral galaxy like our Milky Way, and AGNs have a supermassive black holes. The formation of such heavy black holes is still an unsolved question. The work of [130] is an excellent work to understand the assembly of the first supermassive black holes. As we have seen, the dark stars can grow as huge as $10^6 M_\odot$. When the dark matter is fully consumed, these stars can collapse directly to black holes, without ever going through the nuclear fusion phase. Such black holes can then act as seeds for supermassive black holes, which can grow via accretions and consumption of gas and other objects.

In standard stellar evolution, the stars with masses ranging from $\sim 150 - 240 M\odot$ are anticipated to evolve into a pair instability supernova with no black hole remnant, resulting in the predicted gap in the black hole mass function of roughly $50 M_\odot$ to $140 M_\odot$, but the LIGO and Virgo Collaborations[131][132] recently discovered black holes of masses $66 M_\odot$ and $85 M_\odot$ in the gravitational wave event $GW190521$. The authors of [133] propose that if an additional energy source is added throughout the star along with nuclear fusion, it is possible for the altered evolution to avoid the complete destruction of a pair instability supernova, and a black hole remnant is left behind. The dark matter annihilation is the source of this additional energy in the star. For a $180 M_\odot$ star (MESA's one-dimensional star evolution atmosphere is being used), if this additional energy source accounts for $\sim$ 50% of the star's energy, the star has the capability of totally avoiding the pair instability and transforming into a core-collapsed supernova and a black hole remnant with mass $\sim 120 M_\odot$.

Furthermore, if dark stars do get fairly big, their mergers should provide a gravitational wave signal.Their gravitational wave signature should differ from that of similar-mass black holes because they are stretched. This might be an interesting approach for LIGO to find dark stars. They are also made up of relatively cool baryons, thus the electromagnetic signature of the event should be substantially different from that of a much hotter accretion disk [2].

7.5 DarkStars

This section is devoted to discuss the capabilities of the dark star evolution code called "DarkStars". This code was developed by [3], which is a modification of the the standard stellar evolution code STARS [134][135][136]. It was to cover the implications of dark matter capture and annihilation DarkStars is written in Fortran95, and can be freely downloaded from `http://www.fysik.su.se/~pat/darkstars` or `https://github.com/patscott/DarkStars`.

DarkStars includes gravitational capture of WIMPs from the galactic halo via the full equations of Gould [137], including both spin-dependent and spin-independent scattering on the 22 most important atomic nuclei. The capture routines are adapted from the solar capture code in DarkSUSY[138]. Capture may be executed semi-analytically from either a standard isothermal WIMP halo or an isothermal halo

with a truncated WIMP velocity distribution at the local escape velocity. Alternatively, numerical capture calculations can be performed on a velocity distribution derived[139] from the Via Lactea[140] simulation of a Milky Way-type galaxy, or any other arbitrary, user-supplied velocity distribution[141][142][143].

The height distribution of WIMPs in a star is calculated by interpolating within two limiting distributions based on the value of the WIMP's mean-free path in the star: one for WIMPs with extremely long mean-free paths and the other for WIMPs with extremely short mean-free paths. Conductive energy transfer between atomic nuclei and WIMPs through weak-scattering events is approximated at each height by re-scaling the known equation for conductive luminosity at short mean-free routes according to the star's actual mean free path. The annihilation luminosity is computed at each height in the star as the product of the annihilation cross-section and the square of the local WIMP density, and this is included into the stellar solver's luminosity equation alongside the conductive luminosity. DarkStars takes a simple text-file input and generates an evolutionary run using a series of switches and physical settings. Switches enable the user to choose between analytical and numerical capture, different halo velocity distributions, the inclusion or exclusion of annihilation and conductive energy transport effects, and the ability to run in a special'reconvergence mode,' in which the solution obtained at each timestep is converged twice. The user may specify the WIMP mass, spin-dependent, spin-independent, and annihilation cross-sections, as well as the stellar mass and metallicity, the initial WIMP population in the star, and the proportion of energy lost to neutrinos in each annihilation. A constant star velocity can also be specified using a WIMP halo with a certain local density and velocity dispersion, placed at a place with a single well-defined Galactic escape velocity. Runs can alternatively be performed along user-defined orbits, in which case these four parameters are replaced with dynamic values given in an additional text file. Orbits can also be looped if needed.

The three exemplar codes that are run here are for a star of $1M_{\odot}$ at a distance of 0.01pc from the galactic center, moving through dark matter WIMP halo at speed $220KM/s$ and galactic escape velocity $600Km/s$. The WIMP Halo velocity dispersion is $270Km/s$ for a WIMP particle mass of $100GeV$. The star has an initial number of WIMPS 10^{30}. The annihilation cross section is taken to be $3 \times 10^{-26}cm^3/s$ ($v \rightarrow 0$, mean over velocity), The spin-independent and spin dependent WIMP-nucleus cross section are $1 \times 10^{-44}cm^2$ and $1 \times 10^{-38}cm^2$ respectively. The energy lost to neutrinos are set to 0.1. A boost factor= 1.0 is also included which to multiply capture rates to mimic ignored effects. Knudsen number at which WIMP energy transport is maximised is set to $K_0 = 0.4$, and Knudsen suppression $\tau = 0.5$ is set which is a relaxation scale for Knudsen dependent suppression function. The WIMP thermalisation timescale is set to $\tau_{Therm} = -1.0$. The abundance of heavy elements are also set. For Carbon and Oxygen abundance the value is set as 8.39 and 8.66 respectively. $Na = 6.17, Al = 6.37, Si = 7.51, S = 7.14, Ar = 6.18, Ca = 6.31, Fe = 7.45, Ni = 6.17 and Pb = 2.00$ are set. The code ends when the star becomes a certified "*WIMP Burner*".

The main difference comes in the local WIMP density, through which the star travels through. For the case of "Normal", the local WIMP density is $\rho = 1 \times 10^{-5}GeV/cm^3$. For "Dark" case, the local WIMP density is $1 \times 10^{9}GeV/cm^3$ and for "Very Dark" case it is $1 \times 10^{10}GeV/cm^3$. Isothermal Maxwell-Boltzmann distribution for halo velocity is considered in all three cases. Keeping the mass of the star almost same throughout the run, for "Very dark" results obtained are shown in Figure 7.2,7.3.

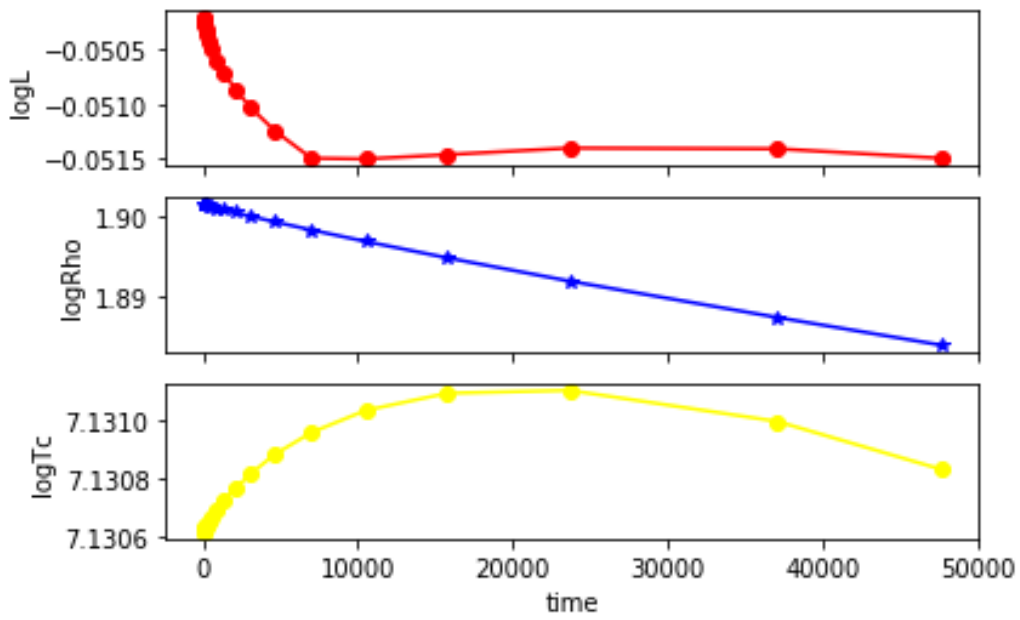

FIGURE 7.2: Various parameters(Luminosity, Density, WIMP isothermal temperature) vs Time in years

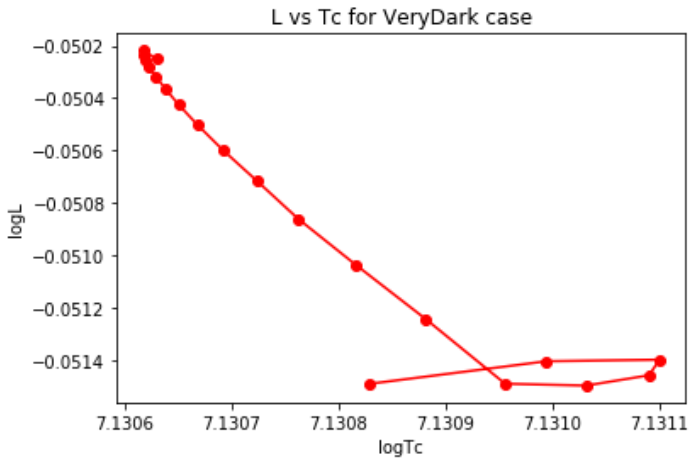

FIGURE 7.3: Luminosity vs Temperature(WIMP isothermal temperature)

Figure 7.2 plots luminosity, density and temperature(WIMP isothermal temperature) versus time (years) elapsed since the star starts capturing dark matter. It is clear that with time the density increases drastically initially but decreases gradually as the star starts to consume dark matter via annihilation which becomes the dominant energy source of the star. Similarly, the star gets more brighter with time. Around 10000 years, the luminosity becomes somewhat same. The temperature also increases and then decreases slightly with passage of time as the star is consuming dark matter. These results are due to setting mass of star equal to $1M_{\odot}$. Figure 7.3 shows the plot between luminosity and temperature.

In Appendix A, the rest of the output data is shown for the Very Dark case. One can see the dark matter density increases drastically, then slowly goes down. The energy deposited by dark matter annihilation increases with time. Since the mass is

same throughout, the capture and net accretion rate also decreases.

Similarly, in Appendix B and C, the output data of the Dark and Normal cases are shown. The interesting thing to note is that in the Normal case the all the parameters, i.e. density, temperature, number of WIMPs in the star, and annually injected annihilation energy increases gradually. This is because in the Normal case, the dark matter density is small, therefore the star collects dark matter much more slowly than the rest of the two cases, therefore, the parameters increase gradually. Even though a very simple exemplar codes, they show clearly that for a star to become dark star one requires a highly dense dark matter halo density, which is criteria 1 (section 3.1.1) and dark matter annihilation becomes dominant energy source of the star, i.e. criteria 2 (section 3.1.3). This code is extremely powerful tool and using this code, one can simulate the formation and evolution of dark stars for various scenarios. This is clearly evident by the outputs of exemplar codes shown here.

Chapter 8

Summary

Works like [144], which discusses dark matter annihilation in the Sun, indirect detection due to dark matter annihilation in the Sun as a possible way to find WIMPs was proposed by[145]; indirect detection in the Earth as a possible way to find WIMPs was proposed [146] and [147]; indirect detection due to annihilation at the Galactic Center was proposed [148]; effects of nonannihilating WIMPs on convection in stars was considered by [149]. The role of dark matter annihilation on the evolution of the Sun and other Population I main-sequence stars, including in galactic nuclei leading to black hole formation, was previously studied by [150] and [151]. Therefore, the idea of studying dark matter effects on stars is not new.

In this work we have discussed about Dark Stars. Proposed by [1], these stars use dark matter-dark matter annihilation as their energy source to keep themselves in hydrostatic and thermal equilibrium even though these stars are made (almost entirely) of hydrogen and helium. The WIMP or Weakly Interacting Massive Particle is the preferred model of dark matter. These are the stars that are theorised to be born when Universe was roughly 200 million years old at redshift $z = 10 - 15$ ending the dark ages of the Universe and can grow as long as there is dark matter to power it, therefore it can reach the mass of $10^7 M_\odot$ with luminosity $10^{11} L_\odot$.

For a star to be born as dark star, three important criteria should be fulfilled:

- High dark matter density
- Dark matter annihilation products gets trapped at the stellar surface
- Dark matter annihilation is the dominant energy source of the star.

The dark star is born at the center of a dense dark matter halo, which can accrete dark matter either via Blumenthal method of adiabatic contraction or Young's method. Both ways are capable enough to accrete huge amount dark matter in the star. Once the dark star consumes the dark matter, the star contracts gravitaionally which provides energy to the star for some time and then the nuclear fusion kicks in as the main energy source. If the star finds itself surrounded by a dense dark matter halo again, it can gather dark matter via scattering capture process. Since these stars do not produce ionising photons which prevent further accretion.

The annihilation of dark matter in a star makes it look younger than the star of the same stellar properties. These stars are bright, huge,puffy($\sim 10 AU$) and have a low surface temperature($\sim 10000 K$) as long as there is dark matter present to provide energy to it via annihilation. James Webb Space telescope is capable enough to observe them, and they can leave behind signatures in the Cosmic Microwave Background and re-ionization. These stars can in-fact delay the reionization of the Universe. These stars are an ideal laboratories to put constraints on the properties of dark matter as the stellar properties of these stars are dependent on the properties of the dark matter. The code "DarkStars" is a very powerful tool that can be useful

in studying them. If dark stars get massive enough, their mergers should provide a gravitational wave signal. Because they are extended, their gravitational wave signature should be different from that of similar-mass black holes. This might be an interesting approach for LIGO to find dark stars. Because they are composed of relatively cool baryons, the electromagnetic signature of the event may differ significantly from that of a much hotter accretion disk. These stars may potentially serve as a possible seed for the creation of supermassive black holes.[2]

Such type of stars, if discovered in near future, will open up new ways to understand stellar evolution and dark matter, which is extremely exciting.

References

[1] D. Spolyar, K. Freese, and P. Gondolo, Physical Review Letters **100**, 051101 (2008).

[2] K. Freese, T. Rindler-Daller, D. Spolyar, and M. Valluri, Reports on Progress in Physics **79**, 066902 (2016).

[3] P. Scott, J. Edjsö, and M. Fairbairn, in *Dark matter in astrophysics and particle physics* (World Scientific, 2010), pp. 320–327.

[4] D. N. Spergel, M. Bolte, and W. Freedman, Proceedings of the National Academy of Sciences **94**, 6579 (1997).

[5] P. J. E. Peebles, D. Schramm, E. Turner, and R. Kron, Nature **352**, 769 (1991).

[6] P. J. E. Peebles, D. N. Schramm, E. L. Turner, and R. G. Kron, Scientific American **271**, 52 (1994).

[7] A. Santangelo and J. Jochum, *Lecture script observational cosmology* (Institute for Astronomy and Astrophysics(IAAT), Faculty of Science, Eberhard Karls University of Tübingen, Summer term 2018).

[8] C. Sivaram, Astrophysics and space science **125**, 189 (1986).

[9] Planck Collaboration, Aghanim, N., Akrami, Y., Ashdown, M., Aumont, J., Baccigalupi, C., Ballardini, M., Banday, A. J., Barreiro, R. B., Bartolo, N., Basak, S., Battye, R., Benabed, K., Bernard, J.-P., Bersanelli, M., Bielewicz, P., Bock, J. J., Bond, J. R., Borrill, J., Bouchet, F. R., Boulanger, F., Bucher, M., Burigana, C., Butler, R. C., Calabrese, E., Cardoso, J.-F., Carron, J., Challinor, A., Chiang, H. C., Chluba, J., Colombo, L. P. L., Combet, C., Contreras, D., Crill, B. P., Cuttaia, F., de Bernardis, P., de Zotti, G., Delabrouille, J., Delouis, J.-M., Di Valentino, E., Diego, J. M., Doré, O., Douspis, M., Ducout, A., Dupac, X., Dusini, S., Efstathiou, G., Elsner, F., Enßlin, T. A., Eriksen, H. K., Fantaye, Y., Farhang, M., Fergusson, J., Fernandez-Cobos, R., Finelli, F., Forastieri, F., Frailis, M., Fraisse, A. A., Franceschi, E., Frolov, A., Galeotta, S., Galli, S., Ganga, K., Génova-Santos, R. T., Gerbino, M., Ghosh, T., González-Nuevo, J., Górski, K. M., Gratton, S., Gruppuso, A., Gudmundsson, J. E., Hamann, J., Handley, W., Hansen, F. K., Herranz, D., Hildebrandt, S. R., Hivon, E., Huang, Z., Jaffe, A. H., Jones, W. C., Karakci, A., Keihänen, E., Keskitalo, R., Kiiveri, K., Kim, J., Kisner, T. S., Knox, L., Krachmalnicoff, N., Kunz, M., Kurki-Suonio, H., Lagache, G., Lamarre, J.-M., Lasenby, A., Lattanzi, M., Lawrence, C. R., Le Jeune, M., Lemos, P., Lesgourgues, J., Levrier, F., Lewis, A., Liguori, M., Lilje, P. B., Lilley, M., Lindholm, V., López-Caniego, M., Lubin, P. M., Ma, Y.-Z., Macıas-Pérez, J. F., Maggio, G., Maino, D., Mandolesi, N., Mangilli, A., Marcos-Caballero, A., Maris, M., Martin, P. G., Martinelli, M., Martınez-González, E., Matarrese, S., Mauri, N., McEwen, J. D., Meinhold, P. R., Melchiorri, A., Mennella, A., Migliaccio, M., Millea, M., Mitra, S., Miville-Deschênes, M.-A., Molinari, D., Montier, L., Morgante, G., Moss, A., Natoli, P., Nørgaard-Nielsen, H. U., Pagano, L., Paoletti, D., Partridge, B., Patanchon, G., Peiris, H. V., Perrotta, F., Pettorino, V., Piacentini, F., Polastri, L., Polenta, G., Puget, J.-L.,

Rachen, J. P., Reinecke, M., Remazeilles, M., Renzi, A., Rocha, G., Rosset, C., Roudier, G., Rubiño-Martın, J. A., Ruiz-Granados, B., Salvati, L., Sandri, M., Savelainen, M., Scott, D., Shellard, E. P. S., Sirignano, C., Sirri, G., Spencer, L. D., Sunyaev, R., Suur-Uski, A.-S., Tauber, J. A., Tavagnacco, D., Tenti, M., Toffolatti, L., Tomasi, M., Trombetti, T., Valenziano, L., Valiviita, J., Van Tent, B., Vibert, L., Vielva, P., Villa, F., Vittorio, N., Wandelt, B. D., Wehus, I. K., White, M., White, S. D. M., Zacchei, A., and Zonca, A., A&A **652**, C4 (2021).

[10] C. S. Frenk and S. D. M. White, Annalen der Physik **524**, 507 (2012).

[11] F. Zwicky, Helvetica Physica Acta **6**, 110 (1933).

[12] H. W. Babcock, Lick Observatory Bulletin **19**, 41 (1939).

[13] F. D. Kahn and L. Woltjer, The Astrophysical Journal **130**, 705 (1959).

[14] J. P. Ostriker, P. J. E. Peebles, and A. Yahil, **193**, L1 (1974).

[15] J. Einasto, E. Saar, A. Kaasik, and A. D. Chernin, Nature **252**, 111 (1974).

[16] J. P. Ostriker and P. J. Peebles, The Astrophysical Journal **186**, 467 (1973).

[17] S. D. White and M. J. Rees, Monthly Notices of the Royal Astronomical Society **183**, 341 (1978).

[18] D. Clowe, M. Bradač, A. H. Gonzalez, M. Markevitch, S. W. Randall, C. Jones, and D. Zaritsky, The Astrophysical Journal Letters **648**, L109 (2006).

[19] A. H. Peter, arXiv preprint arXiv:1201.3942 (2012).

[20] R. H. Cyburt, Physical Review D **70**, 023505 (2004).

[21] R. D. Peccei and H. R. Quinn, Physical Review D **16**, 1791 (1977).

[22] K. Sigurdson, M. Doran, A. Kurylov, R. R. Caldwell, and M. Kamionkowski, Physical Review D **70**, 083501 (2004).

[23] G. Steigman and M. S. Turner, Nuclear Physics B **253**, 375 (1985).

[24] G. Bertone, D. Hooper, and J. Silk, Physics reports **405**, 279 (2005).

[25] G. Jungman, M. Kamionkowski, and K. Griest, Physics Reports **267**, 195 (1996).

[26] L. Bergström and P. Ullio, Nuclear Physics B **504**, 27 (1997).

[27] P. Ullio and L. Bergström, Physical Review D **57**, 1962 (1998).

[28] G. Gounaris, J. Layssac, P. Porfyriadis, and F. Renard, Physical Review D **69**, 075007 (2004).

[29] E. Ripamonti and T. Abel, 10.1201/9781420012095.ch5 (2005).

[30] R. Barkana and A. Loeb, Physics reports **349**, 125 (2001).

[31] V. Bromm and R. B. Larson, Annu. Rev. Astron. Astrophys. **42**, 79 (2004).

[32] N. Yoshida, K. Omukai, and L. Hernquist, Science **321**, 669 (2008).

[33] D. Hollenbach and C. F. McKee, **41**, 555 (1979).

[34] K. Omukai and R. Nishi, The Astrophysical Journal **508**, 141 (1998).

[35] G. R. Blumenthal, S. Faber, R. Flores, and J. R. Primack, The Astrophysical Journal **301**, 27 (1986).

[36] P. Young, The Astrophysical Journal **242**, 1232 (1980).

[37] K. Freese, P. Gondolo, J. Sellwood, and D. Spolyar, The Astrophysical Journal **693**, 1563 (2009).

[38] T. Abel, G. L. Bryan, and M. L. Norman, science **295**, 93 (2002).

[39] J. F. Navarro, C. S. Frenk, and S. D. M. White, **462**, 563 (1996).

[40] E. Ripamonti, M. Mapelli, and A. Ferrara, Monthly Notices of the Royal Astronomical Society **375**, 1399 (2007).

[41] A. Natarajan, J. C. Tan, and B. W. O'Shea, The Astrophysical Journal **692**, 574 (2009).

[42] M. E. Peskin, *An introduction to quantum field theory* (CRC press, 2018).

[43] L. Gao, N. Yoshida, T. Abel, C. Frenk, A. Jenkins, and V. Springel, Monthly Notices of the Royal Astronomical Society **378**, 449 (2007).

[44] N. Yoshida, K. Omukai, L. Hernquist, and T. Abel, The Astrophysical Journal **652**, 6 (2006).

[45] K. Freese, P. Bodenheimer, P. Gondolo, and D. Spolyar, New Journal of Physics **11**, 105014 (2009).

[46] P. Gondolo, J.-H. Huh, H. Do Kim, and S. Scopel, Journal of Cosmology and Astroparticle Physics **2010**, 026 (2010).

[47] G. Servant and T. M. Tait, Nuclear Physics B **650**, 391 (2003).

[48] O. Adriani, G. Barbarino, G. Bazilevskaya, R. Bellotti, M. Boezio, E. Bogomolov, L. Bonechi, M. Bongi, V. Bonvicini, S. Bottai, A. Bruno, F. Cafagna, D. Campana, P. Carlson, M. Casolino, G. Castellini, M. Pascale, G. De Rosa, N. Simone, and V. Zverev, Nature **458**, 607 (2009).

[49] A. Abdo, M. Ackermann, M. Ajello, W. Atwood, M. Axelsson, L. Baldini, J. Ballet, G. Barbiellini, D. Bastieri, M. Battelino, B. Baughman, K. Bechtol, R. Bellazzini, B. Berenji, R. Blandford, E. Bloom, G. Bogaert, E. Bonamente, A. Borgland, and M. Ziegler, Physical review letters **102**, 181101 (2009).

[50] F. Aharonian, A. Akhperjanian, U. B. De Almeida, A. Bazer-Bachi, Y. Becherini, B. Behera, W. Benbow, K. Bernlöhr, C. Boisson, A. Bochow, et al., Physical Review Letters **101**, 261104 (2008).

[51] S. Galli, F. Iocco, G. Bertone, and A. Melchiorri, Physical Review D **80**, 023505 (2009).

[52] T. R. Slatyer, N. Padmanabhan, and D. P. Finkbeiner, Physical Review D **80**, 043526 (2009).

[53] N. Padmanabhan and D. P. Finkbeiner, Physical Review D **72**, 023508 (2005).

[54] T. A. Porter, *Fermi lat measurements of the diffuse gamma-ray emission at intermediate galactic latitudes*, 2009.

[55] F. Iocco, A. Bressan, E. Ripamonti, R. Schneider, A. Ferrara, and P. Marigo, Monthly Notices of the Royal Astronomical Society **390**, 1655 (2008).

[56] D. Spolyar, P. Bodenheimer, K. Freese, and P. Gondolo, The Astrophysical Journal **705**, 1031 (2009).

[57] K. Freese, D. Spolyar, and A. Aguirre, Journal of Cosmology and Astroparticle Physics **2008**, 014 (2008).

[58] P. Scott, *Dark stars: structure, evolution and impacts upon the high-redshift universe*, 2011.

[59] J. Binney and S. Tremaine, Binney, J. & Tremaine, S (1987).

[60] A. Heger and S. E. Woosley, The Astrophysical Journal **724**, 341 (2010).

[61] K. Freese, P. Bodenheimer, D. Spolyar, and P. Gondolo, The Astrophysical Journal **685**, L101 (2008).

[62] S. Chandrasekhar, *Book review: an introduction to the study of stellar structure, by s. chandrasekhar*, 1939.

[63] S. Hirano, H. Umeda, and N. Yoshida, The Astrophysical Journal **736**, 58 (2011).

[64] M. Taoso, G. Bertone, G. Meynet, and S. Ekström, Phys. Rev. D **78**, 123510 (2008).

[65] S. Ekström, G. Meynet, A. Maeder, and F. Barblan, Astronomy & Astrophysics **478**, 467 (2008).

[66] P. Scott, J. Edsjö, and M. Fairbairn, in *Dark matter in astroparticle and particle physics* (World Scientific, 2008), pp. 387–392.

[67] P. Scott, M. Fairbairn, and J. Edsjö, Monthly Notices of the Royal Astronomical Society **394**, 82 (2009).

[68] T. Rindler-Daller, K. Freese, R. H. Townsend, and L. Visinelli, Monthly Notices of the Royal Astronomical Society **503**, 3677 (2021).

[69] *Webb's launch gsfc/nasa*.

[70] C. Ilie, K. Freese, M. Valluri, I. T. Iliev, and P. R. Shapiro, Monthly Notices of the Royal Astronomical Society **422**, 2164 (2012).

[71] E. Zackrisson, P. Scott, C.-E. Rydberg, F. Iocco, B. Edvardsson, G. Östlin, S. Sivertsson, A. Zitrin, T. Broadhurst, and P. Gondolo, The Astrophysical Journal **717**, 257 (2010).

[72] Gustafsson, B., Edvardsson, B., Eriksson, K., Jørgensen, U. G., Nordlund, Å., and Plez, B., A&A **486**, 951 (2008).

[73] I. Hubeny and T. Lanz, **439**, 875 (1995).

[74] E. Zackrisson, N. Bergvall, K. Olofsson, and A. Siebert, Astronomy & Astrophysics **375**, 814 (2001).

[75] P. F. Hopkins, G. T. Richards, and L. Hernquist, The Astrophysical Journal **654**, 731 (2007).

[76] T. Lejeune, F. Cuisinier, and R. Buser, Astronomy and Astrophysics Supplement Series **130**, 65 (1998).

[77] A. Burrows, D. Sudarsky, and I. Hubeny, The Astrophysical Journal **640**, 1063 (2006).

[78] A. Burrows, D. Sudarsky, and J. I. Lunine, The Astrophysical Journal **596**, 587 (2003).

[79] C. C. Steidel, M. Giavalisco, M. Pettini, M. Dickinson, and K. L. Adelberger, The Astrophysical Journal Letters **462**, L17 (1996).

[80] R. J. Bouwens, G. Illingworth, I. Labbe, P. Oesch, M. Trenti, C. M. Carollo, P. Van Dokkum, M. Franx, M. Stiavelli, V. González, et al., Nature **469**, 504 (2011).

[81] P. Oesch, R. J. Bouwens, G. Illingworth, I. Labbé, M. Trenti, V. Gonzalez, C. M. Carollo, M. Franx, P. van Dokkum, and D. Magee, The Astrophysical Journal **745**, 110 (2012).

[82] E. Zackrisson, P. Scott, C.-E. Rydberg, F. Iocco, S. Sivertsson, G. Östlin, G. Mellema, I. T. Iliev, and P. R. Shapiro, Monthly Notices of the Royal Astronomical Society: Letters **407**, L74 (2010).

[83] E. Zackrisson, P. Scott, C.-E. Rydberg, F. Iocco, S. Sivertsson, G. Östlin, G. Mellema, I. T. Iliev, and P. R. Shapiro, Monthly Notices of the Royal Astronomical Society: Letters **407**, L74 (2010).

[84] E. Zackrisson, C.-E. Rydberg, D. Schaerer, G. Östlin, and M. Tuli, The Astrophysical Journal **740**, 13 (2011).

[85] P. Scott, A. Venkatesan, E. Roebber, P. Gondolo, E. Pierpaoli, and G. Holder, The Astrophysical Journal **742**, 129 (2011).

[86] E. Dwek and F. Krennrich, Astroparticle Physics **43**, 112 (2013).

[87] A. Maurer, M. Raue, T. Kneiske, D. Horns, D. Elsässer, and P. Hauschildt, The Astrophysical Journal **745**, 166 (2012).

[88] D. R. Schleicher, R. Banerjee, and R. S. Klessen, Physical Review D **79**, 043510 (2009).

[89] R. Genzel, F. Eisenhauer, and S. Gillessen, Reviews of Modern Physics **82**, 3121 (2010).

[90] J. Jackson, N. Geis, R. Genzel, A. Harris, S. Madden, A. Poglitsch, G. Stacey, and C. Townes, The Astrophysical Journal **402**, 173 (1993).

[91] M. Christopher, N. Scoville, S. Stolovy, and M. S. Yun, The Astrophysical Journal **622**, 346 (2005).

[92] M. Montero-Castaño, R. M. Herrnstein, and P. T. Ho, The Astrophysical Journal **695**, 1477 (2009).

[93] W. Forrest, J. Pipher, and W. Stein, The Astrophysical Journal **301**, L49 (1986).

[94] D. A. Allen, A. Hyland, and D. Hillier, Monthly Notices of the Royal Astronomical Society **244**, 706 (1990).

[95] A. Krabbe, R. Genzel, S. Drapatz, and V. Rotaciuc, The Astrophysical Journal **382**, L19 (1991).

[96] A. Krabbe, R. Genzel, A. Eckart, F. Najarro, D. Lutz, M. Cameron, H. Kroker, L. Tacconi-Garman, N. Thatte, L. Weitzel, et al., The Astrophysical Journal Letters **447**, L95 (1995).

[97] R. Sanders, Nature **359**, 131 (1992).

[98] M. Morris, The Astrophysical Journal **408**, 496 (1993).

[99] A. Ghez, G. Duchêne, K. Matthews, S. Hornstein, A. Tanner, J. Larkin, M. Morris, E. Becklin, S. Salim, T. Kremenek, et al., The Astrophysical Journal Letters **586**, L127 (2003).

[100] T. Paumard, R. Genzel, F. Martins, S. Nayakshin, A. Beloborodov, Y. Levin, S. Trippe, F. Eisenhauer, T. Ott, S. Gillessen, et al., The Astrophysical Journal **643**, 1011 (2006).

[101] Y. Levin and A. M. Beloborodov, The Astrophysical Journal Letters **590**, L33 (2003).

[102] R. Genzel, R. Schödel, T. Ott, F. Eisenhauer, R. Hofmann, M. Lehnert, A. Eckart, T. Alexander, A. Sternberg, R. Lenzen, et al., The Astrophysical Journal **594**, 812 (2003).

[103] *The Nobel Prize in Physics 2020*, en-US.

[104] R. Genzel, A. Eckart, T. Ott, and F. Eisenhauer, Monthly Notices of the Royal Astronomical Society **291**, 219 (1997).

[105] A. Ghez, S. Salim, S. D. Hornstein, A. Tanner, J. Lu, M. Morris, E. Becklin, and G. Duchêne, The Astrophysical Journal **620**, 744 (2005).

[106] F. Martins, S. Gillessen, F. Eisenhauer, R. Genzel, T. Ott, and S. Trippe, The Astrophysical Journal Letters **672**, L119 (2007).

[107] Y. Levin and A. M. Beloborodov, The Astrophysical Journal Letters **590**, L33 (2003).

[108] O. Gerhard, The Astrophysical Journal Letters **546**, L39 (2000).

[109] H. M. Lee, The astrophysical journal **319**, 801 (1987).

[110] M. B. Davies and A. King, The Astrophysical Journal Letters **624**, L25 (2005).

[111] J. G. Hills, Nature **331**, 687 (1988).

[112] C. Hopman and T. Alexander, The Astrophysical Journal **645**, 1152 (2006).

[113] H. B. Perets, C. Hopman, and T. Alexander, The Astrophysical Journal **656**, 709 (2007).

[114] T. Alexander, arXiv preprint arXiv:0708.0688 (2007).

[115] Q. Zhu, R. P. Kudritzki, D. F. Figer, F. Najarro, and D. Merritt, The Astrophysical Journal **681**, 1254 (2008).

[116] S. Clea, A. Kenath, C. Sivaram, and S. Gudennavar, Physics of the Dark Universe **30**, 100727 (2020).

[117] Lopes, José and Lopes, Ilıdio, A&A **651**, A101 (2021).

[118] N. F. Bell, G. Busoni, and S. Robles, Journal of Cosmology and Astroparticle Physics **2018**, 018 (2018).

[119] J. F. Acevedo, J. Bramante, R. K. Leane, and N. Raj, Journal of Cosmology and Astroparticle Physics **2020**, 038 (2020).

[120] N. F. Bell, G. Busoni, S. Robles, and M. Virgato, Journal of Cosmology and Astroparticle Physics **2020**, 028 (2020).

[121] C.-S. Chen and Y.-H. Lin, Journal of High Energy Physics **2018**, 1 (2018).

[122] T. Güver, A. E. Erkoca, M. H. Reno, and I. Sarcevic, Journal of Cosmology and Astroparticle Physics **2014**, 013 (2014).

[123] N. F. Bell, G. Busoni, M. E. Ramirez-Quezada, S. Robles, and M. Virgato, Journal of Cosmology and Astroparticle Physics **2021**, 083 (2021).

[124] A. R. Zentner and A. P. Hearin, Phys. Rev. D **84**, 101302 (2011).

[125] T. J. Raen, H. Martınez-Rodrıguez, T. J. Hurst, A. R. Zentner, C. Badenes, and R. Tao, Monthly Notices of the Royal Astronomical Society **503**, 5611 (2021).

[126] A. Maselli, C. Kouvaris, and K. D. Kokkotas, International Journal of Modern Physics D **30**, 2150003, 2150003 (2021).

[127] J. Casanellas and I. Lopes, The Astrophysical Journal **705**, 135 (2009).

[128] J. Casanellas and I. Lopes, The Astrophysical Journal Letters **733**, L51 (2011).

[129] R. Ibata, C. Nipoti, A. Sollima, M. Bellazzini, S. Chapman, and E. Dalessandro, Monthly Notices of the Royal Astronomical Society **428**, 3648 (2013).

[130] K. Inayoshi, E. Visbal, and Z. Haiman, Annual Review of Astronomy and Astrophysics **58**, 27 (2020).

[131] R. Abbott et al. (LIGO Scientific Collaboration and Virgo Collaboration), Phys. Rev. Lett. **125**, 101102 (2020).

[132] B. P. Abbott et al. (LIGO Scientific Collaboration and Virgo Collaboration), Phys. Rev. Lett. **116**, 061102 (2016).

[133] J. Ziegler and K. Freese, Phys. Rev. D **104**, 043015 (2021).

[134] P. P. Eggleton, Monthly Notices of the Royal Astronomical Society **151**, 351 (1971).

[135] P. P. Eggleton, Monthly Notices of the Royal Astronomical Society **156**, 361 (1972).

[136] O. R. Pols, C. A. Tout, P. P. Eggleton, and Z. Han, Monthly Notices of the Royal Astronomical Society **274**, 964 (1995).

[137] A. Gould, The Astrophysical Journal **321**, 571 (1987).

[138] P. Gondolo, J. Edsjö, P. Ullio, L. Bergström, M. Schelke, and E. A. Baltz, Journal of Cosmology and Astroparticle Physics **2004**, 008 (2004).

[139] M. Fairbairn and T. Schwetz, Journal of Cosmology and Astroparticle Physics **2009**, 037 (2009).

[140] M. Fairbairn and T. Schwetz, Journal of Cosmology and Astroparticle Physics **2009**, 037 (2009).

[141] M. Fairbairn, P. Scott, and J. Edsjö, Physical Review D **77**, 047301 (2008).

[142] P. C. SCOTT, J. EDSJÖ, and M. FAIRBAIRN, Dark Matter in Astroparticle and Particle Physics, 10.1142/9789812814357_0038 (2008).

[143] P. Scott, M. Fairbairn, and J. Edsjö, arXiv preprint arXiv:0810.5560 (2008).

[144] L. M. Krauss, K. Freese, D. Spergel, and W. Press, The Astrophysical Journal **299**, 1001 (1985).

[145] M. Srednicki, K. A. Olive, and J. Silk, Nuclear Physics B **279**, 804 (1987).

[146] K. Freese, Physics Letters B **167**, 295 (1986).

[147] L. M. Krauss, M. Srednicki, and F. Wilczek, Physical Review D **33**, 2079 (1986).

[148] P. Gondolo and J. Silk, Physical Review Letters **83**, 1719 (1999).

[149] A. Bouquet and P. Salati, Astronomy and Astrophysics **217**, 270 (1989).

[150] P. Salati and J. Silk, **338**, 24 (1989).

[151] A. Bouquet and P. Salati, The Astrophysical Journal **346**, 284 (1989).

Appendix A

Very Dark case of DarkStar

Here are the values of various stellar properties of the Very Dark case are listed(Table A1). It is clearly seen that for this case the star gathers dark matter much more quickly and in huge amount than the rest two cases. The density and WIMP isothermal temperature are increasing but reduces as the star starts to annihilate, which becomes the dominate energy source of the star.

TABLE A.1: Table showing, luminosity, temperature, density and mass of a solar mass star in very dark scenario

Model	Time(years)	mass(solar mass)	Log L	Log T_S	Log RHO	Log T_C
1	0.120000000000E+02	0.100000000000E+01	-.502509548085E-01	0.376760905808E+01	0.190147415293E+01	0.713063006253E+01
2	0.240000000000E+02	0.999999999998E+00	-.502169360274E-01	0.376765256309E+01	0.190145373543E+01	0.713061693428E+01
3	0.420000000000E+02	0.999999999995E+00	-.502329850504E-01	0.376765012819E+01	0.190145111561E+01	0.713061749297E+01
4	0.690000000000E+02	0.999999999990E+00	-.502540348054E-01	0.376764678967E+01	0.190144300650E+01	0.713061915286E+01
5	0.109500000000E+03	0.999999999983E+00	-.502815116462E-01	0.376764236860E+01	0.190142457025E+01	0.713062284203E+01
6	0.170250000000E+03	0.999999999972E+00	-.503176024831E-01	0.376763649053E+01	0.190139263347E+01	0.713062888856E+01
7	0.261375000000E+03	0.999999999956E+00	-.503644591262E-01	0.376762882645E+01	0.190134352460E+01	0.713063791034E+01
8	0.398062500000E+03	0.999999999933E+00	-.504250699061E-01	0.376761882561E+01	0.190127137740E+01	0.713065032086E+01
9	0.603093750000E+03	0.999999999897E+00	-.505023708559E-01	0.376760591391E+01	0.190116455887E+01	0.713066801504E+01
10	0.910640625000E+03	0.999999999843E+00	-.505988099486E-01	0.376758959307E+01	0.190100862427E+01	0.713069183624E+01
11	0.137196093750E+04	0.999999999763E+00	-.507174452318E-01	0.376756911304E+01	0.190078072009E+01	0.713072388542E+01
12	0.206394140625E+04	0.999999999642E+00	-.508613587184E-01	0.376754359540E+01	0.190042040441E+01	0.713076220870E+01
13	0.310191210938E+04	0.999999999462E+00	-.510358573306E-01	0.376751179949E+01	0.189993510177E+01	0.713081574775E+01
14	0.465886816406E+04	0.999999999191E+00	-.512447923068E-01	0.376747178745E+01	0.189923498054E+01	0.713088172390E+01
15	0.699430224609E+04	0.999999998784E+00	-.514910494607E-01	0.376742180306E+01	0.189822985513E+01	0.713095575921E+01
16	0.104974533691E+05	0.999999998175E+00	-.514981016360E-01	0.376740082167E+01	0.189678832618E+01	0.713103167323E+01
17	0.157521800537E+05	0.999999997261E+00	-.514587915320E-01	0.376737667788E+01	0.189473565457E+01	0.713109035211E+01
18	0.236342700806E+05	0.999999995889E+00	-.513992077345E-01	0.376734160339E+01	0.189182067907E+01	0.713110038519E+01
19	0.370338231262E+05	0.999999993556E+00	-.514052241476E-01	0.376727357619E+01	0.188726473101E+01	0.713099427732E+01
20	0.476746446625E+05	0.999999991703E+00	-.514913059199E-01	0.376721075360E+01	0.188376940351E+01	0.713082906733E+01

TABLE A.2: Various parameters of $1M_{\odot}$star for Very Dark case

Model Number	Total number of WIMPS in star	Capture rate (WIMPs/yr)	Net accretion rate (WIMPs/yr)	Annually injected annihilation energy (GeV)
0	1.0000000000000000E+030	2.9227621365609641E+042	2.9227621365609641E+042	7273071589272930.0
1	3.4719602252341779E+043	2.8147781968826861E+042	2.7346358266105234E+042	8.0142370272162883E+042
2	6.6374579762366757E+043	2.8147150738488159E+042	2.5217740249194931E+042	2.9294104892932268E+043
3	1.0765595675392021E+044	2.8147118568247174E+042	2.0440782642977294E+042	7.7063359252698806E+043
4	1.5222360172386954E+044	2.8147016032350511E+042	1.2739906852901672E+042	1.5407109179448839E+044
5	1.8638891449616093E+044	2.8146780728749198E+042	5.0498642701450808E+041	2.3096916458604119E+044
6	2.0193732316797036E+044	2.8146363992203595E+042	1.0389598443304859E+041	2.7107404147873109E+044
7	2.0545117236275128E+044	2.8145716303464221E+042	9.2955028244122164E+039	2.8052761275220098E+044
8	2.0578318579482762E+044	2.8144741919807310E+042	9.6295938498628255E+038	2.8135112325957446E+044
9	2.0581826945484093E+044	2.8143280514426121E+042	1.0900703616664469E+039	2.8132379810809458E+044
10	2.0585813182569483E+044	2.8141089285543931E+042	1.5505880634547584E+039	2.8125583404909384E+044
11	2.0591486951329296E+044	2.8137804124730115E+042	2.1630375586849905E+039	2.8116173749143266E+044
12	2.0599406164778481E+044	2.8132858834513827E+042	3.3030595061910429E+039	2.8099828239451918E+044
13	2.0611509633953819E+044	2.8125462155923860E+042	4.4160074077169131E+039	2.8081302081846689E+044
14	2.0627709883999617E+044	2.8114381738461307E+042	6.2959630613993141E+039	2.8051422107847313E+044
15	2.0650845700192859E+044	2.8097786239761927E+042	8.8112285890592159E+039	2.8009673953871334E+044
16	2.0683301709131147E+044	2.8072948007440601E+042	1.2214638253931192E+040	2.7950801624901290E+044
17	2.0728445966858097E+044	2.8035840535677754E+042	1.6591325560847388E+040	2.7869927280069282E+044
18	2.0790053963027082E+044	2.7980491375400669E+042	2.2724462756619957E+040	2.7753246747834468E+044
19	2.0900956861045605E+044	2.7889304399842431E+042	2.6658097013791719E+040	2.7622723429704516E+044
20	2.1001570017374980E+044	2.7816319647606854E+042	2.4715191033968469E+040	2.7569167737267170E+044

TABLE A.3: Various parameters of $1M_{\odot}$star for Very Dark case cont..

Model Number	WIMP thermal radius (stellar radii)	WIMP isothermal temperature (K)	Central WIMP density (WIMPs/cm3)
0	1.47639433532357 50E-002	13639200.733449310	217.29358749831812
1	1.51627456863269 05E-002	13469562.169904808	72398830835104 29.0
2	1.51653171251918 20E-002	13469193.724786041	13853109798743870
3	1.51654827827967 36E-002	13469210.968493331	22468718390460360.
4	1.51657877174689 35E-002	13469262.364531359	31769300218607436.
5	1.51663450238659 83E-002	13469375.840496330	38896205440669176.
6	1.51672279056839 67E-002	13469562.913038993	42135302037220248.
7	1.51685259225658 68E-002	13469841.680646455	42859439200360752.
8	1.51703625748161 25E-002	13470225.863323675	42916129734953760.
9	1.51729855453149 32E-002	13470773.644233327	42904995951383704.
10	1.51766703107218 46E-002	13471511.105471708	42886968864609272.
11	1.51818548223234 94E-002	13472503.859429931	42861326359969680.
12	1.51895558494405 06E-002	13473693.324289767	42820310232242592.
13	1.51998097956361 30E-002	13475352.435864622	42768083448766992.
14	1.52140782456331 98E-002	13477395.685636971	42690225799018288.
15	1.52338047727634 64E-002	13479687.138613088	42581440322810304.
16	1.52590912606958 23E-002	13482034.351436019	42428958883795568.
17	1.52938350926424 34E-002	13483844.513877619	42215967221809456.
18	1.53418935997789 35E-002	13484138.434763724	41923192603838464.
19	1.54159694270833 81E-002	13480819.406006904	41516392034451680.
20	1.54722436128495 14E-002	13475675.371933043	41246604043276008.

TABLE A.4: Various parameters of $1 M_{\odot}$star for Very Dark case cont..

Model number	WIMP density at thermal radius (WIMPs/cm$\hat{3}$)	WIMP population change during last timestep(%)
0	79.937843539019184	0.0000000000000000
1	2512765433051587.0	3471960225234077.5
2	4803450081772386.0	91.173214715873954
3	7790850611916668.0	62.194558729182766
4	11015756647998846.	41.398215494774689
5	13486958758603096.	22.444162656370828
6	14610094312688644.	8.3419170683188231
7	14861190848089696.	1.7400692153664530
8	14880852542105350.	0.16160211122579154
9	14876944105614544.	1.7048846764519024E-002
10	14870361471057978.	1.9367751443778111E-002
11	14860993714389636.	2.7561547894633161E-002
12	14846421675670920.	3.8458676966375088E-002
13	14827903688873998.	5.8756398502560023E-002
14	14800745017215946.	7.8598076188996002E-002
15	14761066843660928.	0.11215891789901619
16	14707112967001198.	0.15716551956022035
17	14632677089092970.	0.21826427115850683
18	14528527374388258.	0.29721473702123352
19	14383304640021310.	0.42195109640669853
20	14285605459272986.	0.48138062289815292

Appendix B

Dark case of DarkStar

We ca see that for this case the star gathers less WIMP particles than the Dark case. This makes the star be born as dark star later than the dark case. The capture rate and net accretion rate also reduces as the mass of the star is kept same throughout the run. But the density and WIMP isothermal temperature increase.

TABLE B.1: Various parameters of $1 M_{\odot}$ star for Dark case

Model Number	Total number of WIMPS in star	Capture rate (WIMPs/yr)	Net accretion rate (WIMPs/yr)	Annually injected annihilation energy (GeV)
0	1.0000000000000000E+030	2.9227621365609589E+041	2.9227621365609589E+041	7273071589272930.0
1	3.5037402238770199E+042	2.9253046833039383E+041	2.9163635522459643E+041	8.9411310579741623E+040
2	6.9891395642669154E+042	2.9252963690505950E+041	2.8897175618035287E+041	3.5578807247066212E+041
3	1.1858274935458990E+043	2.9252963211011358E+041	2.8228758436114880E+041	1.0242047748964773E+042
4	1.8882084715548925E+043	2.9252961502156390E+041	2.6656134582713815E+041	2.5968269194425766E+042
5	2.8490108274129497E+043	2.9252955547539831E+041	2.3341028052646827E+041	5.9119274948930057E+042
6	4.0231521869208178E+043	2.9252937575132449E+041	1.7464204118394315E+041	1.1788733456738134E+043
7	5.1770679956425734E+043	2.9252892770669547E+041	9.7326065406439918E+040	1.9520286230025555E+043
8	5.9619403161288957E+043	2.9252803501969282E+041	3.3668869022029496E+040	2.5885916599766333E+043
9	6.2735182796163493E+043	2.9252655147884239E+041	5.9352280713805979E+039	2.8659132340746178E+043
10	6.3337210690064222E+043	2.9252428356135131E+041	4.5229415334462507E+038	2.9207198940800667E+043
11	6.3385359940869881E+043	2.9252087838803895E+041	6.9906208624256213E+037	2.9245097217941468E+043
12	6.3392917167153518E+043	2.9251575924583614E+041	8.9844666602733930E+037	2.9242591457923339E+043
13	6.3402653680017373E+043	2.9250808294001497E+041	1.2280776822097458E+038	2.9238527517179401E+043
14	6.3415967468133037E+043	2.9249656944721646E+041	1.7012010533608454E+038	2.9232644934188037E+043
15	6.3434417324376320E+043	2.9247929627077827E+041	2.3430063536078293E+038	2.9224499563541750E+043
16	6.3459840764875490E+043	2.9245337932954179E+041	3.1996431961746569E+038	2.9213341500992432E+043
17	6.3494584013938221E+043	2.9241448843743846E+041	4.3259147217555547E+038	2.9198189696526292E+043
18	6.3541602424568229E+043	2.9235612349574108E+041	5.8096688232841371E+038	2.9177515661341268E+043
19	6.3604831263668120E+043	2.9226854325896191E+041	7.7791135515974290E+038	2.9149063190380217E+043
20	6.3689646944707602E+043	2.9213719611560070E+041	1.0858610425598138E+039	2.9105133507304088E+043

TABLE B.2: Various parameters of $1 M_{\odot}$ star for Dark case cont..

Model Number	WIMP thermal radius (stellar radii)	WIMP isothermal temperature (K)	Central WIMP density (WIMPs/cm$\hat{3}$)
0	1.4763943353235750E-002	13639200.733449310	217.29358749831812
1	1.4690510654973118E-002	13672628.371860409	799450963336270.88
2	1.4691361840796493E-002	13672560.335592424	1595041767398693.2
3	1.4691673156493402E-002	13672561.384250946	2706260384655599.5
4	1.4691720266658380E-002	13672565.968805794	4309206999426244.5
5	1.4691760962407249E-002	13672581.700159008	6501885035114527.0
6	1.4691851915078030E-002	13672628.840597259	9181316532935844.0
7	1.4692046292799433E-002	13672737.792216957	11814262369832652.
8	1.4692403901495815E-002	13672941.963242970	13604434836508902.
9	1.4692961764392063E-002	13673257.962526655	14313876120690970.
10	1.4693763772413113E-002	13673704.903013468	14448994264401542.
11	1.4694893260476342E-002	13674321.686995076	14456797827662274.
12	1.4696543870529946E-002	13675153.697421608	14453702230054830.
13	1.4698786606337829E-002	13676292.930911927	14449534944190740.
14	1.4701884231607622E-002	13677813.812867245	14443673283258348.
15	1.4706141856713548E-002	13679807.707686676	14435669018680050.
16	1.4711994530071911E-002	13682400.578837488	14424693216484808.
17	1.4719977142126124E-002	13685687.884400690	14409787534410050.
18	1.4730810286470847E-002	13689751.550258182	14389320822186330.
19	1.4745498255817967E-002	13694650.047124634	14361708220142542.
20	1.4765386139264858E-002	13700329.776954584	14321803777538178.

TABLE B.3: Various parameters of $1M_{\odot}$star for Dark case cont..

Model number	WIMP density at thermal radius (WIMPs/cm$\hat{3}$)	WIMP population change during last timestep(%)
0	79.93784353901918 4	0.0000000000000000
1	2777989128672 16.44	350374022387601.94
2	5541364643747 36.88	99.476534151643534
3	9401872566618 10.12	69.667164697730485
4	1497070168520435.2	59.231294756770353
5	2258833032277389.5	50.884336678505662
6	3189700640850403.5	41.212246307047195
7	4104418705258053.0	28.681883138130132
8	4726388555589674.0	15.160556537927112
9	4972783750250356.0	5.226116783566 8987
10	5019698638586778.0	0.9596336012231 1647
11	5022400127875131.0	7.602047876922 3951E-002
12	5021433149973292.0	1.192266840590225 0E-002
13	5019987453956019.0	1.535899166492331 3E-002
14	5017948563830545.0	2.099878686916930 4E-002
15	5015043332028913.0	2.909339237401647 7E-002
16	5011049249992706.0	4.007830696885809 9E-002
17	5005723802877483.0	5.474840252350813 4E-002
18	4998526952578317.0	7.405105704714228 0E-002
19	4988388473275229.0	9.950778181106137 4E-002
20	4974092308577102.0	0.133347859516969 65

Appendix C

Normal case of DarkStar

As seen here, in this case the star gathers dark matter much slowly and very less in comparison to the Very Dark case and Dark case. It is clear that for a star to become dark star soon, a highly dense dark matter is required.

TABLE C.1: Various parameters of $1 M_{\odot}$ star for Normal case

Model Number	Total number of WIMPS in star	Capture rate (WIMPs/yr)	Net accretion rate (WIMPs/yr)	Annually injected annihilation energy (GeV)
0	1.0000000000000000E+030	2.9227621365609629E+027	2.9227621365608903E+027	7273071589272930.0
1	1.0350731456387307E+030	2.9264502871985501E+027	2.9264502871984720E+027	7813493877770806.0
2	1.0701905490851126E+030	2.9264428386019774E+027	2.9264428386018938E+027	8352941480430623.0
3	1.1228665201799467E+030	2.9264428332683015E+027	2.9264428332682097E+027	9195460007026038.0
4	1.2018804766781883E+030	2.9264428335163408E+027	2.9264428335162353E+027	10535126541165854.
5	1.3204014114355954E+030	2.9264428338439233E+027	2.9264428338437963E+027	12715374536864034.
6	1.4981828135916047E+030	2.9264428342801529E+027	2.9264428342799891E+027	16369929982867838.
7	1.7648549168653664E+030	2.9264428348574636E+027	2.9264428348572365E+027	22716175935443716.
8	2.1648630718549076E+030	2.9264428355988280E+027	2.9264428355984860E+027	34180473707639448.
9	2.7648753044911887E+030	2.9264428365115689E+027	2.9264428365110114E+027	55753010505239592.
10	3.6648936537262250E+030	2.9264428375334225E+027	2.9264428375324429E+027	97958019398346400.
11	5.0149211780498926E+030	2.9264428384621734E+027	2.9264428384603394E+027	1.8341949404419696E+017
12	7.0399624651771770E+030	2.9264428320710477E+027	2.9264428320674330E+027	3.6145814733341350E+017
13	1.0077524389231477E+031	2.9264428129105012E+027	2.9264428129030943E+027	7.4067058737197914E+017
14	1.4633867245471669E+031	2.9264427638790187E+027	2.9264427638634002E+027	1.5618364973150822E+018
15	2.1468381415292294E+031	2.9264426470512348E+027	2.9264426470176211E+027	3.3613645850827208E+018
16	3.1720152260659169E+031	2.9264423800234077E+027	2.9264423799500263E+027	7.3381482303427973E+018
17	4.7097807125222885E+031	2.9264417869677847E+027	2.9264417868060086E+027	1.6177622146681952E+019
18	7.0164284746453167E+031	2.9264404949534126E+027	2.9264404945943753E+027	3.5903744716601377E+019
19	1.0476398589895825E+032	2.9264377629176732E+027	2.9264377621172491E+027	8.0042424189007823E+019
20	1.5666348916350938E+032	2.9264321647221389E+027	2.9264321629323154E+027	1.7898235858597806E+020

TABLE C.2: Various parameters of $1 M_{\odot}$ star for Normal case cont..

Model Number	WIMP thermal radius (stellar radii)	WIMP isothermal temperature (K)	Central WIMP density (WIMPs/cm$\hat{3}$)
0	1.4763943353235750E-002	13639200.733449310	217.29358749831812
1	1.4683441529974353E-002	13673452.079776708	236.48350624928241
2	1.4684226758029080E-002	13673390.077282522	244.55231014097134
3	1.4684533905060667E-002	13673389.905507760	256.58938590967119
4	1.4684549721305958E-002	13673389.916255873	274.64508667779717
5	1.4684563570179738E-002	13673389.936309196	301.72863920284624
6	1.4684577992043360E-002	13673389.969138252	342.35396937212028
7	1.4684593924368848E-002	13673390.020465013	403.29196504793703
8	1.4684612102754332E-002	13673390.099268457	494.69896207891270
9	1.4684633217756801E-002	13673390.219007388	631.80946216534448
10	1.4684657954097126E-002	13673390.399638601	837.47522641685259
11	1.4684686943193867E-002	13673390.670692751	1145.9739022838364
12	1.4684720226153823E-002	13673390.361234734	1608.7220700404966
13	1.4684758462489995E-002	13673390.241380978	2302.8443370710906
14	1.4684801476776414E-002	13673390.773533197	3344.0271287409414
15	1.4684848731754425E-002	13673393.021531792	4905.7978324220812
16	1.4684899577917816E-002	13673399.331823571	7248.4399595927080
17	1.4684954252561529E-002	13673414.673845863	10762.355832165013
18	1.4685017964446052E-002	13673449.000180243	16033.083187651690
19	1.4685109687131610E-002	13673518.101095844	23938.765293274166
20	1.4685270777586268E-002	13673654.631954907	35796.139915404267

TABLE C.3: Various parameters of $1 M_{\odot}$star for Normal case cont..

Model number	WIMP density at thermal radius (WIMPs/cm$\hat{3}$)	WIMP population change during last timestep(%)
0	79.937843539019184	0.0000000000000000
1	82.175727724245064	3.5073145638730647
2	84.962743165923143	3.3927460676908430
3	89.144703259190265	4.9221114071569687
4	95.417645622494859	7.0368075882767478
5	104.82705809374404	9.8612912895449174
6	118.94117687712806	13.464193586609237
7	140.11235558993209	17.799703804802480
8	171.86912476012884	22.665214639853382
9	219.50428075315693	27.715943813581518
10	290.95701970864155	32.551860395767967
11	398.13613956236213	36.836744852092714
12	558.90484501937397	40.380321349631735
13	800.05792355043593	43.147416468190684
14	1161.7873590711836	45.212918175707479
15	1704.3803352530604	46.703404200523345
16	2518.2649717700951	47.752882003784244
17	3739.0753835532969	48.479133196456338
18	5570.2396447611445	48.975693411588161
19	8316.8420954453959	49.312411973606153
20	12436.342026938455	49.539450813380327